POLITECNICO DI TORINO

Corso di Laurea Magistrale
in Ingegneria Biomedica

Tesi di Laurea

Detecting freezing of gait in Parkinson's Disease (PD) with functional near-infrared spectroscopy (fNIRS), surface electromyography, and inertial sensors

Relatore
Prof. Filippo MOLINARI

Candidato
Francesco VURCHIO

Correlatori
Prof Massimo SALVI
Prof. Massimo FILIPPI
Prof.ssa Federica AGOSTA
Dott.ssa Silvia BASAIA

Anno Accademico 2024-2025

Abstract

Parkinson's disease (PD) is a progressive neurodegenerative disorder affecting the basal ganglia and resulting in motor symptoms such as bradykinesia, rigidity, and tremor. Among its most disabling manifestations, freezing of gait (FoG) is characterized by brief episodes of gait arrest despite the intention to move, thus significantly increasing fall risk and compromising patients' autonomy.

Its pathophysiology remains unclear, involving disrupted cortical-subcortical communication and impaired motor control. The transient and context-dependent nature of FoG makes objective, multimodal assessments essential to improve its characterization and clinical management.

The aim of this study was to characterize FoG in individuals with PD using a multimodal approach based on the simultaneous and equally weighted acquisition of functional near-infrared spectroscopy (fNIRS), surface electromyography (sEMG), and inertial measurement unit (IMU) signals.

Eleven patients with PD were enrolled in this preliminary study, including four individuals who reported experiencing FoG episodes on daily basis (PD-FoG group) and seven patients with no experience with FoG (PD-noFoG group). Participants completed seven motor tasks: four single-task (purely motor) conditions and three dual-task (DT) conditions in which a cognitive task was combined with the primary motor task, specifically designed to elicit FoG episodes.

All recorded signals underwent dedicated preprocessing pipelines to ensure data quality and synchronization across modalities. fNIRS data were processed using the NIRSTORM toolbox, including artifact and non-physiological components removal, 3D reconstruction of cortical activation maps, and statistical analyses to quantify task-related activation at the single-subject level and to compare activation patterns across groups. IMU data were processed to identify gait events (turn and walk phases) and to detect steps. EMG data underwent standard EMG processing, with filtering, normalization and envelope extraction.

Considering the machine learning analysis, fNIRS, EMG, and IMU data were segmented into fixed-length epochs, from which modality-specific feature vectors were extracted. These features were then concatenated to form multimodal representations and used to train and validate ML models through a leave-one-subject-out cross-validation strategy. The binary classification aimed to distinguish between "FoG" and "noFoG" epochs, while a multi-class configuration, including a "preFoG" class, was implemented to enable early prediction of upcoming freezing events.

Ground-truth labels were derived from video annotations independently performed by two trained evaluators, ensuring reliable identification of "FoG" and "preFoG" events, subsequently used to validate ML models.

Cortical β-maps analysis, both at the single subject level and within PD-FoG group, revealed increased activation in prefrontal, premotor, and supplementary motor regions during FoG episodes, consistent with models of impaired automaticity and compensatory frontal recruitment. Between groups contrasts revealed statistically significant differences in non-FoG conditions, suggesting that subjects with FoG may experience different activation patterns in brain activity also when not experiencing freezing episodes.

ML results showed high performance in detecting FoG episodes: in the binary task, multimodal models achieved robust generalization across subjects, with k-nearest neighbors and random-forest classifiers yielding the highest balanced accuracy (97-98% mean and 2.7% standard deviation across folds). Extending the framework to the three-class problem confirmed the possibility of identifying preFoG states, although with lower performance (balanced accuracy between 76% and 84%) and higher inter-subject variability (6-9%).

Overall, this preliminary study supported the feasibility and added value of a fully multimodal framework for the detection of FoG in PD. Capturing different signatures of gait, our approach moves beyond purely clinical assessments and provides a more comprehensive description of freezing episodes. These findings paved the way for larger-scale studies with the long-term goal of informing personalized rehabilitation strategies and interventions to reduce FoG burden and improve patients' autonomy.

List of Contents

List of Figures

List of Tables

List of Equations

List of Abbreviations

Abbreviation	Definition
10MWT	10-Meter Walk Test
ADL	Activities of daily living
BCT	Biceps Femoris
BF	Backwards Counting Task
CMRR	Common-mode rejection ratio
CNN	Convolutional Neural Network
COMT	Catechol-O-methyltransferase
CSF	Cerebrospinal fluid
CoV	Coefficient of Variation
CV	Cross Validation
DaT-SPECT	Dopamine transporter single-photon emission computed tomography
DBS	Deep Brain Stimulation
DL	Deep Learning
DOF	Degrees Of Freedom
DOT	Diffuse Optical Tomography
DPF	Differential Pathlength Factor
DT	Dual Task
DTree	Decision Tree
ECOC	Error-Correcting Output Codes
EEG	Electroencephalogram
EMG	Electromyography
FI	Freezing Index
fNIRS	Functional Near Infrared Spectroscopy
FoG	Freezing of Gait
GC	Gastrocnemius
GBT	Gradient Boosting Tree
GDD	Greater Difficulty Direction
GLM	Generalized Linear Model
GM	Gluteus Maximus
HbO	Oxyhemoglobin
HbR	Deoxyhemoglobin
HD-sEMG	High Density surface Electromyography
HS	Heel Strike
HRF	Hemodynamic Response Function
H&Y	Hoehn and Yahr
IEMG	Integrated EMG
IMU	Inertial Measurement Unit
LASSO	Least Absolute Shrinkage and Selection Operator
LDD	Lower Difficulty Direction
LED	Light emitting diode
LEDD	Levodopa Equivalent Daily Dose
LOF	Local Outlier Factor

Abbreviation	Definition
LOSO	Leave One Subject Out
LSL	Lab Streaming Layer
MAO-B	Monoamine oxidase B
MAV	Mean Absolute Value
MBLL	Modified Beer-Lambert Law
MDS-UPDRS	Movement Disorder Society-Unified Parkinson's Disease Rating Scale
MEM	Maximum Entropy on the Mean
MF	Mean Frequency
mH&Y	Modified Hoehn and Yahr
MI	Mutual Information
ML	Machine Learning
MLR	Mesencephalic locomotor region
MMSE	Mini-Mental Status Examination
MNE	Minimum Norm Estimate
MoCA	Montreal Cognitive Assessment
MRI	Magnetic resonance imaging
MUAP	Motor Unit Action Potential
MVC	Maximum Voluntary Contraction
NFOG-Q	New Freezing of Gait Questionnaire
NIR	Near-Infrared
OD	Optical Density
OOB	Out-of-Bag
PCI	Phase coordination index
PD	Parkinson's Disease
PFC	Prefrontal Cortex
PFT	Phonemic Fluency Task
PIGD	Postural instability gait disorder
PKF	Peak Frequency
PPN	Pedunculopontine nucleus
PSD	Power Spectral Density
RBD	REM sleep behavior disorder
RF	Random Forest
RFem	Rectus Femoris
RMS	Root Mean Square
ROI	Region Of Interest
SCI	Scalp Coupling Index
SE	Shannon Entropy
SMA	Supplementary motor area
SNpc	Substantia nigra pars compacta
SpEn	Sample Entropy
SSc	Short Separation channels
SSC	Slope Sign Change
STD	Standard Deviation
STFT	Short-Time Fourier Transform

Abbreviation	Definition
STN	Subthalamic nucleus
SVM	Support Vector Machine
TA	Tibialis Anterior
tDCS	Transcranial Direct Current Stimulation
TDDR	Temporal Derivative Distribution Repair
TD	Time Domain
TF	Time-Frequency
TO	Toe Off
TUG	Timed Up and Go
WL	Wavelength
ZC	Zero Crossing

1 Parkinson's disease and Freezing of Gait

1.1 Parkinson's disease

PD is a progressive neurodegenerative disorder of the central nervous system, caused by the degeneration of dopaminergic neurons in the substantia nigra pars compacta (SNpc), which leads to a reduction in dopamine levels within the nigrostriatal pathway, crucial for the regulation of voluntary movement [1].

PD is clinically characterized by the main motor symptoms of bradykinesia, muscle rigidity, resting tremor, and postural instability. However, it is now widely recognized that PD is a multisystem disorder, with neurodegeneration extending beyond the dopaminergic system. Consequently, a broad spectrum of non-motor symptoms, including cognitive, affective, autonomic, and sleep-related disturbances, can accompany or even precede motor symptoms, contributing significantly to reduce patients' quality of life [2].

1.1.1 Neuropathology and pathophysiology

Post-mortem neuropathological examination reveals a severe depigmentation of neurons in the SNpc, the striatum, the globus pallidus and the thalamus, and the presence of Lewy bodies, abnormal inclusions composed of misfolded α-synuclein, a presynaptic protein that aggregates into insoluble fibrils [3][4].

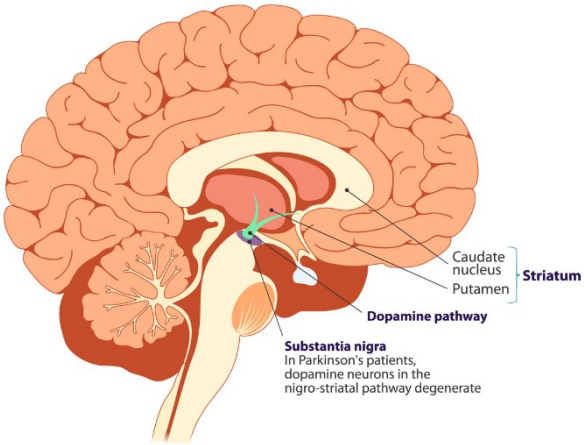

Figure 1.1 Neuroanatomy of the PD's most affected regions [5]

The Braak staging hypothesis proposes that α-synuclein pathology progresses in a predictable pattern, starting from the olfactory bulb and lower brainstem, and spreading to the midbrain and cerebral cortex [6]. This pattern aligns with the gradual emergence of non-motor and motor symptoms during disease progression.

The loss of dopaminergic neurons in the SNpc results in dopamine level reduction in the striatum (composed of caudate and putamen), unbalancing excitatory and inhibitory pathways within the basal ganglia circuitry. According to the Albin-DeLong model, this imbalance leads to an excessive inhibition of the thalamus and reduced activation of the motor cortex [7][8].

1.1.2 Clinical features

PD is a clinically heterogeneous disorder characterized by a wide range of symptoms, which are typically categorized as motor and non-motor *(Figure 1.2)*.

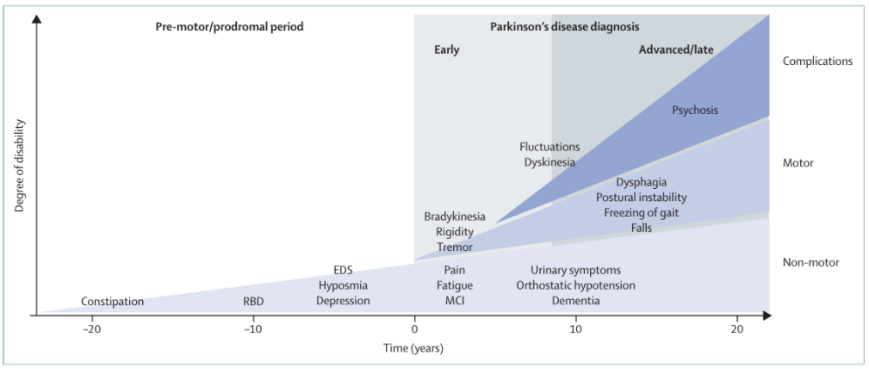

Figure 1.2 Clinical symptoms and time course of Parkinson's disease progression [1]

1.1.2.1 Non-motor symptoms

Non-motor symptoms often appear years before the onset of motor manifestations, offering potential biomarkers for early or prodromal PD [9]. They tend to persist and worsen as the disease advances, particularly in older patients, and represent a major determinant of quality of life.

Common non-motor features include:

- Constipation
- Olfactory dysfunction (hyposmia)
- REM sleep behavior disorder (RBD)
- Depression
- Autonomic disturbances

Their early recognition is crucial, as these symptoms may reflect the involvement of extranigral structures, in line with Braak's hypothesis of disease spread [10].

1.1.2.2 Motor symptoms

The core motor symptoms of PD have been recognized since the 19th century, with James Parkinson's original description in 1817 and further clinical delineation by Jean-Martin Charcot [11].

These manifestations typically include:

- Bradykinesia
- Muscle rigidity
- Resting tremors
- Postural instability
- Gait impairment

Since their expression varies among individuals, researchers and clinicians have devoted efforts into defining PD subtypes, such as tremor-dominant and non-tremor-dominant (or postural instability gait disorder, PIGD) [12].

1.1.3 Diagnosis

PD diagnosis is based on the recognition of its characteristic motor features and the exclusion of other parkinsonian syndromes.

The main diagnostic features include bradykinesia, in combination with either resting tremor or muscle rigidity. These symptoms usually present asymmetrically and respond to dopaminergic therapy, which further supports the diagnosis [13].

The Movement Disorder Society (MDS) Clinical Diagnostic Criteria, introduced by Postuma and colleagues [14], provides a standardized guide for PD diagnosis:

1. The identification of parkinsonism (bradykinesia plus rest tremor or rigidity)
2. The assessment of supportive criteria, exclusion criteria, and red flags.

Supportive criteria include a clear response to levodopa, the presence of levodopa-induced dyskinesias, or the presence of rest tremors, while exclusion criteria include features atypical for PD, such as early severe autonomic failure, early falls, or supranuclear gaze palsy.

1.1.3.1 Imaging

While neuroimaging is not used for PD diagnosis it can be helpful in uncertainty cases:

- Dopamine transporter single-photon emission computed tomography (DaT-SPECT) provides in vivo estimation of dopaminergic loss and it is useful to distinguish PD from conditions without nigrostriatal degeneration [15].
- Magnetic resonance imaging (MRI) is not specifically used to diagnose PD but can help excluding atypical or secondary parkinsonisms.
- Molecular imaging and biomarker research have shown promise in supporting early or differential diagnosis [16].

1.1.3.2 Clinical Rating Scales

Clinical evaluation of PD employs standardized rating instruments that quantify both motor and non-motor impairment.

The most important and widely used are the Hoehn and Yahr (H&Y) scale and the Movement Disorder Society-Unified Parkinson's Disease Rating Scale (MDS-UPDRS), which provide complementary information on disease severity and progression [17].

1.1.3.2.1 Hoehn and Yahr

The H&Y scale, first introduced in 1967, remains one of the simplest and most reproducible measures of global disease stage [18].

It classifies PD severity into five stages, ranging from unilateral involvement (stage 1) to complete dependence or confinement to a wheelchair or bed (stage 5). Intermediate stages reflect increasing bilateral involvement and postural instability. Higher stages correlate with

greater motor disability and a higher likelihood of non-motor complications such as cognitive decline and depression [19].

A modified version (mH&Y), introduced in the 1990s, adds 0.5-point increments, improving sensitivity to clinical changes and better capturing the transition between stages 2 and 3 [19].

H&Y Stage	mH&Y Stage	Clinical Description
1	1	Unilateral involvement only, minimal or no functional disability
1.5		Unilateral and axial involvement
2	2	Bilateral or midline involvement without impairment of balance
2.5		Mild bilateral disease with recovery on pull test
3	3	Mild to moderate bilateral disease with postural instability; physically independent
4	4	Severe disability; still able to walk or stand unassisted
5	5	Wheelchair-bound or bedridden unless aided

Table 1.1 H&Y and mH&Y scales.

1.1.3.2.2 Movement Disorder Society-Unified Parkinson's Disease Rating Scale

The MDS-UPDRS represents the most comprehensive and widely validated tool for assessing Parkinson's disease [17].

The scale is divided into four parts, covering the full spectrum of PD manifestations:

- Part I - Non-Motor Experiences of Daily Living: Assesses behaviors and symptoms such as cognition, mood, sleep, and autonomic function. Subsection IA is clinician-rated, while IB is patient-reported.
- Part II - Motor Experiences of Daily Living: Evaluates how motor symptoms affect routine activities, independence, and quality of life.
- Part III - Motor Examination: Involves assessment of rigidity, bradykinesia, tremor, gait, and posture.
- Part IV - Motor Complications: Captures fluctuations, dyskinesias, and dystonia, summarizing their impact over the previous week.

1.1.4 Treatments

The treatment of PD is primarily symptomatic, aiming to restore dopaminergic function and alleviate both motor and non-motor symptoms. Despite significant therapeutic advances, no current intervention is able to reverse the underlying neurodegenerative process [1].

1.1.4.1 Pharmacological therapy

The cornerstone of PD management is dopaminergic replacement therapy, most commonly with levodopa, a dopamine precursor administered in combination with a peripheral

decarboxylase inhibitor such as carbidopa or benserazide, which remains the most effective medication for improving motor symptoms and quality of life in PD patients [20].

However, with chronic use, complications such as motor fluctuations and levodopa-induced dyskinesias often emerge, typically after several years of therapy [21].

Alternative pharmacological approaches are dopamine agonists, that directly stimulate dopamine receptors, and monoamine oxidase B (MAO-B) inhibitors and catechol-O-methyltransferase (COMT) inhibitors, which reduce dopamine breakdown, prolonging its effect. These agents are often used as adjunctive or early monotherapy in younger patients to delay levodopa-related complications [22].

For non-motor symptoms, pharmacological treatments are managed according to symptom type: antidepressants for mood disorders, cholinesterase inhibitors for cognitive impairment, and medications targeting autonomic or sleep disturbance [2].

1.1.4.2 Surgical therapy

When medical treatment becomes insufficient to control motor complications, deep brain stimulation (DBS) is often used as a surgical option. DBS consists in high-frequency electrical stimulation of specific subcortical targets, as the subthalamic nucleus (STN).

This intervention restores the functional balance of the basal ganglia network, leading to significant improvement in motor symptoms and reduction of medication requirements [23][24].

1.1.4.3 Rehabilitation and non-pharmacological management

A multidisciplinary approach is fundamental in PD management. Physical therapy helps maintain mobility, balance and independence, while speech and swallowing therapy address dysarthria and dysphagia.

Regular exercise and physiotherapy have been shown to enhance motor performance and may exert neuroprotective effects by promoting neuroplasticity [25][26].

Moreover, cognitive-behavioral interventions and patient education can mitigate anxiety, depression, and apathy, contributing to overall quality of life.

Although current treatments are highly effective in alleviating symptoms, disease progression ultimately leads to increasing disability. Emerging therapeutic strategies, including gene therapy, cell replacement, and neuroprotective agents targeting α-synuclein aggregation, are under investigation but remain experimental [27].

1.2 Freezing of Gait

1.2.1 Clinical Description

FoG is defined as a “brief, episodic absence or marked reduction of forward progression of the feet despite the intention to walk” [28]. During a FoG episode, patients often describe the feeling that their feet are “glued to the floor”, unable to initiate or continue stepping.

FoG episodes usually last from a few to tens of seconds, and their unpredictable occurrence can lead to loss of balance and falls, representing a sensitive problem for the mobility and independence [29].

Clinically, FoG is a heterogeneous symptom, which can manifest as:

- Akinetic FoG, where stepping completely ceases.
- Kinetic FoG, in which ineffective, trembling, or shuffling leg movements occur without meaningful forward motion.
- A mixed form, with alternating patterns during a single episode [29].

FoG typically occurs under specific triggering conditions, such as gait initiation, turning, approaching narrow passages like doorways, or in dual-task situations that requires greater cognitive load. Emotional states like stress or anxiety can facilitate its occurrence, while external cues, such as rhythmic auditory or visual signals, may help overcome the freezing episode [30].

The prevalence of FoG increases with disease duration and severity, affecting approximately 30-50% of patients with advanced PD [31]. It is also important to specify that not all PD patients develop FoG, suggesting distinct neurophysiological or cognitive profiles that predispose certain individuals.

1.2.2 Pathophysiology

The pathophysiology of FoG extends beyond the typical PD dopaminergic deficit. FoG is thought to be caused by interruption in communication between cortical, subcortical, and brainstem locomotor regions, that leads to a failure in the transition from motor planning to motor execution [32].

Functional imaging and electrophysiological studies have identified abnormal connectivity within a distributed gait network that includes the supplementary motor area (SMA) and pre-SMA (involved in movement initiation), basal ganglia, and mesencephalic locomotor region (MLR), particularly the pedunculopontine nucleus (PPN) [33][34][35].

Disruption of these circuits impairs the generation of rhythmic stepping, forcing patients to rely on cognitive control to maintain movement. When attentional or executive resources are taxed, such as during DT, this compensatory mechanism fails, triggering a FoG episode [34][36].

1.2.3 Assessment and Quantification

The assessment of FoG is challenging because, given its episodic and context-dependent nature, it may not occur during routine clinical examinations, requiring the use of standardized scales or FoG-eliciting protocols to capture its presence and severity. Clinical evaluation relies on both subjective reports and objective observation.

1.2.3.1 Clinical assessment

The most commonly used tool is the New Freezing of Gait Questionnaire (NFOG-Q), which combines patient self-report and video-based examples to evaluate the frequency, duration, and functional impact of FoG [37]. It provides a semi-quantitative measure that correlates well with disease severity and motor fluctuations [38].

In addition, FoG severity is estimated through two specific items of the MDS-UPDRS, particularly item 2.13 (freezing during daily activities) and item 3.11 (freezing during examination) [17].

Although these clinical instruments are simple and widely adopted, they depend on patient recollection and examiner interpretation, which may limit reproducibility and ecological validity.

1.2.3.2 FoG eliciting task-based testing

To overcome these limitations, provocative gait tasks are often employed in laboratory or clinical settings. Such protocols include gait initiation, turning, passing through narrow doorways, or dual-task walking, as these are the conditions that could most likely elicit [29][39].

Combining these tasks with video recordings allows for standardized expert rating of FoG episodes, enhancing inter-rater reliability. However, these approaches remain time-consuming and environment dependent [39][40].

1.2.3.3 Instrumented assessment

In recent years, several instrumented approaches have been developed to provide objective quantification of FoG episodes using wearable sensors or physiological recordings. These systems, typically based on IMUs, or electrophysiological signals, allow continuous monitoring and characterization of gait dynamics in both clinical and real-world conditions [41][42].

Although these methods have significantly advanced the understanding of FoG, their clinical adoption remains limited, and further research is needed to optimize detection algorithms and integrate multimodal data.

1.2.4 Rehabilitation and Management Strategies

The management of freezing remains particularly complex, as it often persists despite optimized dopaminergic therapy and reflects mechanisms that extend beyond the dopaminergic system [29][32].

Consequently, treatment focuses on individualized, multidisciplinary strategies aimed at compensating for the disrupted coordination between motor and cognitive systems.

1.2.4.1 Pharmacological and surgical interventions

Medication adjustments can reduce episodes related to “off” fluctuations, but freezing frequently appears in “on” states. Adjunctive treatments such as MAO-B inhibitors, dopamine agonists, or amantadine have shown inconsistent results, and no specific drug has proven consistently effective [31].

Surgical stimulation of subcortical structures may alleviate certain gait impairments, but results on freezing are variable. Experimental stimulation of the PPN has yielded only partial and heterogeneous benefits [43][44].

1.2.4.2 Cueing and physiotherapeutic interventions

External cueing remains the most effective non-pharmacological strategy to overcome freezing. There are three kinds of external cueing: visual, auditory, and tactile cues help restore rhythmic stepping and movement initiation by providing external stimuli that substitutes impaired internal control [45].

Physiotherapy programs emphasize task-oriented gait training, dual-task exercises, and compensatory strategies to re-establish movement continuity, also exploiting new technologies, as virtual reality and augmented feedback systems to simulate triggering contexts, improving adaptability and motor-cognitive coordination [46].

1.2.4.3 Cognitive and behavioral approaches

Since freezing is strongly influenced by deficits in executive control and attention, cognitive interventions have become increasingly relevant. Training focused on attention shifting, response inhibition, and working memory can strengthen compensatory control of gait [36][47].

Behavioral strategies such as mental imagery, rhythmic counting, or large amplitude stepping help reinitiate movement during episodes, while interventions targeting anxiety and stress can reduce their occurrence [48].

1.2.4.4 Multimodal rehabilitation

Current evidence shows the effect of integrative rehabilitation combining physical, cognitive, and technological components, merging cueing and cognitive engagement into personalized frameworks designed to address the multiple dimensions of freezing [32].

2 Biosignals

2.1 Functional Near-Infrared Spectroscopy

2.1.1 Introduction and physiological basis

fNIRS is a non-invasive optical neuroimaging technique that measures brain activity indirectly by detecting changes in cerebral blood oxygenation. It relies on the physiological principle of neurovascular coupling, according to which localized increase in neuronal activity leads to corresponding changes in regional cerebral blood flow and oxygen consumption [49][50].

During neuronal activation, energy demand increases and triggers a compensatory vascular response mediated by neurovascular and metabolic mechanisms, that result in an increase in oxyhemoglobin (HbO) and a decrease in deoxyhemoglobin (HbR) concentrations in the local microvasculature. These hemodynamic changes, which occur within a few seconds of stimulus onset, serve as indirect markers of neuronal activity [51][52].

In order to probe cortical hemodynamics, fNIRS exploits this coupling by using near-infrared (NIR) light, typically in the 700-900 nm range, where biological tissues such as skin, skull, and cerebrospinal fluid (CSF) exhibit minimal absorption. Within this optical window, HbO and HbR are the primary chromophores, each with distinct absorption spectra. By measuring changes in the intensity of light reflected or transmitted through cortical tissue, fNIRS can estimate variations in their relative concentrations and, consequently, infer localized brain activation patterns [53].

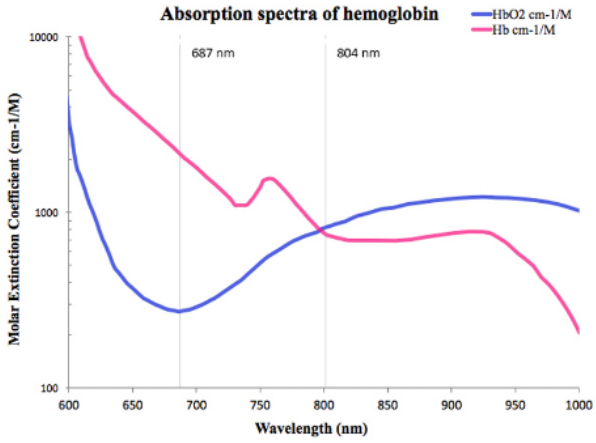

Figure 2.1 Absorption Spectra of Hemoglobin [54]

The technique measures hemodynamic responses in the superficial layers of the cortex, generally up to a depth of 1-2 cm beneath the scalp, depending on the distance between light sources and detectors. Although it does not provide direct neuronal recordings as electroencephalogram (EEG) does, or the whole-brain spatial coverage of fMRI, fNIRS offers a unique balance between temporal resolution, portability, and tolerance to motion, making it particularly suitable for studies in naturalistic environments, including motor control and gait-related paradigms [55][56].

2.1.2 Physical and Optical Principles of fNIRS

The fNIRS signal originates from the interaction between near-infrared light and biological tissue, a process governed primarily by absorption and scattering phenomena. When NIR

photons enter the scalp, they undergo multiple scattering events due to the heterogeneous composition of the head, including scalp, skull, CSF and cortical tissue, resulting in a diffuse propagation of light.

A fraction of the photons re-emerges and can be detected at the scalp surface, carrying information about the optical properties of the underlying tissue.

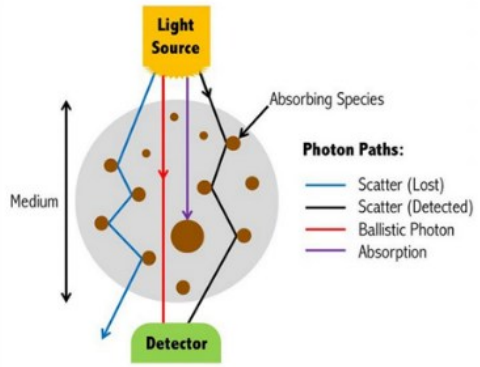

Figure 2.2 Schematic representation of photon scattering and absorption in head tissues during fNIRS measurement. [57]

In the NIR spectral window, tissue absorption is relatively low, allowing photons to penetrate up to a few centimeters beneath the surface before being either absorbed or reflected. Within this window, the main absorbers are HbO and HbR, whose distinct absorption spectra *(Figure 2.1)* form the basis for estimating their relative concentration changes.

Scattering, on the other hand, is primarily due to variations in refractive index between cellular structures and interstitial fluid, and it dominates over absorption by several orders of magnitude. Consequently, light propagation in biological tissue is best described as a diffusion process rather than simple straight-line transmission.

2.1.2.1 The "Banana-Shaped" Sensitivity Profile

Due to this highly scattering nature of biological tissue, photons emitted from a source follow complex, random trajectories before reaching a detector. The ensemble of these photon paths defines a characteristic "banana-shaped" sensitivity profile *(Figure 2.3)*, with the highest sensitivity located midway between the source and detector and extending to a depth of approximately half their separation distance. This geometry determines the cortical region that contributes most strongly to the measured signal and explains why fNIRS is mainly sensitive to superficial cortical layers [58][59].

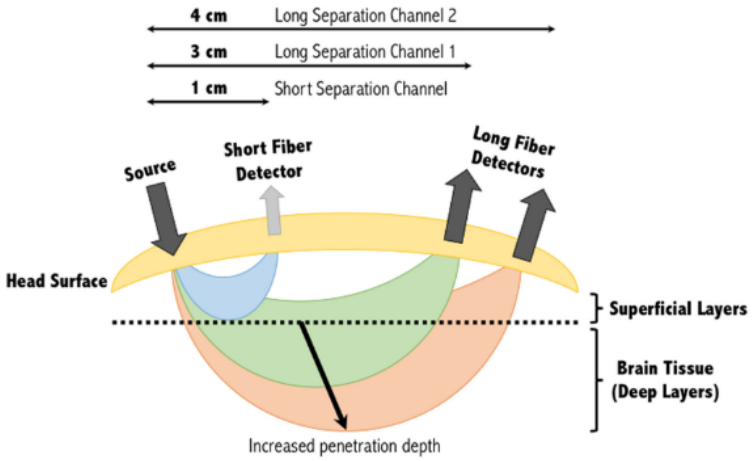

Figure 2.3 Schematic representation of the "banana-shaped" light path between a source and three detectors at different distances [57]

2.1.2.2 The Modified Beer–Lambert Law

To relate measured light intensity to changes in chromophore concentration, fNIRS relies on the Modified Beer-Lambert Law (MBLL) [60]. This model assumes that the attenuation of light intensity (ΔA) is proportional to the pathlength (L) through the medium and to the change in the medium absorption, which depends on the variation in HbO and HbR concentrations:

$$\Delta A(\lambda) = \varepsilon_{\mathrm{HbO}}(\lambda) \cdot \Delta[HbO] \cdot L \cdot DPF + \varepsilon_{\mathrm{HbR}}(\lambda) \cdot \Delta[HbR] \cdot L \cdot DPF$$

Equation 2.1 Modified Beer-Lambert Law (MBLL)

where $\varepsilon_{\mathrm{HbO}}$ and $\varepsilon_{\mathrm{HbR}}$ are the molar extinction coefficients of HbO and HbR at wavelength λ, and DPF (Differential Pathlength Factor) accounts for the increased photon pathlength due to scattering. The DPF depends on wavelength, age, and tissue type, and it is typically determined empirically or taken from literature values [61].

2.1.2.3 Limitations of Simplified Optical Models

Although the MBLL provides a convenient linear approximation for continuous-wave systems [62], it rests on simplifying assumptions, like homogeneous tissue optical properties, constant scattering, and a well-defined mean optical pathlength. In reality, light propagation in the head is far more complex, with different tissue layers contributing differently to absorption and scattering [63][64].

For this reason, more sophisticated models based on diffusion approximation have been developed to more accurately describe photon migration in tissue.

2.1.2.4 Advanced 3D Reconstruction in fNIRS

To overcome the limitations inherent in simplified models such as the MBLL, more advanced approaches conceptualize fNIRS as a tomographic imaging problem. These methods, commonly referred to as diffuse optical tomography (DOT) or 3D fNIRS reconstruction, aim to estimate spatial maps of absorption changes (and therefore hemodynamic activity) within the cortical volume or surface from scalp-measured optical signals.

2.1.2.4.1 Forward modeling: Monte Carlo and diffusion-based simulations

The forward problem consists in modeling how local variations in the absorption coefficient within the head affect the measured optical density changes at each detector. This is expressed through a sensitivity matrix that quantifies the contribution of each voxel to each source-detector pair.

Monte Carlo photon propagation simulations are widely recognized as the gold standard for modeling light transport in heterogeneous biological tissues [64]. By randomly sampling photon trajectories through the different tissue layers (scalp, skull, CSF, gray and white matter) these simulations compute maps of fluence and sensitivity profiles for each channel.

Each layer is characterized by specific optical properties, as the absorption (μ_a) and reduced scattering (μ_s') coefficients, typically derived from literature or experimental measurements [65][66].

These parameters, summarized in *Table 2.1* , are essential inputs for the Monte Carlo model and critically determine the spatial distribution of light fluence and the resulting sensitivity of each channel.

Tissue	μ_a @760 nm	μ'_s @760 nm	μ_a @850 nm	μ'_s @850 nm
Background	0.0000	0.000	0.0000	0.000
Scalp	0.0159	10.00	0.0191	8.25
Skull	0.0101	12.50	0.0136	10.75
CSF	0.0004	0.125	0.0026	0.125
Gray matter	0.0178	15.625	0.0186	13.875
White matter	0.0178	15.625	0.0186	13.875

Table 2.1 Optical properties of cerebral tissues at two different wavelengths [65][67]

Alternative numerical implementations rely on the diffusion approximation of the radiative transport equation, valid under the condition of high scattering ($\mu_s' \gg \mu_a$), and are often solved using finite element or finite difference methods [63][64].

2.1.2.4.2 Inverse reconstruction: MNE, MEM and regularization approaches

Once the forward sensitivity matrix is computed, the inverse problem involves estimating the spatial distribution of absorption changes that best explain the measured optical signals. This is typically expressed as:

$$Y = AX + e$$

where Y represents the measured changes in optical density, A the sensitivity matrix, X the unknown HbO/HbR changes across voxels, and e the residual error term.

Among the most common inversion strategies are Minimum Norm Estimate (MNE) and Maximum Entropy on the Mean (MEM) which differ in the constraints they impose on the solution [68][69].

- MNE seeks the solution with minimal overall energy by minimizing the cost function

$$\| AX - Y \|^2 + \lambda \| X \|^2$$

where λ controls regularization strength. Depth-weighting or spatial priors are often applied to mitigate the bias toward superficial cortex [59].

- MEM extends this approach by introducing entropy-based priors, promoting spatial smoothness and physiologically plausible activation patterns [69][70]. These methods have shown improved localization and reduced spatial blurring compared to standard MNE, particularly under low signal-to-noise conditions.

Because the inverse problem is intrinsically ill-posed, proper regularization and prior information (e.g., anatomical constraints or noise covariance estimates) are essential for obtaining stable and interpretable reconstructions.

2.1.3 Preprocessing and Data Analysis Pipeline

Building upon these modeling principles, the following step in an fNIRS study consists of preparing and analyzing the recorded optical data to extract physiologically meaningful information. The preprocessing pipeline aims to remove artifacts and physiological confounds while transforming raw light intensity signals into reliable estimates of hemodynamic activity. Although specific implementations vary across toolboxes, most frameworks share a common sequence of operations [56][71][72].

2.1.3.1 Raw data inspection and channel quality control

The first stage involves visual and automated inspection of the raw light intensity signals. Channels affected by poor optode-scalp coupling, detector saturation, or excessive noise are identified and excluded.

Signal quality can be quantified using indices such as the scalp coupling index (SCI) or the coefficient of variation (CoV) across time [73]:

- SCI quantifies the quality of optode-scalp contact in fNIRS recordings by evaluating the correlation between cardiac oscillations detected by paired sources and detectors [74]. It is computed as the Pearson correlation coefficient between two short time windows of the raw light intensity signals, filtered within the cardiac frequency band (≈ 0.5-2.5 Hz):

$$SCI = \frac{cov\left(I_{\lambda_1}, I_{\lambda_2}\right)}{\sigma_{I_{\lambda_1}} \sigma_{I_{\lambda_2}}}$$

Equation 2.2 Scalp Coupling index

  where I_{λ_1} and I_{λ_2} are the filtered intensity signals at the two wavelengths, cov is the covariance, and σ denotes the standard deviation.

- CoV expresses the relative variability of a signal with respect to its mean and is used as a normalized index of signal stability:

$$\mathrm{CoV} = \frac{\sigma_x}{\mu_x}$$

Equation 2.3 Coefficient of variation

where σ_x is the standard deviation and μ_x is the mean of the signal x. In fNIRS preprocessing, the CoV is typically computed on raw intensity or optical density (OD) data to identify noisy channels.

This preliminary step ensures that subsequent corrections operate only on physiologically plausible data.

2.1.3.2 Conversion from intensity to optical density

Clean intensity signals are converted to OD through a logarithmic transformation, which linearizes the relationship between measured intensity and tissue absorption.

This step standardizes the data and allows artifact correction and filtering to operate in the same units across wavelengths and channels [62].

2.1.3.3 Motion artifact detection and correction

Body movement such as head movement or activity tasks can introduce artifacts in the data. Generally, they can be detected by looking for transient spikes or baseline shifts that obscure the underlying hemodynamic signal.

Detection strategies rely on identifying abrupt signal changes, typically via amplitude or derivative thresholds, while correction methods include spline interpolation, wavelet filtering, or temporal principal component analysis [72][75].

2.1.3.4 Filtering and physiological noise attenuation

Motion correction artifacts are only one of the problems that need to be considered: slow drifts and physiological rhythms, such as cardiac, respiratory, or Mayer wave oscillations also have to be removed, and this is often done by applying a band-pass filter, typically in the range 0.01-0.2 Hz, to isolate the frequency band of the hemodynamic response [76].

In addition, systemic hemodynamics unrelated to neural activity can be mitigated through short-separation regression, where signals from nearby detectors (≤ 1.5 cm from the source) are used as nuisance regressors to remove superficial components [77][78].

At such short distances, the detected light does not penetrate deep enough to reach cortical tissue and thus primarily captures superficial physiological components, including scalp blood flow and systemic oscillations, rather than neural hemodynamic responses.

2.1.3.5 Conversion to hemoglobin concentration changes

Once preprocessed, the OD signals are converted into relative concentration changes of HbO and HbR using MBLL**,** described in 2.1.2.2, or 3D fNIRS reconstruction, described in 2.1.2.4.

This step combines the wavelength-dependent extinction coefficients and DPF to estimate the local variations in absorption associated with cortical hemodynamics [61][79].

2.1.3.6 Baseline correction and epoching

For event-related or block-design paradigms, the continuous Δ[HbO]/Δ[HbR] signals are segmented into epochs aligned to stimulus onsets.

A baseline period preceding each event is often subtracted to correct for residual slow trends. This normalization enhances comparability across conditions and participants [52].

2.1.3.7 First-level statistical analysis

Task-related activations are typically modeled using the Generalized Linear Model (GLM) framework [80].

Each condition is represented by a regressor convolved with a canonical hemodynamic response function (HRF), with also short-separation and motion regressors that can be included as nuisance terms to further reduce non-neural variance.

The resulting beta coefficients (β) quantify the amplitude of task-evoked responses for each channel or, in reconstructed datasets, for each cortical vertex [69].

These β-values are then used in group-level analyses for statistical comparison across conditions or populations [81].

2.1.3.8 Time-Series and Functional Connectivity Analysis in fNIRS

Following signal preprocessing, the temporal evolution of the fNIRS signal can be further analyzed to extract features that describe regional activity and inter-regional relationships. These features are widely used in both experimental and machine learning contexts, providing quantitative metrics that reflect brain dynamics over time [82][83].

2.1.3.8.1 ROI-level time-series representation

A common approach to reduce data dimensionality and increase physiological interpretability is to aggregate voxel- or channel-level signals within predefined functional networks or regions of interest (ROIs). Signals can be averaged across all voxels belonging to a certain ROI, in order to produce one representative time series per ROI, summarizing its overall hemodynamic activity and facilitating subsequent computation of inter-ROI relationships.

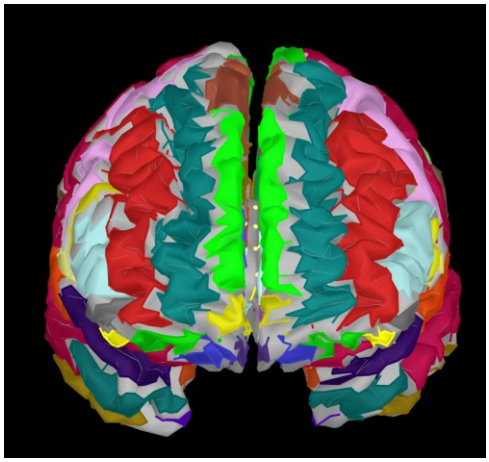

Figure 2.4 AAL3 atlas: standard brain parcellation into ROIs.

2.1.3.8.2 Time domain (TD) feature extraction

Once network-level time series are obtained, the signal is often segmented into short, consecutive time windows (commonly 2-10 s) using a sliding-window approach [84][85].

Within each window, simple descriptive statistics, such as the mean, standard deviation, or slope of the HbO signal, are computed to quantify transient activation levels [52][86].

The mean value is particularly popular as it reflects the average network activation in each time segment, providing a compact feature well suited for classification frameworks. Shorter windows yield higher temporal resolution, allowing detection of rapid fluctuations, whereas longer windows improve signal-to-noise ratio at the cost of temporal precision [84].

In addition to statistical moments, several studies have extracted alternative time-series features such as peak amplitude, range, variance (VAR), or higher-order moments (skewness, kurtosis), which may capture non-linear aspects of the hemodynamic response [83][87].

2.1.3.8.3 Functional connectivity features

Beyond local activation, fNIRS time series can be used to estimate functional connectivity, reflecting the temporal coupling between signals recorded from distinct cortical regions or networks.

The most common metric is the Pearson correlation coefficient between HbO signals, computed either over the entire recording or within sliding windows to assess dynamic connectivity [85][88].

This correlation quantifies the degree to which fluctuations in one region co-occur with those in another, providing an indirect measure of network communication.

When computed in short, overlapping windows, correlation matrices can reveal time-varying connectivity patterns analogous to dynamic functional connectivity in fMRI [89]. For statistical stability, correlation values are often Fisher-z-transformed prior to analysis [88].

Functional connectivity-based features have been shown to improve the discrimination of cognitive states and disease conditions compared with univariate activation features alone [90][91]. Combining activation-based and connectivity-based features therefore provides a richer representation of the underlying neural processes.

2.1.4 Instrumentation

2.1.4.1 General system architecture

A typical fNIRS system comprises light sources and detectors arranged on the head through a cap or flexible holder. Each source-detector pair defines a measurement channel sensitive to hemodynamic changes in the cortical region beneath their midpoint [53][62].

Depending on the modulation scheme used for light emission and detection, fNIRS instruments can be classified as:

- Continuous-Wave (CW): use constant-intensity light and measure only relative changes in detected intensity. CW systems are the most common and cost-effective configuration for cognitive and motor neuroscience studies.

- FD: use amplitude-modulated light and detect both amplitude and phase shifts, allowing absolute quantification of absorption and scattering.
- TD: emit picosecond light pulses and measure photon arrival distributions, offering superior depth resolution but requiring complex hardware.

Most modern neuroimaging applications employ CW systems, which balance portability, cost, and robustness, particularly in studies involving motion or naturalistic behavior [56].

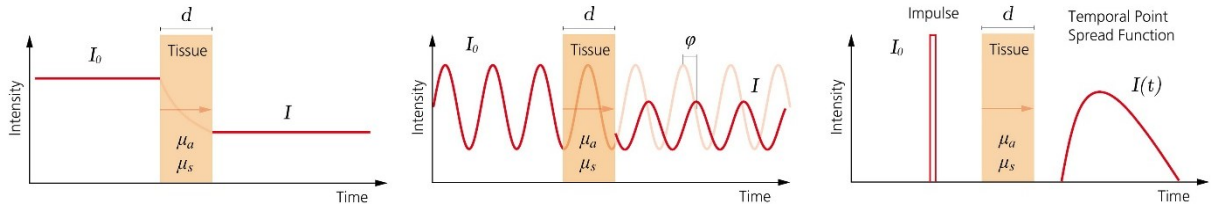

Figure 2.5 Representation of the three different NIRS techniques: CW (left), FD (middle), TD (right) [92]

2.1.4.2 Core components and design considerations

Each source emits NIR light into the tissue, and each detector records the portion of that light that has diffused through the underlying layers and re-emerged at the surface. The region of overlap between the emitted and detected light paths defines the channel's sensitivity volume, which corresponds to the cortical area probed.

2.1.4.2.1 Sources

The light sources are usually light-emitting diodes (LEDs) or laser diodes that operate in the 700-900 nm range, a spectral window where absorption by water and lipids is minimal and where hemoglobin is the main absorber (see *Figure 2.1*). Two wavelengths, commonly around 760 and 850 nm, are typically employed to estimate HbO and HbR concentration changes.

2.1.4.2.2 Detectors

The detectors are positioned at a fixed distance from the sources and are generally implemented as silicon or avalanche photodiodes, chosen for their high sensitivity and fast response. They convert the collected light intensity into voltage signals proportional to photon flux. The balance between detector gain, noise performance, and saturation limits is critical for achieving optimal signal quality, particularly in portable and high-density recording setups.

2.1.4.2.3 Design considerations

The distance between sources and detectors, known as the source-detector separation, is a key determinant of both sensitivity and penetration depth. Standard separations of 2.5-3.5 cm allow the measurement of hemodynamic activity from cortical regions approximately 1-1.5 cm beneath the scalp. Short-separation pairs (typically 8-15 mm) are often included to record signals from superficial tissues such as scalp and skull, which can later be used to regress out systemic artifacts [77].

Optodes are usually placed according to standardized coordinate systems, such as the international 10-20 or 10-5 EEG layouts, ensuring reproducibility across subjects and compatibility with anatomical atlases. Optode holders or caps are designed to maintain stable

contact with the scalp throughout the experiment, minimizing motion-related signal loss, and are often available in different sizes to accommodate variations in head circumference.

Data quality depends heavily on the optode-scalp coupling, as even small air gaps or hair interference can significantly attenuate the detected signal. For this reason, modern systems provide real-time feedback on channel quality, allowing the operator to adjust optodes before or during data collection.

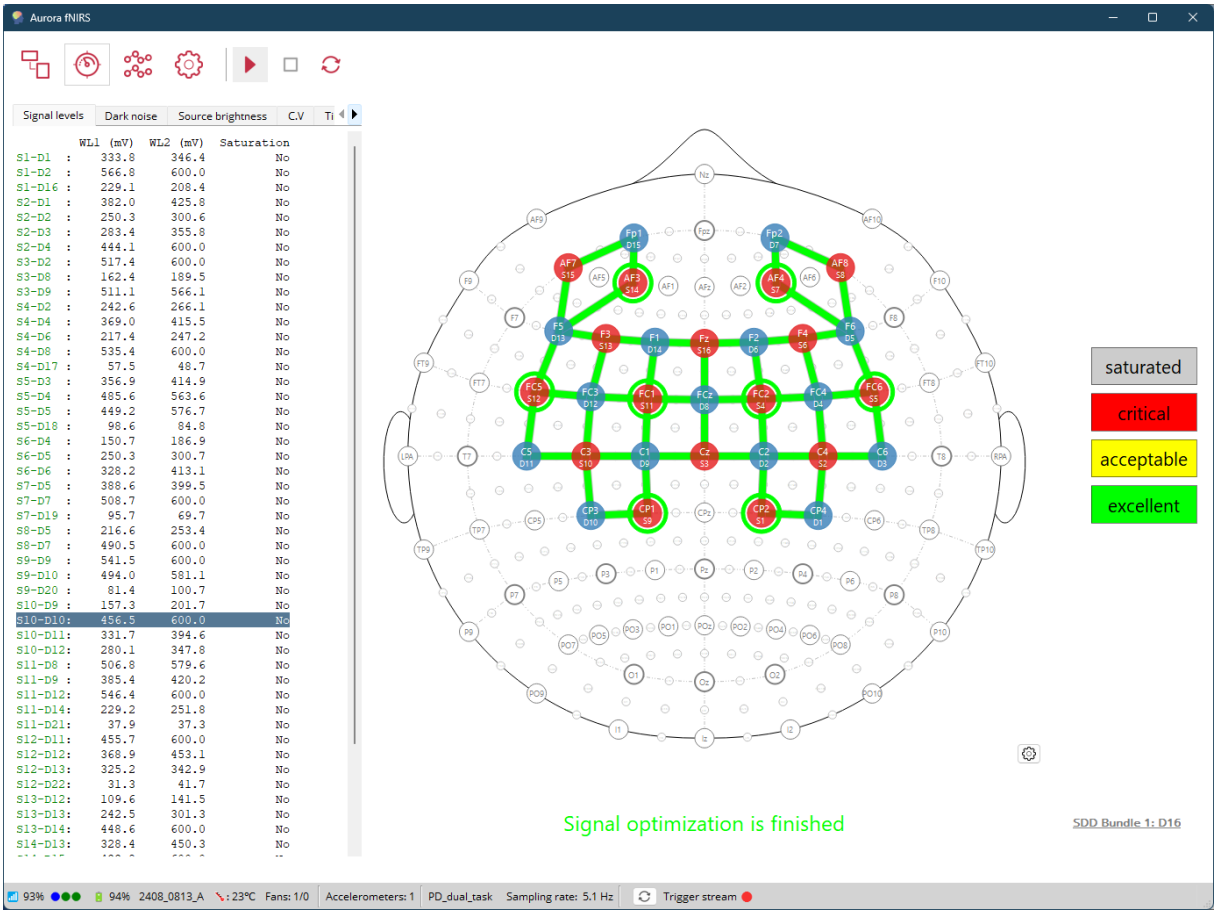

Figure 2.6 Example of channel quality feedback provided by a NIRS acquisition system [93]

Sampling frequencies in continuous-wave systems typically range between 5 and 20 Hz, sufficient to capture slow hemodynamic fluctuations occurring over several seconds.

Together with advances in miniaturized optoelectronics and wireless communication, these design features have led to highly portable and motion-tolerant fNIRS systems that are well suited for ecological or ambulatory experimental settings [56].

2.2 Surface Electromyography

sEMG is a non-invasive technique that provides a window into the neuromuscular system by recording, at the skin surface, the electrical activity generated by muscle fibers during contraction.

Because of these characteristics, sEMG has become a cornerstone in studies of human motor control and rehabilitation. It is widely used in gait analysis, sports science and human-machine interfaces to quantify muscle activation patterns, assess coordination, or control assistive devices [94][95].

From a methodological perspective, sEMG lies at the intersection of physiology and engineering: the recorded waveform reflects motor-unit recruitment and firing behavior, while proper processing (e.g., filtering, rectification, normalization) is required to obtain interpretable measures [96][97].

Over the years, several initiatives have provided guidelines for standardized data collection, including the SENIAM project [98], which remains the reference for electrode placement and reporting, particularly for lower-limb muscles. As a result, sEMG today represents one of the most accessible and informative tools to study human movement, bridging neural control and biomechanical execution.

2.2.1 Physiological principles of the sEMG signal

2.2.1.1 Motor unit physiology

The fundamental source of the sEMG signal is the electrical activity generated by motor units, the smallest functional components of the neuromuscular system, each composed of a single α-motoneuron and the muscle fibers it innervates [99].

When the motoneuron fires, all the fibers belonging to that unit depolarize almost simultaneously, producing an action potential that travels along each fiber's membrane, or sarcolemma, in both directions from the innervation zone toward the tendons [96][97].

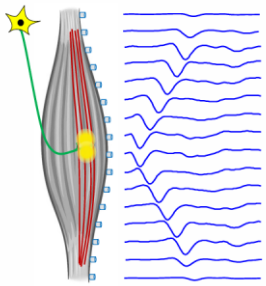

Figure 2.7 Motor unit action potential (MUAP) propagation along muscle fibers [100]

Motor-unit recruitment follows Henneman's size principle: during weak contractions, small, fatigue-resistant units are recruited first; stronger efforts progressively add larger, fast-twitch units [101].

As contraction intensity increases, muscle force rises through two mechanisms:

1. an increase in the number of recruited motor units
2. an increase in the firing rate (discharge rate) of active units [102].

At low percentages of the maximum voluntary contraction (MVC), in which almost all muscle fibers contracts, force modulation relies predominantly on recruitment; at higher intensities, it depends more on firing rate increases and unit synchronization. *(Figure 2.8)*.

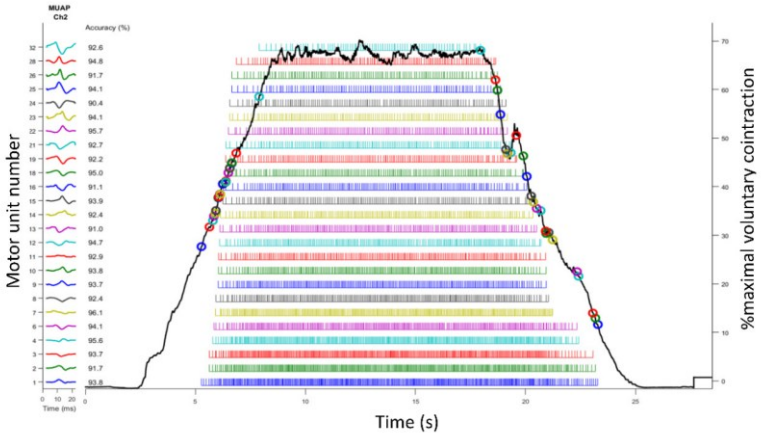

Figure 2.8 Variation in the number of recruited motor units and their firing rate as a function of the percentage of MVC [103].

This hierarchical organization ensures smooth and efficient control of muscle force and explains why the EMG signal reflects the neural strategies used by the central nervous system: changes in recruitment, rate coding, or synchronization directly modulate the electrical activity measurable at the skin surface.

2.2.1.2 Generation and propagation of the EMG signal

When an action potential propagates along a muscle fiber, ionic currents create small extracellular potential differences. The superposition of these contributions across the fibers of a motor unit forms the MUAP, detectable by surface electrodes placed above the muscle [97].

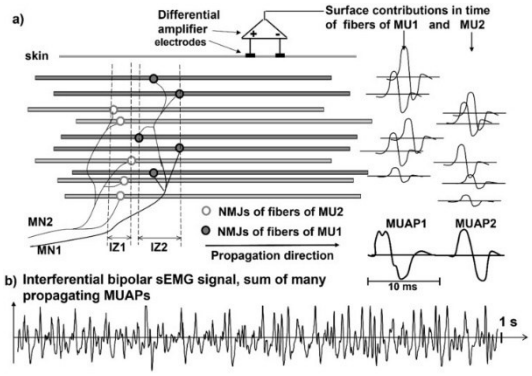

Figure 2.9 Schematic process of the spatial and temporal summation of MUAPs [104]

During voluntary movement, many motor units fire asynchronously and repeatedly; their MUAPs sum in space and time, producing the characteristic interference pattern observed in sEMG [99][105].

Although individual electrical events last only a few milliseconds, typical propagation velocities in skeletal muscle (≈ 3-5 m/s) mean that multiple action potentials coexist and interact at any instant, giving rise to the rich temporal structure of the sEMG trace [97].

2.2.2 Characteristics and sources of variability in the sEMG signal

The surface EMG signal represents the combined electrical manifestation of numerous MUAPs, recorded through the filtering layers of tissue between muscle and skin.

Although its physiological origin lies in the activation of individual fibers, the observed waveform is a composite signal shaped by both biological and technical factors [97][99].

Understanding these influences is essential to correctly interpret EMG data and ensure that variations in the signal correspond to genuine physiological differences rather than measurement artefacts.

2.2.2.1 General characteristics of the sEMG signal

The raw sEMG is a stochastic, approximately zero-mean signal characterized by bursts of activity during muscle contraction and near-flat segments during relaxation. Its amplitude typically ranges from a few hundred microvolts to a few millivolts peak-to-peak, depending on muscle size, contraction level, and electrode placement [105][106].

Because sEMG reflects the summation of many asynchronous motor-unit discharges, its waveform lacks a regular periodic structure and instead resembles a broad-band stochastic signal.

In the frequency domain, most of the signal's power is contained between 20 and 400-500 Hz, with dominant components usually concentrated in the 50-150 Hz range [97][99]. Frequencies below approximately 10-20 Hz are generally attributed to movement artefacts or baseline drift, while components above 400-500 Hz are strongly attenuated by the conductive tissues.

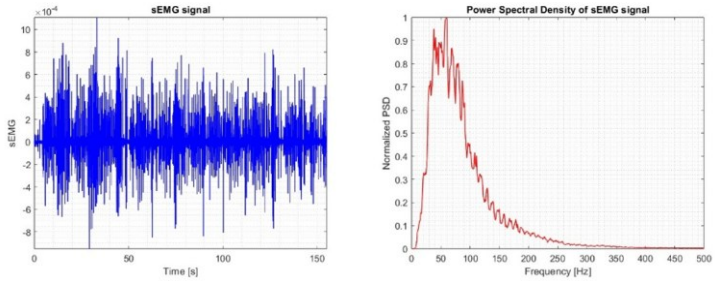

Figure 2.10 Example of sEMG signal and his power spectral density (PSD)

The amplitude of the sEMG increases with muscle force because stronger contractions involve the recruitment of more motor units and higher firing rates. However, this relationship is not perfectly linear across the entire force range, because of phase cancellation and changes in synchronization that can alter the summed potential [99].

2.2.2.2 Physiological factors influencing signal morphology

Several physiological characteristics of the muscle and surrounding tissues modify the shape, amplitude, and PSD of the sEMG signal:

- Muscle fiber orientation: the alignment of the electrode pair with the direction of muscle fibers maximizes recorded amplitude, while misalignment causes phase cancellation [106].

- Depth of active fibers: signals from deeper fibers are more attenuated by tissue filtering; therefore, sEMG primarily reflects activity of superficial motor units.
- Subcutaneous tissue thickness: fat and skin layers act as a low-pass filter, reducing amplitude and shifting the spectrum toward lower frequencies [106] *(Figure 2.11)*.
- Muscle fiber conduction velocity: physiological factors such as temperature, fatigue, or fiber type alter conduction velocity, thereby influencing MUAP duration and frequency content [96].
- Physiological variability: differences in fiber composition, motor-unit territory, and muscle architecture contribute to inter-individual variability.

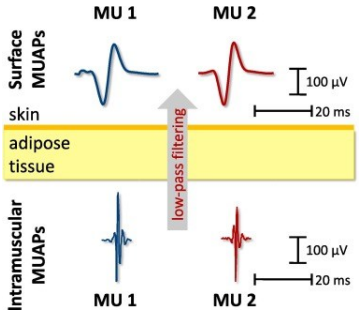

Figure 2.11 Propagation of MUAPs: from generation to the surface [107]

2.2.2.3 Technical and experimental sources of variability

Besides physiological influences, technical aspects of acquisition can markedly affect sEMG quality:

- Electrode configuration: electrode size and inter-electrode distance determine the spatial filtering properties of the system. Larger spacing increases amplitude but also the likelihood of crosstalk from adjacent muscles [106].
- Electrode placement: small deviations in position relative to the innervation zone or tendon can alter signal amplitude and phase [98].
- Skin preparation: poor electrode-skin contact or high impedance can increase noise and reduce reproducibility.
- Motion artefacts: mechanical disturbances due to cable movement or skin deformation introduce low-frequency noise, particularly in dynamic tasks.
- Power-line interference: 50 Hz contamination from power grid is a typical problem and typically removed using notch or band-stop filters.

These factors highlighted the need for standardized electrode placement and acquisition procedures, which led to the definition of the SENIAM guidelines [98].

Adherence to such protocols reduces variability across sessions and subjects, ensuring that differences in EMG amplitude or frequency content reflect physiological changes rather than inconsistencies in recording setup.

2.2.3 Signal acquisition and instrumentation

Reliable acquisition of surface electromyography signals requires an appropriate combination of sensor technology, placement accuracy, and hardware characteristics.

Since the EMG potential measured at the skin surface is extremely small, typically in the order of microvolts, careful attention to instrumentation and experimental setup is essential to ensure high signal quality and reproducibility [97][105].

2.2.3.1 Electrodes and detection configuration

sEMG is typically recorded using Ag/AgCl electrodes with conductive gel or pre-gelled adhesive pads, thanks to their stable electrochemical properties and low half-cell potential. Reusable dry electrodes and textile-based sensors have also become increasingly popular in wearable applications, although they often exhibit higher impedance and lower signal-to-noise ratio [96].

Electromyographic signals can be recorded using either monopolar or bipolar configurations. In monopolar recordings, each electrode measures the potential difference between an active site placed over the muscle belly and a reference electrode positioned on an electrically neutral location, typically over a bony prominence. This configuration captures the global activity of the muscle but is more susceptible to external noise and crosstalk from adjacent muscles [99].

In contrast, electrodes are almost always arranged in a differential (bipolar) configuration, where two closely spaced electrodes measure the potential difference across the muscle surface. This setup minimizes common-mode noise and enhances spatial selectivity. The inter-electrode distance typically ranges from 10 to 20 mm: smaller distances increase selectivity but reduce amplitude, while larger distances capture broader muscle activity and raise the risk of crosstalk from adjacent muscles [106].

Electrodes should be aligned parallel to muscle fiber direction to maximize detected amplitude and avoid phase cancellation. Correct orientation is particularly important for fusiform and pennate muscles, where fiber orientation may vary along the muscle length [98].

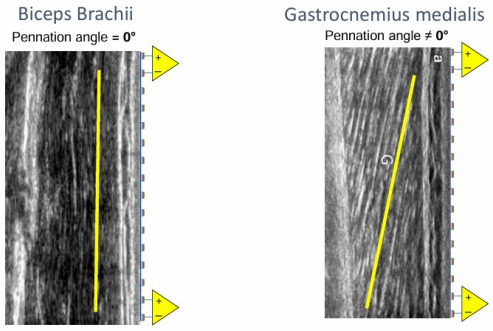

Figure 2.12 Different muscle fibers orientation in fusiform muscle (left) and pennate muscle (right) [100]

2.2.3.2 Skin preparation and placement guidelines

Because the skin acts as a high-impedance layer between the muscle and electrodes, proper skin preparation is crucial. The recommended procedure involves cleansing the skin with alcohol to remove oils and debris, and, if necessary, light abrasion to reduce impedance and improve contact stability [98].

Electrodes should be placed on the midline of the muscle belly, halfway between the innervation zone and the tendon, avoiding areas near muscle edges where signal amplitude decreases and crosstalk increases [96].

Standardized electrode positioning greatly enhances inter-subject comparability and repeatability; the SENIAM project provides detailed recommendations for each major muscle group, including lower limb muscles [98].

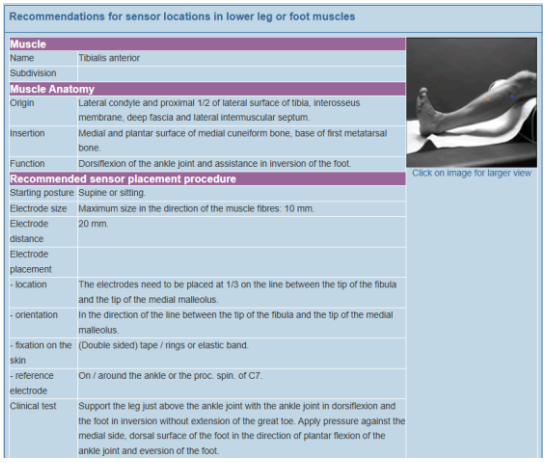

Recommendations for sensor locations in lower leg or foot muscles

Muscle	
Name	Tibialis anterior
Subdivision	
Muscle Anatomy	
Origin	Lateral condyle and proximal 1/2 of lateral surface of tibia, interosseus membrane, deep fascia and lateral intermuscular septum.
Insertion	Medial and plantar surface of medial cuneiform bone, base of first metatarsal bone.
Function	Dorsiflexion of the ankle joint and assistance in inversion of the foot.
Recommended sensor placement procedure	
Starting posture	Supine or sitting.
Electrode size	Maximum size in the direction of the muscle fibres: 10 mm.
Electrode distance	20 mm.
Electrode placement	
- location	The electrodes need to be placed at 1/3 on the line between the tip of the fibula and the tip of the medial malleolus.
- orientation	In the direction of the line between the tip of the fibula and the tip of the medial malleolus.
- fixation on the skin	(Double sided) tape / rings or elastic band.
- reference electrode	On / around the ankle or the proc. spin. of C7.
Clinical test	Support the leg just above the ankle joint with the ankle joint in dorsiflexion and the foot in inversion without extension of the great toe. Apply pressure against the medial side, dorsal surface of the foot in the direction of plantar flexion of the ankle joint and eversion of the foot.

Click on image for larger view

Figure 2.13 Example of SENIAM electrode positioning guidelines [44].

2.2.3.3 Amplification and acquisition hardware

Due to the limited magnitude of sEMG signals, the recording system must include low-noise differential amplifiers with high input impedance (≥ 100 MΩ) and high common-mode rejection ratio (CMRR), ideally above 100 dB, to suppress powerline interference and motion artifacts [105].

Typical amplifier bandwidth ranges from 10-20 Hz (high-pass) to 450-500 Hz (low-pass), matching the physiological spectrum of the EMG while excluding low-frequency drift and high-frequency noise [97][99].

Signals are then digitized using analog-to-digital converters with at least 12-bit resolution (often 16-bit in modern systems) and a sampling rate no lower than 1000 Hz, to prevent aliasing and to preserve temporal details of the waveform [96].

Wireless EMG systems are now widely used in gait and rehabilitation research, since they reduce motion artifacts and interference caused by cables and improve subject comfort without significantly compromising signal integrity.

2.2.4 Preprocessing of sEMG signals

Before quantitative analysis or feature extraction, raw sEMG data must undergo a series of preprocessing steps designed to remove noise, standardize amplitude, and highlight the physiologically meaningful components of the signal [96][99].

2.2.4.1 Filtering and artifact removal

The raw sEMG signal contains various noise sources, including movement artifacts (< 20 Hz), power-line interference (50 Hz), and high-frequency electronic noise (> 500 Hz). To attenuate these components, filtering is a fundamental preprocessing step.

A band-pass filter is typically applied, with cut-off frequencies between 20 and 450-500 Hz, which preserves the physiological spectrum of the EMG signal while removing drift and high-frequency disturbances [105].

In environments with strong electromagnetic contamination, a notch filter centered at 50 Hz can further reduce power line interference. However, excessive filtering should be avoided, as it may distort signal morphology and attenuate relevant physiological information.

Advanced approaches, such as adaptive filtering and wavelet-based denoising, have been proposed for dynamic tasks, where movement artifacts may overlap in frequency with the true EMG content [108].

2.2.5 Rectification and envelope extraction

Because the EMG signal alternates in polarity and oscillates around zero, rectification is commonly used to convert all values to positive polarity, emphasizing the overall level of activity. Full-wave rectification is the standard approach, as it preserves the total energy of the signal [99].

To obtain a smoother representation of muscle activation over time, a linear envelope can be extracted by applying a low-pass filter (typically 2-10 Hz) to the rectified signal, or, alternatively, the root mean square (RMS) can be computed over a sliding window to quantify the time-varying amplitude of EMG activity [96].

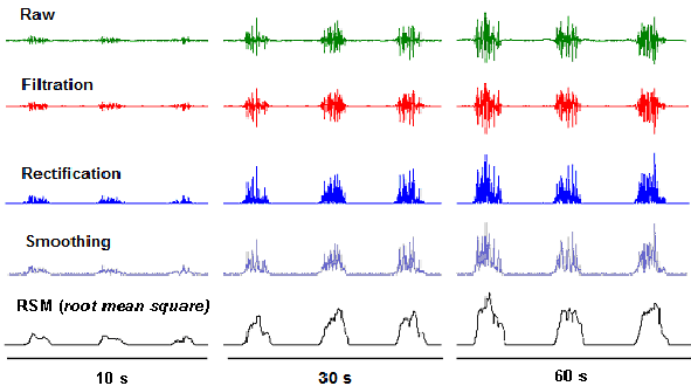

Figure 2.14 Typical sEMG signal processing pipeline [109]

2.2.6 Feature extraction and analysis

Once EMG signals have been properly preprocessed, the next step involves extracting quantitative descriptors, or features, that summarize specific properties of the waveform. These features allow the complex, stochastic EMG signal to be represented numerically and compared across muscles, subjects, or conditions.

Feature extraction can be performed in several domains: time, frequency, or time-frequency, depending on the analytical goals. Each domain captures distinct aspects of muscle activity, from intensity and variability to fatigue and coordination [96][110].

2.2.6.1 Time domain features

TD features are directly computed from the preprocessed sEMG signal or from the extracted envelope without frequency transformation. They are computationally simple and widely used for real-time analysis or pattern recognition. Most of them reflect the amplitude and variability of muscle activation and correlate with the level of neural drive to the muscle.

Common TD features include:

- Mean Absolute Value (MAV): the average rectified amplitude over a window; correlates with muscle contraction intensity.
- RMS: the square root of the mean squared value of the signal, proportional to the effective energy of the EMG and linearly related to force in isometric contractions [99].
- Integrated EMG (IEMG): the cumulative absolute value over time, often used to quantify total activation in a movement phase.
- Zero Crossing (ZC): number of times the signal crosses zero; provides an indirect measure of frequency content.
- Slope Sign Changes (SSC) and Waveform Length (WL): reflect the signal's complexity and rate of change, informative for distinguishing between movement phases or levels of effort [111].
- VAR or Standard Deviation (STD): describe signal dispersion, often related to activation variability.

These parameters are particularly effective for muscle activation quantification, onset detection, and classification of movement patterns, and remain the foundation of many EMG-based control systems [110][111].

2.2.6.2 Frequency domain features

Frequency-domain (FD) analysis provides complementary information on the spectral composition of the EMG signal, which is influenced by muscle fiber conduction velocity, motor-unit synchronization, and fatigue [97][105].

Applying the Fast Fourier Transform to the signal, it is possible to compute the power spectral density (PSD), from which several key descriptors can be extracted:

- Mean Frequency (MNF): the average frequency weighted by spectral power.
- Median Frequency: the frequency that divides the power spectrum into two equal halves; commonly used as a fatigue indicator.
- Peak Frequency (PKF): the frequency of maximum spectral amplitude.
- Spectral Moments: higher-order moments that quantify the spread and asymmetry of the spectrum.

These frequency-domain features are widely employed to assess neuromuscular fatigue during prolonged or repetitive tasks, since the power spectrum typically shifts toward lower frequencies, due to decreased conduction velocity and motor-unit synchronization changes [112].

2.2.6.3 Time-frequency features

Because muscle activation is inherently non-stationary, time-frequency (TF) methods provide a more detailed description of how spectral content evolves over time. Common approaches include:

- Short-Time Fourier Transform (STFT): computes spectra within short, overlapping windows, producing a TF map of EMG activity.
- Wavelet Transform: decomposes the signal into localized waveforms at multiple scales, capturing transient events and subtle temporal changes more effectively than STFT [113].

TF features are potentially useful in dynamic tasks such as gait, where the frequency content of EMG changes within the cycle.

2.2.6.4 Complexity features

Beyond TF features, several nonlinear and complexity-based measures have been proposed to capture the irregularity and unpredictability of the EMG waveform, such as Sample Entropy (SpEn) and Shannon Entropy (SE), which quantify the degree of signal regularity or self-similarity and can be sensitive to motor control strategies or fatigue [114].

2.2.6.4.1 Shannon Entropy

SE measures the average information content or uncertainty associated with a discrete probability distribution [115]. In the context of physiological signals, it quantifies how evenly distributed the amplitude or symbolic patterns are across the observation space.

Given a discrete signal with probability distribution $p(x_i)$ over n states, SE is defined as:

$$SE = \sum_{i=1}^{n} p[x_i] \cdot log_2\left(\frac{1}{p[x_i]}\right)$$

Equation 2.4 Shannon Entropy

where $p(x_i)$ is the probability of observing the i-th amplitude bin.

2.2.6.4.2 Sample Entropy

SpEn is a non-linear measure used to quantify the irregularity and unpredictability of physiological time-series data.

Given a signal X of length N, it evaluates the likelihood that two sequences of length d that are similar within a tolerance r will remain similar when extended to length $d + 1$. Lower values indicate a more regular or predictable signal, whereas higher values reflect greater complexity.

$$SpEn(d, r, N) = -ln\left[\frac{\sum_i C_i^{d+1}(r)}{\sum_i C_i^{d}(r)}\right]$$

Equation 2.5 Sample Entropy

Where:

$$C_i^d(r) = \frac{1}{(N-d+1)} N_i^r \qquad i = 1,2,\dots,N-d+1$$

And:

- N is the signal length
- d is the segment length
- r is the tolerance
- N_i^r computes the number of times that the distances between vectors *X(1:d)* and *X(i:d+i)* (the maximum distance between pairs of elements) are smaller than *r*

2.2.6.5 Correlation-based features

While most EMG features are computed from individual channels, correlation-based features describe the relationships between signals recorded from different muscles or between different time windows of the same signal.

These measures provide insight into muscle coordination, co-activation patterns, and functional coupling between synergistic or antagonistic muscle groups [116][117].

2.2.6.5.1 Coherence

Coherence, defined in the FD, provides information on the linear coupling between two signals at specific frequencies. It is defined as:

$$C_{xy}(f) = \frac{\left|S_{xy}(f)\right|^2}{S_{xx}(f) \cdot S_{yy}(f)}$$

Equation 2.6 Coherence

Where $S_{xy}(f)$ is the cross-power spectral density between $x(t)$ and $y(t)$.

Coherence values range from 0 (no linear relationship) to 1 (perfect correlation) and can reveal frequency bands where muscles share common neural input [97][118].

In the context of gait or posture control, coherence analysis helps identify functional muscle synergies and intermuscular coordination patterns, especially in frequency ranges associated with cortical drive (typically 10–60 Hz) [117].

2.2.6.5.2 Autocorrelation and self-similarity

When correlation analysis is applied within a single EMG channel, the autocorrelation function $R_{xx}(\tau)$ describes how similar a signal is to a delayed version of itself.

$$R_{xx}(\tau) = \int_{-\infty}^{+\infty} x(t) \cdot x(t-\tau) dt$$

Equation 2.7 Autocorrelation function

Features such as the autocorrelation coefficient at given lags or the width of the main peak can reflect motor-unit firing regularity, burst periodicity, or rhythmic modulation in gait-related tasks [96].

2.2.6.5.3 Mutual Information

A more general measure of dependency between two signals is Mutual Information (MI), derived from information theory.

Unlike correlation or coherence, MI detects any form of statistical dependence, whether linear or nonlinear [119][120].

For two random variables $X$and Y, the mutual information is defined as:

$$MI(X;Y) = \iint p(x,y) \log\left(\frac{p(x,y)}{p(x)p(y)}\right) dx\, dy$$

Equation 2.8 Mutual Information

where $p(x,y)$ is the joint probability density function and $p(x)$, $p(y)$ are the marginals. $MI(X;Y)$ is always non-negative and equals zero only when X and Y are statistically independent.

In EMG studies, MI has been used to quantify functional connectivity between muscles, even when relationships are nonlinear or non-synchronous [121]. Higher MI values indicate greater shared information between signals, reflecting stronger neural coupling or co-activation.

This makes MI particularly suitable for investigating muscle synergies, bilateral coordination, and pathological alterations of intermuscular control in disorders such as Parkinson's disease or post-stroke gait [122].

2.2.7 Applications of sEMG in research

Surface electromyography has become a cornerstone tool in human movement research, offering a non-invasive means of observing the translation of neural commands into muscle activity.

Because of its versatility, sEMG has found applications across a wide range of disciplines, from biomechanics and rehabilitation to sports science and human-machine interaction, providing both qualitative and quantitative insight into the functioning of the neuromuscular system [94][96].

2.2.7.1 Gait and locomotion analysis

One of the most established fields of application for sEMG is gait analysis, where it provides detailed information about muscle activation timing, amplitude, and coordination during walking.

By recording from lower-limb muscles, such as the tibialis anterior (TA), gastrocnemius (GC), rectus femoris (RFem), biceps femoris (BF), and gluteus maximus (GM), researchers can characterize the sequence and duration of muscle activity throughout the gait cycle [123].

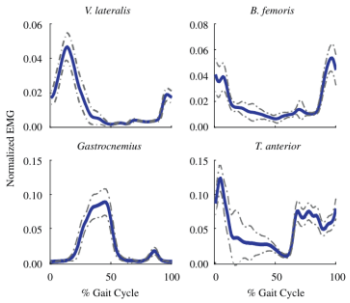

Figure 2.15 Lower limb muscle activation normalized with respect to % of gait cycle [124]

Temporal parameters such as onset and offset timing, burst duration, and co-activation indices reveal the strategies used by the nervous system to maintain stability and propulsion. For example, altered activation timing of the TA or excessive co-contraction between lower limb antagonist muscles has been reported in gait disorders such as Parkinson's disease, stroke, and cerebral palsy [125][126].

More recently, advanced analyses such as muscle synergy extraction and connectivity mapping have been applied to EMG data to study modular organization and intermuscular coordination during locomotion [117][127][128].

2.2.7.2 Rehabilitation and clinical assessment

In clinical and rehabilitative settings, sEMG is widely used to evaluate motor impairments and monitor recovery after neurological or musculoskeletal injury.

By quantifying muscle activation patterns, clinicians can detect abnormal synergies, co-contraction, or spasticity, and assess the effectiveness of therapeutic interventions [128].

Biofeedback applications allow patients to visualize their own muscle activity in real time, promoting motor relearning and voluntary control after stroke or spinal cord injury. In gait rehabilitation, sEMG-driven feedback, and robotic devices (such as exoskeletons) use EMG signals to trigger or modulate assistance in proportion to voluntary effort [129].

The same principle underlies EMG-triggered functional electrical stimulation (FES), where muscle activity recorded from a weak or contralateral limb can be used to activate electrical stimulation in the affected muscles, facilitating symmetrical movement patterns [130].

2.2.7.3 Advanced research directions

Modern EMG research increasingly relies on high-density surface EMG (HD-sEMG), which employs electrode arrays to capture spatial distributions of muscle activation with high resolution. This technique enables decomposition into single motor-unit action potentials, estimation of conduction velocity maps, and detailed analysis of muscle architecture [131]. Such approaches deepen understanding of neuromuscular control and are being translated to clinical and robotic contexts.

At the same time, network-based analyses of intermuscular coherence and information-theoretic measures (e.g., MI) are providing new insights into the connectivity structure of muscle coordination networks [117][122].

These frameworks mark the transition from viewing EMG as a set of isolated signals to considering it as a system-level representation of neural control of movement.

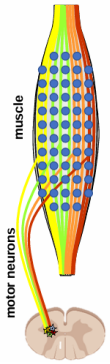

Figure 2.16 HD-sEMG [100]

2.3 Inertial Measurement Units (IMUs)

Inertial Measurement Units (IMUs) are compact multisensory systems designed to measure linear acceleration and angular velocity, and, when equipped with magnetometers, the orientation of a body segment with respect to the Earth's magnetic field.

Widely used in biomechanics, rehabilitation, and neuroscience to analyze gait, posture, and motor control, they provide a portable and versatile tool for quantifying human movement in real-world environments, offering an alternative to optical motion capture systems that are often costly, cumbersome, and restricted to laboratory settings [132][133].

By combining accelerometers, gyroscopes, and magnetometers, they allow estimation of kinematic parameters such as displacement, velocity, and orientation, as well as the detection of movement events and phases.

2.3.1 Physical principles and signal components

2.3.1.1 Structure and components of an IMU

An IMU typically consists of three sensing elements:

1. a triaxial accelerometer
2. a triaxial gyroscope
3. a triaxial magnetometer

Together, these sensors measure linear acceleration, angular velocity, and magnetic field strength along three orthogonal axes, providing a nine-degree-of-freedom (9-DOF) representation of motion [132][134].

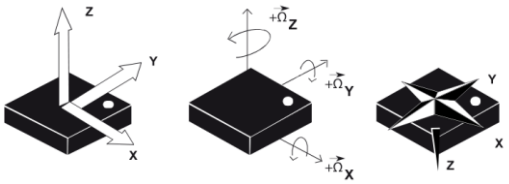

Figure 2.17 9-DOF IMU schematic representation [135]

Simpler configurations, such as 6-DOF systems, include only accelerometers and gyroscopes and are usually less accurate in the orientation estimation.

2.3.1.2 Accelerometer

The accelerometer measures specific force, corresponding to the linear acceleration acting on the sensor, and converts it in acceleration, expressed either in meters per second squared (m/s^2) or in multiples of gravitational acceleration ($g = 9.81\ m/s^2$).

Most IMUs employ Micro-Electro-Mechanical Systems (MEMS) accelerometers, where a microscopic proof mass suspended by elastic elements is displaced by inertial forces, and this deflection is converted into an electrical signal [136].

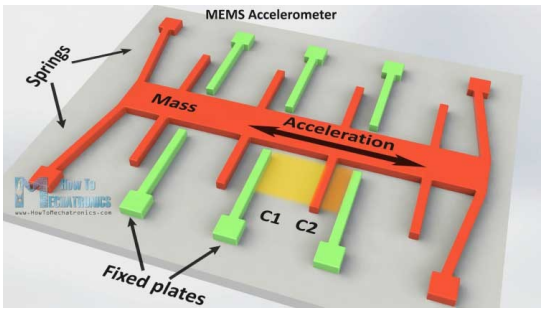

Figure 2.18 Mems Accelerometer [137]

In movement analysis, accelerometers capture translational motion and can be used to study the magnitude and timing of impacts or transitions between movement phases.

Because gravity is always present in the signal, separating dynamic acceleration (due to motion) from static acceleration (due to gravity) is a key step in signal interpretation [134].

2.3.1.3 Gyroscope

The gyroscope measures angular velocity, typically expressed in degrees per second (°/s) or radians per second (rad/s), indicating how fast the sensor rotates around each of its three axes.

MEMS gyroscopes operate based on the Coriolis effect, in which a vibrating mass experiences an apparent force proportional to the angular velocity of the sensor.

Integrating the angular velocity over time provides information about changes in orientation, although this process is subject to drift, as small measurement biases accumulate progressively [136][138].

Despite this limitation, gyroscopes are crucial for capturing rotational dynamics and for detecting events characterized by changes in angular motion, such as turns or limb swings [139].

2.3.1.4 Magnetometer

The magnetometer measures the local magnetic field vector, providing an absolute reference for orientation relative to the Earth's magnetic north.

It is primarily used to correct yaw drift from the gyroscope, thus improving the long-term stability of orientation estimates.

However, magnetometers are sensitive to local magnetic disturbances generated by metallic structures or electronic devices, which can distort the measurement. For this reason, their contribution is often adaptively weighted or excluded in environments with strong electromagnetic interference [140].

2.3.2 Orientation estimation and sensor fusion

While each component of an IMU provides valuable information about motion, none of them alone is sufficient to estimate orientation accurately.

- The accelerometer senses the direction of gravity and thus provides an estimate of inclination but cannot measure rotation about the vertical axis (yaw).

- The gyroscope measures angular velocity and can capture fast rotational dynamics, yet integration of its signal over time leads to drift, resulting in progressively inaccurate orientation estimates.
- The magnetometer provides an absolute reference for heading relative to the Earth's magnetic north but is sensitive to local magnetic disturbances.

To overcome these limitations, sensor fusion algorithms combine the three signals to produce a stable and drift-free estimate of orientation over time [134][138].

This process is essential in human movement analysis, where accurate knowledge of limb orientation enables quantification of joint angles, segment trajectories, and gait phases.

2.3.2.1 Mathematical representations of orientation

Orientation in three-dimensional space can be expressed using different mathematical formalisms:

- Euler angles (roll, pitch, yaw): intuitive representation, but prone to gimbal lock when two rotation axes align.
- Rotation matrices: 3×3 orthogonal matrices describing orientation transformations between reference frames.
- Quaternions: four-element vectors that provide a compact, singularity-free representation of orientation and are computationally efficient for continuous updates [134].

Most modern IMU systems internally represent orientation as unit quaternions and convert them to Euler angles or rotation matrices as needed for analysis.

2.3.2.2 Principles of sensor fusion

Sensor fusion algorithms' general goal is to minimize the estimation error between the predicted orientation (from integrated gyroscope data) and the measured orientation (from accelerometer and magnetometer readings). Several approaches have been proposed, differing in complexity, computational cost, and robustness.

2.3.2.2.1 Complementary and Kalman filters

Complementary filters implement a simple frequency-based combination of signals: low-pass filtering of accelerometer/magnetometer data (stable but slow) and high-pass filtering of gyroscope data (fast but drifting). This provides an effective balance for real-time applications with limited processing requirements [141].

In contrast, Kalman filters and their nonlinear extensions (Extended or Unscented Kalman Filters) use probabilistic models to optimally estimate the state (orientation) given noisy sensor measurements. They recursively update orientation estimates by weighing the predicted motion model (from the gyroscope) against sensor observations (from accelerometer and magnetometer), minimizing the overall estimation error [142].

Kalman-based approaches remain the standard in high-accuracy motion tracking and biomechanical applications [143].

2.3.2.2.2 Gradient-descent and quaternion-based filters

More recently, computationally efficient algorithms such as the Madgwick and Mahony filters have been developed for wearable and embedded systems [138][141].

These filters operate directly on quaternion representations and use gradient-descent optimization to minimize the difference between estimated and measured acceleration and magnetic field. They achieve high accuracy with minimal computational load, making them particularly suitable for real-time applications and battery-powered IMUs.

These algorithms are widely adopted in modern commercial systems, where the fusion process is implemented internally, and the user directly receives orientation estimates (quaternions, Euler angles, or rotation matrices) rather than raw sensor data.

2.3.2.3 Orientation estimation in research-grade IMUs

Research-oriented IMUs, such as those produced by APDM (Opal sensors), integrate proprietary fusion algorithms similar to the Madgwick or Kalman filter frameworks.

The sensors output pre-processed orientation data with high temporal precision and minimal drift, typically expressed as quaternions synchronized across multiple sensors [144][145].

This built-in estimation considerably reduces preprocessing requirements, allowing researchers to focus on higher-level analyses such as phase detection, feature extraction, and kinematic reconstruction.

2.3.2.4 Coordinate systems and reference frames

Accurate interpretation of IMU data requires awareness of the reference frames involved:

- The sensor frame is fixed to the IMU's axes (x, y, z).
- The global frame (or world frame) defines an external reference, typically aligned with gravity (z-axis vertical) and magnetic north.
- The body segment frame is defined anatomically for biomechanical interpretation.

Sensor fusion provides the transformation from the sensor frame to the global frame, enabling subsequent derivation of joint angles, segment orientations, and event-based parameters [134][143].

2.3.3 Acquisition and instrumentation

2.3.3.1 General considerations on IMU acquisition

Accurate acquisition of inertial data requires careful consideration of sensor configuration, placement, sampling parameters, and synchronization.

In research applications, IMUs are typically sampled at frequencies between 100 and 200 Hz, which is sufficient to capture human movement dynamics while minimizing data size and power consumption [132][133].

The range and resolution of the sensing elements determine the quality and interpretability of the signals. Typical full-scale ranges are ±16 g for accelerometers and ±2000°/s for gyroscopes, ensuring accurate tracking of both low- and high-intensity movements.

2.3.3.2 Sensor placement and body configuration

The placement of IMUs on the body critically affects the quality and interpretability of kinematic data. Sensors are generally aligned with the anatomical axes of the body segment they are attached to, enabling direct biomechanical interpretation of recorded motion.

Common attachment sites for gait analysis include the feet, shanks, thighs, pelvis, and trunk, depending on the variables of interest [132][139]. To ensure stability and reduce motion artifacts, sensors are fixed using elastic straps or medical-grade adhesive.

Prior to acquisition, an alignment or calibration procedure is typically performed to relate the sensor's coordinate frame to the global and anatomical frames. This calibration may involve a brief static posture (to identify the gravity vector) and a dynamic movement to define the segment's primary axis [134].

2.3.4 Signal preprocessing

2.3.4.1 Overview

Raw inertial data acquired from IMUs contain valuable kinematic information but also various sources of noise and bias that must be corrected before analysis.

Preprocessing transforms the raw accelerometer, gyroscope, and magnetometer signals into a consistent, reliable form suitable for event detection, phase segmentation, and feature extraction. Typical operations include filtering, bias removal, coordinate transformation and segmentation [132][134].

2.3.4.2 Filtering and noise reduction

All inertial sensors are affected by high-frequency noise and small mechanical vibrations that can obscure movement-related components.

To mitigate this, signals are typically passed through low-pass Butterworth filters with cutoff frequencies between 5 and 20 Hz, depending on the task dynamics [133][139]. For example, gait analysis often employs a cutoff near 10 Hz, which preserves the relevant motion content while suppressing noise.

2.3.4.3 Drift correction and bias compensation

Among IMU sensors, gyroscopes are most susceptible to bias drift. Even small constant offsets in angular velocity can integrate into substantial orientation errors over time. Common correction strategies include:

- High-pass filtering
- Static calibration, where the average gyroscope output in a motionless state is subtracted as a baseline.
- Zero-velocity updates, which reset velocity estimates during detected stance phases (e.g., when the foot is flat on the ground).
- Sensor fusion, which continuously corrects gyroscope drift using accelerometer and magnetometer information [134][143].

2.3.4.4 Coordinate alignment and reference frames

To interpret inertial data in biomechanical terms, the signals must be expressed in a common reference frame, rather than the sensor frame, whose axes depend on how the device is mounted.

Through orientation estimation, signals can be transformed into the global or anatomical frame, aligning them with gravity and the body's main axes of motion [134][140].

When multiple sensors are used, ensuring consistent alignment between their local frames prevents systematic asymmetries in derived kinematic variables.

After the alignment, gravity is often removed from the acceleration data, since it can bias the estimation of dynamic movement components and obscure the true kinematic patterns related to voluntary motion. By subtracting the gravitational acceleration vector, the resulting signal better reflects linear accelerations associated with limb or body movement rather than static posture or sensor orientation [134].

2.3.4.5 Segmentation and event detection

Once the IMU signals have been filtered and aligned, they are often segmented into meaningful movement phases or cycles.

Segmentation allows subsequent feature extraction to focus on homogeneous activity windows, such as single steps, turns, or task-specific periods.

Event detection methods depend on sensor placement and measured variable:

- Angular velocity zero-crossings or peaks can identify gait events such as heel strike and toe-off [139].
- Acceleration magnitude thresholds are used to detect impacts or postural transitions.
- Orientation changes can define turning periods or segment movements in upper-limb tasks.

Automatic segmentation enhances reproducibility and enables large-scale analysis of periodic behaviors such as locomotion or repetitive gestures.

2.3.5 Event and phase detection in gait analysis

2.3.5.1 General principles

Event and phase detection represent a central step in IMU based gait analysis. By identifying key temporal landmarks such as heel strike (HS), toe-off (TO), or turn initiation, it becomes possible to divide continuous motion into meaningful functional segments, allowing subsequent computation of gait parameters, spatiotemporal metrics, and movement features [139][146].

Inertial signals are particularly suited for this purpose because angular velocity and linear acceleration waveforms exhibit consistent cyclic patterns across steps.

Detecting these patterns enables the definition of gait phases such as stance, swing, or turning, which are essential for analyzing motor control and for detecting pathological deviations in locomotion [144][147].

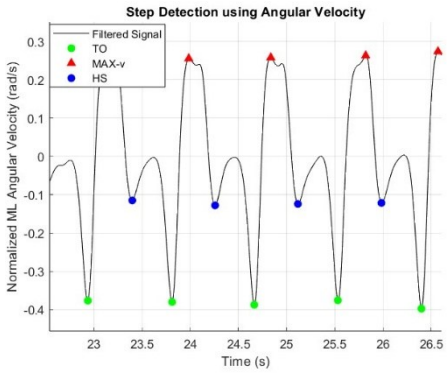

Figure 2.19 Angular Velocity cyclical pattern during physiological gait

2.3.5.2 Gait event detection (step and phase identification)

The detection of gait events is most commonly performed using foot- or shank-mounted IMUs, as these positions capture clear oscillatory patterns corresponding to each step. Several methods have been proposed:

- Threshold-based approaches, which identify events using zero-crossings or peaks in angular velocity or acceleration signals *(Figure 2.19)* [139][148].
- Model-based approaches, where a biomechanical or state-space model represents the periodic motion of the limb [149].
- Machine-learning-based methods, which classify temporal windows as specific gait events using supervised algorithms trained on annotated datasets [150].

A recent and widely cited example is the work of Renggli et al. (2020) [151], who proposed a robust and modular algorithm for step detection in free-living conditions using foot-mounted inertial sensors.

Their method combines angular velocity thresholds and dynamic pattern recognition, showing high accuracy in both healthy and clinical populations. This approach has become a reference for reliable, real-world step detection and is compatible with different sensor systems and walking speeds.

2.3.5.3 Gait phase classification

Once gait events are detected, the signal can be segmented into phases corresponding to functional portions of the gait cycle.

The stance phase begins at HS and ends at TO, whereas the swing phase covers the period between TO and the subsequent HS. More advanced models subdivide stance into loading response, mid-stance, and push-off sub-phases to capture finer details of locomotor control [123].

Inertial data from multiple segments (e.g., foot, shank, trunk) can be combined to assess inter-segmental coordination, allowing estimation of stride duration, cadence, symmetry indices, and gait variability [147][152].

Such segmentation provides the temporal structure required for computing phase-specific features in both research and clinical contexts.

2.3.5.4 Turning detection and characterization

Beyond linear gait, turning is an essential component of everyday mobility and a particularly sensitive marker of motor dysfunction [42][153].

Turn detection typically relies on trunk or pelvis angular velocity around the vertical axis, where rotations exhibit distinctive peaks corresponding to the onset and offset of turning maneuvers.

Some proposed algorithms can identify turns by applying thresholds on yaw angular velocity, by segmenting periods exceeding a minimal rotation angle (e.g., >45°), or by analyzing orientation changes derived from quaternion data [153].

Other studies have extended turn detection by integrating additional context, such as foot kinematics or multi-sensor synchronization, to improve accuracy in complex or free-living conditions [139][154]. These methods enable precise temporal localization of transitions between linear walking and rotational movement, critical information for advanced gait classification and for the identification of mobility impairments.

2.3.6 Feature extraction from IMU signals

Once inertial data have been preprocessed and segmented into meaningful movement phases, a set of quantitative features can be extracted to characterize the kinematics of gait and turning. These features can be divided into two categories:

1) Spatiotemporal gait features, which describe the geometric and temporal structure of walking cycles.
2) Signal-based features, derived directly from the raw accelerometer and gyroscope time series.

Both types of features are fundamental in clinical gait analysis, rehabilitation research, and data-driven classification models [152][154].

2.3.6.1 Spatiotemporal gait features

Spatiotemporal parameters provide a quantitative and easily interpretable description kinematic organization of gait. They are derived from the temporal sequence of detected gait events and from orientation or acceleration changes within a single step window [123][147].

2.3.6.1.1 Temporal parameters

Typical temporal parameters are:

- Stride time (T_s): interval between two consecutive heel strikes of the same foot.
- Step time (T_{step}): time between heel strikes of opposite feet.
- Stance and swing duration: relative portions of the gait cycle spent in contact with or off the ground.
- Cadence: number of steps per minute, reflecting walking rhythm and tempo.
- Double support time: duration during which both feet are in contact with the ground, often increased in unstable gait [152].

2.3.6.1.2 Spatial parameters

When orientation or acceleration data are double-integrated (or combined with step frequency), spatial quantities can be derived, such as:

- stride length (L_s).
- walking speed (v) [139][146].
- Turn angle (θ): total angular displacement during turning events [153].
- Variability and symmetry

Also, measures of stride-to-stride variability and bilateral symmetry are particularly relevant in clinical contexts, as they reflect gait stability and coordination [154]. Typical indices include:

- Coefficient of variation of T_s, L_s or v.
- Symmetry ratio between left and right T_s.
- Phase coordination index (PCI): quantifies temporal coupling between limbs [155].

2.3.6.2 Features derived from preprocessed inertial signals

In addition to discrete spatiotemporal metrics, features can be extracted directly from the continuous accelerometer and gyroscope signals. These features are typically computed over short, overlapping windows and can describe signal intensity, frequency content, regularity, or complexity [110].

2.3.6.2.1 Time-domain features

TD descriptors are simple yet informative measures of signal amplitude and variability:

- Mean, STD, and VAR: quantify central tendency and dispersion of acceleration or angular velocity.
- RMS: reflects signal energy and overall movement intensity.
- Signal magnitude area: sum of absolute values of the three acceleration components, representing total dynamic activity [156]
- Jerk (derivative of acceleration): assesses smoothness of motion, often linked to motor control efficiency.
- Range or peak-to-peak amplitude: identifies maximum oscillatory excursions per cycle.

2.3.6.2.2 Frequency-domain features

Spectral features describe rhythmic properties and periodicity of movement:

- PKF: the frequency with maximum power, corresponding to step or stride frequency.
- Spectral entropy: quantifies signal complexity; higher entropy reflects irregular or unstable motion.
- Power in frequency bands: proportion of total power within defined bands (e.g., 0.5–3 Hz for normal gait).

2.3.6.2.3 Nonlinear and statistical features

To capture the variability and regularity of inertial waveforms, nonlinear metrics have been increasingly adopted:

- SpEn and SE: evaluate signal predictability and regularity; lower values indicate more periodic motion.
- Skewness and kurtosis: describe signal asymmetry, useful for characterizing atypical or abrupt movements.

2.3.6.2.4 Correlation-based features

Inter-segment correlations provide information on coordination between body parts:

- Cross-correlation coefficients between left-right limbs or between trunk and lower limbs indicate synchronization and timing consistency [157].
- Autocorrelation coefficients reveal intra-signal periodicity, helpful for assessing rhythmic gait cycles [158].

3 Previous work in FoG detection

3.1 Technological approaches for the objective detection of Freezing of Gait

Over the past two decades, researchers and clinicians have devoted growing attention to the objective detection of FoG, since the ability to identify these episodes, both in laboratory and real-world settings, allows for more precise monitoring of disease progression, supports the evaluation of pharmacological and rehabilitative strategies, and provides the foundation for real-time closed-loop interventions, such as auditory or visual cueing systems designed to stop the freezing episode and restore walking [45][159].

A wide variety of technological approaches have been explored to capture the onset and dynamics of FoG, reflecting the evolution of the field:

- IMUs, typically placed on the lower limbs or trunk, have been the most widely used modality thanks to their ability to capture gait kinematics with high temporal resolution, combined with small size, low cost, and ease of integration into wearable devices [41].
- sEMG has been used to characterize muscle activation patterns during gait and freezing episodes, because it provides insight into the pathophysiological changes underlying FoG, and has been explored both as a standalone modality and in combination with IMUs [160].
- fNIRS, a more recent addition, offers a non-invasive window into cortical hemodynamic during locomotion. Studies suggest that altered activation of prefrontal and SMA may precede or accompany FoG episodes, highlighting the role of central mechanisms in addition to peripheral kinematics and muscle activity [161][162].

Beyond these single-modality approaches, multimodal systems aim to exploit complementary information from different sensors, combining kinematic, muscular, and cortical markers to improve robustness and generalizability. Such approaches are particularly attractive in the context of real-world monitoring, where variability in environment, task, and patient phenotype can challenge the reliability of single-sensor systems [163][164].

Taken together, these developments illustrate a progressive shift in methodology: from thresholding techniques applied to IMU signals, to classical ML models trained on handcrafted features, and more recently to deep learning (DL) architectures capable of end-to-end representation learning. This trajectory reflects the broader evolution of biomedical signal processing and sets the stage for ongoing efforts to build multimodal, ML-based systems for reliable FoG detection and prediction in both laboratory and daily life scenarios.

3.2 IMU-based approaches for FoG detection and prediction

IMUs have been at the core of FoG research since the beginning of the 2000s. Their widespread adoption stems from their ability to capture gait kinematics in a portable, inexpensive, and minimally invasive manner, which makes them suitable both for laboratory experiments and for long-term home monitoring [165].

3.2.1 Thresholding approaches.

A landmark contribution in this field was made by Moore et al. [41], who introduced the Freezing Index (FI), a quantitative metric derived from accelerometer signals collected at the lower limbs. The FI is defined as the ratio between the signal power in the "freeze band" (3-8 Hz), capturing the high-frequency trembling of the legs during freezing, and the "locomotor band" (0.5-3 Hz), reflecting normal step cadence. By applying a threshold to this index, it became possible to discriminate between normal walking and FoG episodes.

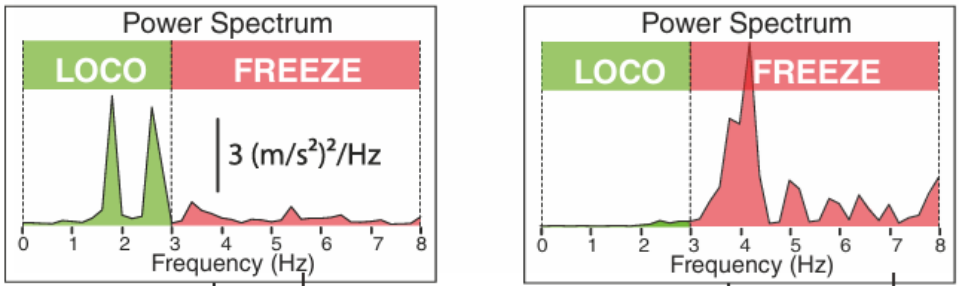

Figure 3.1 Power spectrum during normal walk (left) and FoG (right) [166]

Although highly influential, this approach also exposed a key limitation: thresholds often need to be calibrated for a specific patient cohort or dataset, limiting generalizability when applied across broader clinical populations or daily-life [41][159].

3.2.2 The transition to machine learning.

To overcome these limitations, subsequent research shifted towards supervised machine learning. Instead of relying on fixed thresholds, these methods extract features from IMU data (time-domain statistics, frequency-band powers, entropy measures, and step regularity) and train classifiers to automatically learn discriminative boundaries.

Early studies successfully applied support vector machine (SVM) [167], k-nearest neighbors (kNN), and Decision Trees (DTree) [168][169]. These models demonstrated higher adaptability than thresholding approaches, particularly in heterogeneous patient groups and under varying gait tasks.

3.2.2.1 Growing methodological sophistication.

With the release of annotated resources such as the Daphnet FoG dataset [159], the field saw the rise of more complex algorithms. Ensemble methods like Random Forest (RF) and Gradient Boosting Tree (GBT) were adopted to improve classification robustness, while evaluation protocols moved from strictly controlled laboratory paradigms to activities of daily living

(ADL) environments. These studies highlighted new challenges, such as distinguishing FoG from voluntary stops or irregular gait unrelated to freezing [165].

3.2.3 The emergence of deep learning.

More recently, DL architectures have been applied to IMU data, motivated by the ability to learn feature representations directly from raw signals without the need for feature extraction. One-dimensional convolutional neural networks (CNNs) and recurrent models have been explored for FoG detection and even short-term prediction [169][170].

Borzi et al. [171] proposed a real-time FoG detection system based on deep neural networks and a single inertial sensor, demonstrating that data-driven models can achieve high detection accuracy even with minimal hardware setups. Their work highlights how DL approaches can exploit subtle temporal patterns in gait dynamics, offering promising performance.

While these methods show promising improvements, their reliance on large, high-quality annotated datasets and substantial computational resources currently limits their adoption, as well as issues such as model interpretability and generalization to unseen patients. As such, DL remains an emerging trend in the field rather than a consolidated standard. [171]

3.3 EMG-based approaches for FoG detection and prediction

While IMUs capture the external kinematic consequences of gait, sEMG provides a complementary view by measuring the electrical potentials associated with muscle activation. This perspective is particularly relevant for FoG, as abnormal recruitment patterns and disrupted muscle synergies often precede or accompany freezing episodes. For instance, irregular activation of the TA and GC during the stance-to-swing transition has been reported as a hallmark of freezing [160].

3.3.1 Early explorations

Initial EMG studies in Parkinson's disease were largely descriptive, focusing on identifying abnormalities in muscle timing and co-contraction patterns during gait. Nieuwboer et al. [172] showed that FoG is characterized by prolonged bursts, reduced rhythmicity, and abnormal coupling between antagonistic muscles such as TA and GC. These findings provided the physiological basis for considering EMG as a valuable modality for FoG detection.

3.3.2 From descriptive analysis to quantitative features

As the field moved toward automatic detection, researchers began extracting quantitative descriptors from EMG, many of which align with those adopted in the present work.

These include time-domain indices such as energy, MAV, envelope STD, WL, ZC, and SSC, as well as frequency-domain metrics like MF and spectral ratios. In addition, measures of inter-muscular connectivity, such as coherence and MI, have been employed to capture altered coordination across antagonist muscle groups.

For example, Tahafchi et al. [173] used multimodal sensors combining EMG and IMUs to analyze lower-limb activity in people with PD. By computing energy and envelope-based descriptors of EMG activity, along with kinematic features, they trained an SVM classifier that successfully discriminated between standing, walking, and freezing episodes. Their results highlighted the discriminative power of EMG bursts and energy features, consistent with reports of altered TA and GC recruitment during FoG.

More recently, Zhang et al. [174] released a publicly available multimodal dataset including EMG recordings from TA and GC muscles. In their analysis, EMG features such as MAV, ZC, SSC, and WL were extracted, consistent with the set of descriptors commonly applied in FoG detection.

Feature	Representative studies	Notes
Energy / MAV	Tahafchi 2017; Zhang 2022; Cole 2010	Sensitive to burst amplitude; discriminates FoG vs normal gait
Envelope statistics (Mean, STD)	Tahafchi 2017	Captures changes in EMG activation
WL	Zhang 2022	Reflects EMG signal complexity; higher during irregular bursts
ZC	Zhang 2022	Detects frequency of sign changes; useful for transient FoG events
SSC	Zhang 2022	Highlights slope variability; sensitive to tremor-like FoG
Lag/Ratio of first peak	Cole 2010	Temporal descriptors linked to onset dynamics of EMG bursts
MI	Cantù 2019	Connectivity metric highlighting abnormal synergies between muscles

Figure 3.2 EMG Features for FoG Detection

3.3.3 Integration with IMUs and improved classification

Beyond standalone EMG, several works combined it with IMUs to improve detection accuracy. Mazzetta et al. [160] designed a wearable system integrating shank-mounted IMUs and single-channel EMG to detect FoG episodes in free living-like conditions.

Their approach introduced the R-index, a step-wise ratio between the maximum angular velocity measured by the gyroscope and the corresponding EMG envelope amplitude.

$$R = \frac{\max\left(|\omega_{\text{sagittal}}|\right)}{\text{sEMG}\,|_{t=t_{\max\left(\omega_{\text{sagittal}}\right)}}}$$

This index allowed robust discrimination between normal walking and FoG, with high accuracy and very few false detections, highlighting that EMG does not only complement kinematic data, but can provide direct, physiologically grounded markers of muscle activation deficits during freezing.

3.3.4 Toward prediction and real-world applicability.

More recently, Moore et al. [175] investigated wearable EMG garments designed for everyday use. They observed a marked decrease in EMG amplitude of quadriceps and hamstrings approximately 3-4 seconds before FoG onset, pointing to a potential predictive biomarker. This finding is particularly relevant for closed-loop interventions, where pre-FoG signatures could be used to trigger cueing systems before the freezing episode fully develops.

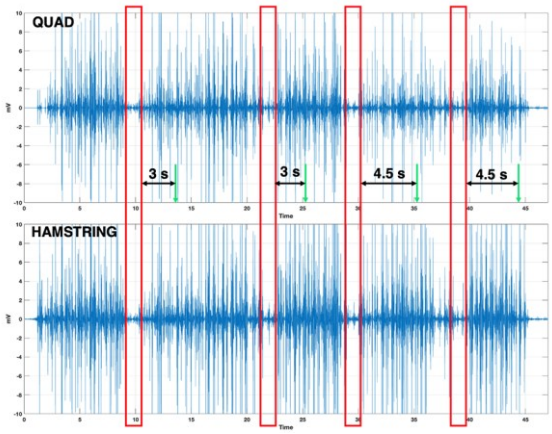

Figure 3.3 Amplitude decrease before FoG onset [175]

3.3.5 Challenges and practical limitations

Despite its promise, sEMG faces practical barriers compared to IMUs. Reliable signal acquisition requires careful electrode placement and skin preparation, while movement artifacts and long-term wearability remain critical issues. These constraints explain why EMG is often used as a complementary rather than standalone modality in FoG detection. However, ongoing developments in wearable technologies, such as textile-integrated electrodes [175], may reduce these limitations and facilitate long-term monitoring.

3.4 Machine learning for FoG detection and prediction

ML has become a cornerstone of modern biomedical signal analysis, providing tools capable of identifying complex, non-linear relationships within physiological data.

In the study of FoG, ML enables the automatic recognition of temporal and spectral patterns in sensor signals that may precede or characterize freezing episodes. By learning directly from examples rather than relying on predefined rules, ML models can adapt to heterogeneous patient populations, variable conditions, and different sensor configurations, offering a powerful framework for both detection and prediction of FoG.

Most FoG studies employing ML adopt a supervised learning paradigm, in which algorithms are trained on labelled data segments and then evaluated on unseen samples. The labelling is often binary (FoG vs non-FoG), although some studies introduced a third class, *Pre-FoG*, to build models capable of anticipating FoG onset and enabling closed-loop cueing systems [157][176].

A typical ML pipeline for FoG detection and prediction includes several fundamental stages:

3.4.1 Feature extraction

The first step involves transforming preprocessed sensor data into compact, informative representations. Features are extracted from IMU, EMG, or fNIRS signals in the TD, FD, and occasionally in the connectivity domain.

The goal is to highlight the statistical and physiological differences between normal gait, pre-FoG, and FoG periods, capturing both transient bursts and sustained oscillations.

3.4.2 Dataset Partitioning

An essential step in the development of any machine learning model is the proper partitioning of the dataset into separate subsets for training, validation, and testing. The choice of partitioning strategy depends strongly on the size and structure of the available data.

3.4.2.1 Train-Validation-Test split

When the dataset is sufficiently large and diverse, it is common to split it into independent subsets, typically using a fixed proportion such as 70-80% for construction and 20-30% for testing [177].

When model tuning is required (e.g., for hyperparameter optimization), construction set is often split in training set and validation set, ensuring that the final test set remains entirely unseen until the last evaluation stage. This approach is computationally efficient and provides a clear separation between learning, tuning, and testing phases.

However, in biomedical and neurophysiological research, such as FoG studies, datasets are often limited in size, and samples may be highly correlated across repetitions or subjects. In such conditions, a simple train-test split may yield unstable results or biased estimates of model performance.

3.4.2.2 Cross-validation

To address this, cross-validation (CV) procedures are typically employed to obtain more robust and generalizable estimates of predictive accuracy.

Cross-validation divides the data into k subsets (or "folds"), iteratively training the model on $k-1$ folds and testing it on the remaining one. This process is repeated k times so that each fold serves as a test set once, and the final performance metric is averaged across all iterations. Common choices include k-fold CV (often with $k = 5$ or 10) and stratified CV, which preserves class balance in each fold [178].

In FoG research, inter-subject variability is particularly high, and subject-specific patterns can dominate the model's learning process [28]. Therefore, validation across subjects is essential to ensure true generalization.

3.4.2.3 Leave-One-Subject-Out cross-validation

A widely adopted strategy is the Leave-One-Subject-Out (LOSO) cross-validation: the model is trained on data from all but one participant and tested on the remaining one, repeating this procedure iteratively for every subject.

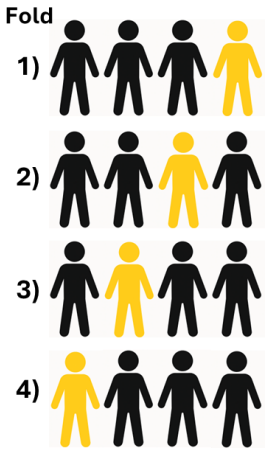

Figure 3.4 LOSO partition, in yellow the subject used for validation, in black the subject used for training

This approach yields a subject-independent estimate of performance, reflecting how well the model would generalize to unseen patients in a real-world clinical setting. Moreover, LOSO prevents data leakage, the inadvertent use of information from the same subject in both training and testing, which could otherwise lead to overly optimistic results.

Overall, careful dataset partitioning and rigorous cross-validation are fundamental to achieving reliable and generalizable models, particularly in biomedical contexts where data quantity and independence are often limited.

3.4.3 Feature selection

Once features are extracted, feature selection or dimensionality reduction is often applied to reduce redundancy, mitigate overfitting, and improve model interpretability. This step is particularly crucial in neuroimaging and multimodal frameworks, where the number of extracted features can be large relative to the number of observations.

Feature selection methods can be broadly categorized into filter-based, wrapper, and embedded approaches [179][180].

3.4.3.1 Filter based methods

Filter based methods evaluate the relevance of each feature independently of any specific classifier, relying on statistical or information-theoretic criteria, such as correlation, MI, or ranking metrics, to identify the subset of features that maximizes discriminative power while minimizing redundancy.

3.4.3.1.1 Minimum Redundancy Maximum Relevance (mRMR)

mRMR is a feature selection criterion designed to identify a subset of features that provides the highest amount of information about the target variable while avoiding redundancy among features [181].

Let S denote the subset of selected features and c the class label. The relevance of a feature subset is defined as the average MI between each feature $f_i \in S$ and the class label:

$$D(S) = \frac{1}{|S|} \sum_{f_i \in S} MI(f_i; c)$$

The redundancy among the selected features is expressed as the average pairwise MI between features:

$$R(S) = \frac{1}{|S|^2} \sum_{f_i, f_j \in S} MI(f_i; f_j)$$

The mRMR objective seeks to maximize the relevance of the selected subset while minimizing redundancy, so maximizing:

$$\Phi(S) = D(S) - R(S)$$

The algorithm proceeds iteratively: starting from an empty feature set, it adds the features that mostly increments the MI between the features subset and the class label.

3.4.3.1.2 ReliefF

ReliefF is a filter-based feature selection algorithm that estimates the importance of each feature based on how well it distinguishes between samples of different classes while remaining stable within samples of the same class.

For each randomly chosen instance R, the algorithm identifies its nearest neighbors:

- the nearest hits, samples from the same class as R.
- the nearest misses, samples from different classes.

A feature is assigned to a higher weight if its value differs significantly between classes (high inter-class separation) but remains similar within the same class (low intra-class variation).

After many iterations across random samples, ReliefF produces a ranked list of features based on their average weight. Features with positive or high scores are considered informative, while features with low or negative scores are likely irrelevant.

ReliefF is computationally efficient and robust to feature correlations and noise. It also naturally handles multiclass problems and continuous variables (through variants such as RReliefF). Because it evaluates features in a local neighborhood context, it is particularly effective for datasets where class boundaries are non-linear or there is interaction between variables. [182]

3.4.3.2 Wrapper methods

Wrapper methods evaluate the quality of feature subsets by training and testing a predictive model on them. Unlike filter approaches, wrapper methods treat feature selection as a search problem in the feature space, guided by the performance of a specific learning algorithm [183].

Subsets of features are generated and evaluated iteratively, using strategies such as forward selection (progressively adding features), backward elimination (progressively removing features), or heuristic/randomized search (e.g., genetic algorithms or simulated annealing).

At each iteration, the classifier's performance metric, typically accuracy, F1-score or balanced accuracy, is used to decide whether to retain or discard a feature subset.

Although wrapper methods often achieve high predictive accuracy, they are computationally demanding, especially when the number of features is large. They are also prone to overfitting if the evaluation is not properly regularized or cross-validated.

Nevertheless, when sufficient data are available, wrapper methods can produce feature subsets optimized for the chosen classifier, providing better real-world performance than purely filter-based selection [180][183].

3.4.3.3 Embedded methods

Embedded methods integrate feature selection directly into the model training process. In this framework, the learning algorithm itself determines which features are most informative while optimizing its internal objective function [179].

A prominent example is the Least Absolute Shrinkage and Selection Operator (LASSO), a linear or logistic regression model that applies an L_1 regularization penalty to the weight vector:

$$\min_{\mathbf{w}} \ \| y - X\mathbf{w} \|^2 + \lambda \| \mathbf{w} \|_1$$

Equation 3.1 LASSO L_1 regularization penalty

The L_1 penalty encourages sparsity by driving less informative feature coefficients toward zero, thereby performing automatic feature selection.

In DTrees algorithms, feature selection occurs at each node split, where the model chooses the feature that maximally reduces impurity (e.g., Gini index or entropy). The hierarchical tree structure inherently ranks features by their contribution to prediction, and irrelevant variables tend not to appear in the final model.

Random Forests, as ensembles of DTrees, generalize this idea by averaging feature importance across multiple randomized trees. Each tree is trained on a bootstrap sample of the data, and at each split, a random subset of features is considered. This mechanism yields robust estimates of feature importance, often measured as the mean decrease in impurity or mean decrease in accuracy upon permutation.

3.4.4 Classification

Finally, the selected features are provided to a classifier that learns the mapping between input features and output labels (e.g. FoG, preFoG, or noFoG). Among the numerous available algorithms, SVM and RF have emerged as the most common and reliable in FoG literature due to their balance between accuracy, interpretability, and robustness on relatively small datasets [184].

3.4.4.1 Support Vector Machines

SVM are among the most established and widely used algorithms for supervised classification problems. Their idea is to find the best possible boundary that separates data points belonging to different classes (e.g. FoG no-FoG) within a multidimensional feature space [185].

Rather than simply dividing the data, SVMs look for the optimal separating surface, called a hyperplane, that maximizes the margin between the two classes. The margin represents the distance between the hyperplane and the closest data points from each class, known as support vectors.

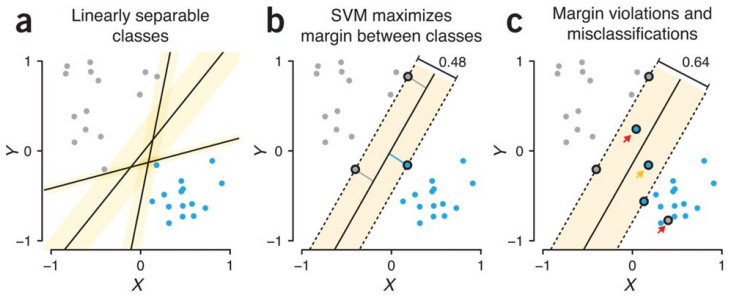

Figure 3.5 SVM 2D representation [186]

A larger margin implies that the model is more confident and tends to generalize better to unseen data, which is essential in biomedical applications where sample variability is high.

In practice, many datasets are not perfectly separable by a straight line (or hyperplane). To handle these more complex relationships, SVMs can use kernel functions, which transform the original feature space into a higher-dimensional one where classes become more easily separable [185].

Different kernels are available depending on the problem's nature:

- the linear kernel works well when data are roughly separable in their original form.
- the polynomial kernel allows capturing interactions between features.
- the radial basis function (RBF) kernel, the most commonly used, is capable of modeling highly nonlinear boundaries.

One of the main advantages of SVMs is their robustness in situations with limited and noisy data. Unlike other classifiers that may overfit when trained on small datasets, SVMs rely only on a subset of the training samples, the support vectors, to define the decision boundary. This property makes them particularly suitable for clinical and biomedical studies, where the number of subjects is usually small compared to the number of extracted features.

3.4.4.2 Decision Trees

DTrees represent one of the most intuitive and interpretable machine learning models and have been applied in several studies on FoG detection. A DTree recursively partitions the feature space into regions that are as homogeneous as possible with respect to the target variable (e.g., FoG vs. noFoG).

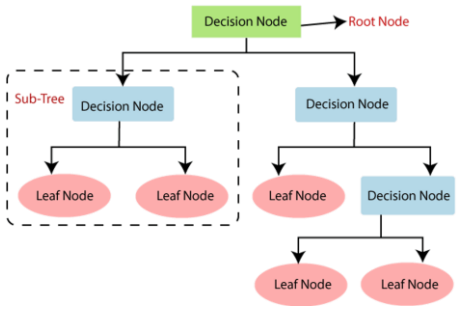

Figure 3.6 DTree schematic representation [187]

At each node, the algorithm selects the feature and threshold that maximize the information gain, typically measured through impurity metrics such as Gini index or entropy [188].

$$Gini(D) = 1 - \sum_{i=1}^{C} {p_i}^2$$

Equation 3.2 Gini Index

The final leaves of the tree represent decision outcomes, which can be easily visualized and interpreted in clinical contexts.

In FoG research, DTrees have been employed both as standalone classifiers and as building blocks for more advanced ensemble methods. When used individually, they offer high interpretability and low computational cost, allowing clinicians to understand which features contribute most to the detection of FoG.

For example, models trained on kinematic or EMG features often highlight measures of signal energy, variability, or frequency content as key discriminators between freezing and normal walking [168][189]. However, DTrees can suffer from overfitting, particularly when trained on small datasets or when the number of features is large relative to the number of samples, a common condition in FoG studies.

To overcome these limitations, ensemble variants such as RF and GBT were introduced, leveraging multiple decision trees to achieve improved robustness and generalization. Nevertheless, the simplicity and explainability of individual DTree continue to make them a valuable tool for exploratory analyses and for identifying relevant physiological features associated with FoG.

3.4.4.3 Random Forests

RF is an ensemble method which builds a collection of DTrees and aggregates their outputs to form a robust consensus prediction [190].

To reduce overfitting and improve generalization, RF exploits the concept of randomness, introduced in two ways:

1. by training each tree on a bootstrap sample of the original dataset
2. by selecting a random subset of features at each node split

This dual randomization reduces correlation among trees, helping the ensemble avoid overfitting and improving its ability to generalize to new data, and, because each tree captures slightly different relationships among features, their combination yields a more balanced model capable of handling noisy and heterogeneous data.

An additional advantage of RFs is their ability to estimate feature importance, providing interpretable insights into which variables contribute most to the classification outcome. In FoG detection, this has been used to identify the most discriminative features, helping to uncover physiological correlates of FoG episodes [160].

3.4.4.4 Gradient Boosting Trees

GBT is an ensemble learning method that constructs a strong predictive model by combining multiple weak learners, typically shallow decision trees, in a sequential manner.

At each iteration, a new tree is trained to predict the residual errors of the ensemble built so far, effectively minimizing a loss function through gradient descent in the functional space.

This iterative correction process allows the model to progressively improve its predictive capability, capturing complex non-linear relationships and feature interactions that single trees or linear models may fail to represent [191].

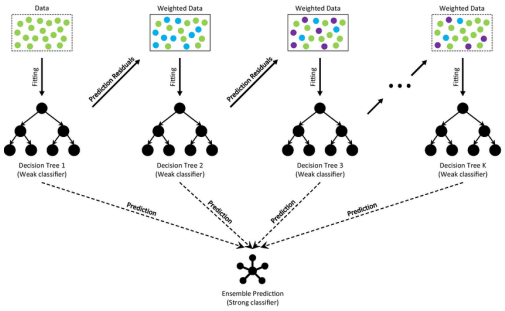

Figure 3.7 Schematic representation of GBT [192]

Each individual tree contributes a small amount to the final prediction, controlled by a learning rate that governs the trade-off between model complexity and generalization. Regularization strategies (such as limiting tree depth) are often used to prevent overfitting which can occur when the number of boosting stages is large.

In the context of FoG detection, GBT is often used thanks to its ability to model non-linear relationships and feature interactions, which makes it suitable for multimodal datasets combining kinematic, muscular, and cortical features, where the relationship between variables is often complex [168].

3.4.4.5 k-Nearest Neighbors

kNN algorithm is one of the simplest and most intuitive methods for supervised classification. Rather than learning an explicit model during training, kNN performs classification based directly on the similarity between data samples.

When a new instance is presented, the algorithm identifies the k most similar examples (the nearest neighbors) from the training set, typically using a distance metric such as Euclidean, Manhattan, or cosine distance, and assigns the class that is most frequent among those neighbors [193].

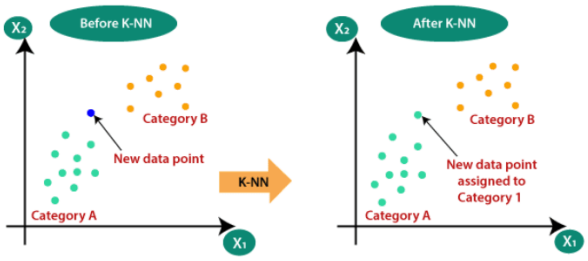

Figure 3.8 kNN 2D representation [194]

This instance-based learning approach means that kNN has no training phase in the conventional sense: all computation happens at prediction time. As a result, the method can adapt flexibly to the shape of the data distribution without assuming any particular functional form, which makes it well suited for nonlinear or irregular relationships between features and labels.

The choice of the parameter k strongly influences model behavior.

- A small k (e.g., 1-3) makes the classifier more sensitive to noise, as decisions depend heavily on a few nearby points.
- A larger k smooths the decision boundary by considering more neighbors, improving robustness but potentially blurring fine distinctions between classes.

In practice, k is typically optimized through cross-validation to balance sensitivity and generalization.

Because kNN relies on distance computations, feature scaling and normalization are crucial: features with larger numerical ranges can otherwise dominate the distance metric and bias the classification. This is particularly relevant in multimodal datasets, where features may have very different units and magnitudes.

In FoG research, kNN has been successfully applied to wearable-sensor data for its simplicity and ease of interpretation [168]. Despite its computational cost at inference time, kNN performs well when the dataset is of moderate size and the feature space is not excessively high-dimensional.

3.4.4.6 LASSO Logistic Regression

Beyond its role in feature selection, the LASSO can also serve as a powerful classification model when applied within the framework of logistic regression.

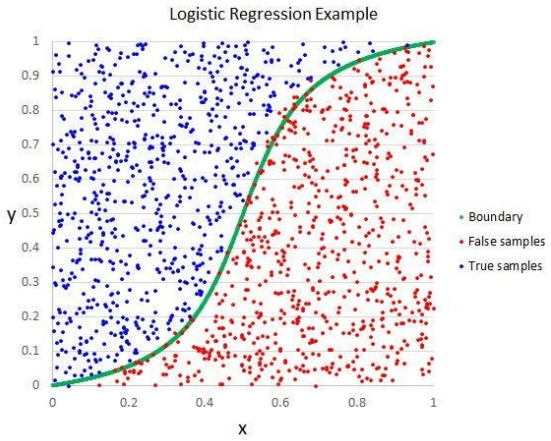

Figure 3.9 Logistic Regression 2D representation [195]

In this context, LASSO estimates the probability that an observation belongs to a particular class (e.g., FoG vs. noFoG) based on a weighted linear combination of features, while enforcing a sparse representation through L_1 regularization [196].

Unlike unregularized logistic regression, which may overfit when the number of predictors is large relative to the number of samples, the LASSO variant naturally constrains model complexity by retaining only the most discriminative features.

From a practical perspective, the resulting model assigns non-zero weights only to features that meaningfully contribute to class discrimination, allowing direct inspection of their relative importance and direction of effect and making LASSO logistic regression particularly appealing for multimodal datasets.

3.4.5 Model evaluation strategies

The performance of a ML model can be quantified by comparing its predicted labels with the corresponding ground-truth annotations through a confusion matrix, which summarizes the number of correctly and incorrectly classified samples for each class.

		Predicted class	
True class		Positive	Negative
	Positive	TP	FN
	Negative	FP	TN

Figure 3.10 Confusion matrix

For a given class c_i, the matrix entries are defined as true positives (TP_i), false positives (FP_i), false negatives (FN_i), and true negatives (TN_i). From these quantities, several evaluation metrics can be derived, each describing a specific aspect of model behavior.

3.4.5.1 Evaluation metrics

The precision measures the proportion of correctly predicted samples among all predictions for a given class, while recall (or sensitivity) quantifies the model's ability to identify all samples belonging to that class:

$$\text{Precision}_i = \frac{TP_i}{TP_i + FP_i}, \qquad \text{Recall}_i = \frac{TP_i}{TP_i + FN_i}$$

Equation 3.3 Precision and Recall

The specificity, conversely, measures the fraction of correctly identified negative samples:

$$\text{Specificity}_i = \frac{TN_i}{TN_i + FP_i}$$

Equation 3.4 Specificity

Since precision and recall capture complementary aspects of performance, they are often combined into the F1-score, defined as their harmonic mean:

$$\text{F1}_i = \frac{2 \cdot \text{Precision}_i \cdot \text{Recall}_i}{\text{Precision}_i + \text{Recall}_i}$$

Equation 3.5 F1-score

To summarize results across multiple classes, per-class metrics can be averaged in different ways: the macro-averaged scores compute the unweighted mean across classes, treating all classes equally, while the weighted averages account for the number of samples in each class.

In addition, the balanced accuracy, corresponding to the average recall across classes, provides a robust measure of overall sensitivity, especially in the presence of class imbalance:

$$\text{Balanced Accuracy} = \frac{1}{K}\sum_{i=1}^{K} \text{Recall}_i$$

Equation 3.6 Balanced Accuracy

where K is the total number of classes.

In binary classification problems, precision, recall, and F1-score are typically reported for the positive class; in multiclass settings the Macro-F1 and Balanced Accuracy offer a more comprehensive evaluation of the model's generalization capability.

3.5 Multimodal approaches for FoG detection

As methodological development progressed, researchers recognized that relying on a single signal type may not be sufficient to capture the complex and heterogeneous manifestations of FoG. IMUs provide information on external kinematics, while sEMG captures neuromuscular activity, and neuroimaging modalities such as EEG or fNIRS probe central mechanisms.

Multimodal systems were therefore proposed to exploit complementary sources of information, aiming to improve detection robustness and generalization across patients and contexts.

3.5.1 Early multimodal studies.

Early multimodal research on FoG detection explored the complementary information contained in kinematic and muscular signals. Cole et al. (2011) [197] presented one of the first integrated approaches combining data from multiple triaxial accelerometers and a surface EMG sensor positioned on the lower limb. Using handcrafted features derived separately from IMU and EMG channels as inputs to a dynamic neural network, their system achieved 83% sensitivity and 97% specificity during unconstrained daily-life activities.

This study demonstrated that the simultaneous observation of limb kinematics and muscle activation could capture the complex motor signatures of FoG, outperforming single-sensor methods in ecological conditions.

Subsequent works, such as Tahafchi et al. [173], adopted a similar multimodal configuration but implemented classical machine-learning classifiers (e.g., SVM) to discriminate between FoG and normal gait, confirming that the fusion of inertial and physiological features can increase sensitivity and reduce false alarms even under variable walking conditions.

3.5.2 Feature-level and decision-level fusion.

As multimodal approaches evolved, two main strategies for integrating heterogeneous biosignals emerged. The first involves combining the sensor data to derive composite descriptors, creating unique features that capture the interaction between modalities [160]. This method allows the extraction of integrated representations rather than treating each signal independently.

The second approach performs feature-level concatenation, in which features extracted separately from each modality are merged into a single multimodal feature vector that serves as input to machine-learning classifiers in order to improve sensitivity and robustness compared to unimodal models [173][197].

Although both approaches have proven effective, feature-level fusion remains the most widely implemented in FoG detection pipelines because of its simplicity, interpretability, and compatibility with conventional supervised learning frameworks. Conversely, composite-feature methods such as the R-index offer deeper physiological interpretability but typically require modality-specific calibration and careful signal synchronization.

3.5.3 Expanding to other modalities.

Beyond IMU-EMG integration, multimodal research has also incorporated additional physiological signals to better represent the interplay between motor and cognitive factors in FoG. For instance, Zhang et al. (2022) [174] developed a multimodal dataset combining accelerometers, EEG, EMG, and skin conductance (SC). Their analyses showed that the inclusion of central and autonomic features increased detection performance and offered insights into non-motor contributors to freezing.

Although fNIRS has been independently studied for cortical correlates of FoG (see Section 3.6), there are currently no widely reported studies combining fNIRS simultaneously with both IMU and EMG.

Nonetheless, the multimodal paradigm introduced by Zhang and colleagues represents a significant step toward multimodal characterization of FoG, promoting reproducibility and standardized benchmarking.

3.5.4 Challenges and practical limitations

Despite these encouraging results, several practical challenges still limit the routine deployment of multimodal systems. Integrating multiple sensors increases the complexity of both data acquisition and synchronization, as each modality operates at different sampling rates. Ensuring reliable time alignment across IMU, EMG, and EEG or fNIRS signals remains a technical priority for consistent feature extraction [174]

Signal quality is another concern, particularly for sEMG and fNIRS, which can be sensitive to electrode contact, motion artifacts, or optode displacement. Long-term wearability and user comfort are also critical factors, as excessive instrumentation can reduce compliance in clinical or daily-life scenarios [175].

Nevertheless, these limitations are progressively being mitigated by advances in sensor miniaturization, wireless synchronization, and integrated hardware solutions. Recent work emphasizes compact, co-located modules (e.g., IMU-EMG units) and smart textiles that embed multiple sensors in a single wearable interface, substantially improving comfort and practicality without compromising data richness.

Ultimately, the continued evolution of multimodal FoG detection research lies in striking a balance between technical performance and real-world usability, ensuring that the systems not only achieve high accuracy but also remain acceptable for everyday use by patients with PD.

3.6 fNIRS-based approaches for FoG detection and characterization

While inertial and electromyographic sensors capture peripheral manifestations of FoG, fNIRS offers a complementary window into cortical hemodynamic, allowing to monitor changes in HbO and HbR concentrations in the cerebral cortex during walking tasks, even in free ambulation, making it particularly suitable for studying FoG mechanisms.

3.6.1 Early studies and rationale

Initial fNIRS investigations in Parkinson's disease showed that patients with FoG exhibit greater prefrontal cortex (PFC) activity during demanding walking conditions such as dual-tasking or turning, compared to patients without FoG and healthy controls [162]. These findings suggested that FoG is associated with an increased reliance on executive control, consistent with theories of impaired automaticity of gait.

3.6.2 Event-related approaches

More recent work has moved from generic comparisons of "walking vs rest" to event-related paradigms specifically designed to elicit FoG. For example, Feng et al. [198] investigated cortical activation and connectivity during turning and doorway tasks, comparing episodes of FoG with clean turns and with preFoG periods. They found significant alterations in frontal and SMA activation in freezers, highlighting impaired cortical recruitment during gait transitions. Similarly, other studies have contrasted FoG vs non-FoG episodes within the same locomotor tasks, confirming differential PFC and SMA dynamics around episode onset [161].

3.6.3 Regional imbalance and mechanisms

Evidence converges on the notion that FoG involves an imbalance between cortical regions: hyperactivation of the PFC during freezing-prone tasks, combined with reduced or poorly timed SMA engagement.

Cockx et al. [161], using fNIRS during free ambulation, reported that patients with FoG displayed abnormal coordination between frontal executive and motor planning areas, consistent with disrupted cortical-subcortical communication. These results align with electrophysiological studies suggesting decoupling of motor and cognitive networks.

3.6.4 Methodological considerations

Despite variability across studies, most fNIRS analyses adopt similar pipelines: motion and physiological artifact correction, removal of superficial hemodynamics (often with SSc regression), and GLM estimation of task-related responses [199].

Statistical contrasts are then performed between FoG and control conditions (e.g., FoG vs clean turns, FoG vs preFoG), followed by group-level analysis to account for inter-subject variability. These methodological choices are essential to increase specificity and reproducibility in mobile fNIRS studies.

Although the literature is still limited compared to IMU and EMG-based approaches, fNIRS provides critical insights into the central mechanisms of FoG and represents a promising avenue for multimodal systems that aim to integrate cortical, muscular, and kinematic information.

4 Materials and Methods

4.1 Patients Cohort

Eleven patients diagnosed with idiopathic PD were enrolled in this preliminary study. Participants were recruited at IRCCS Ospedale San Raffaele, according to the following inclusion criteria: H&Y score ≤ 4, PIGD phenotype, stable dopaminergic medication for at least 4 weeks, no dementia and Mini-Mental Status Examination score (MMSE) ≥ 24.

Participants were stratified into two subgroups based on their clinical history and experience of freezing episodes:

- FoG group (n = 4): patients who reported experiencing freezing of gait episodes on a daily basis.
- noFoG group (n = 7): patients without self-reported or clinically observed freezing episodes.

Demographic and clinical information, including age, sex, disease duration, LEDD, H&Y stage, MDS-UPDRS part III scores, Montreal Cognitive Assessment (MoCA), and NFOG-Q scores, were collected prior to the experimental session. All subjects underwent both motor and cognitive assessments as part of the baseline characterization.

All participants provided written informed consent prior to inclusion. The study protocol was conducted in accordance with the principles of the Declaration of Helsinki.

A detailed summary of the cohort's demographic and clinical characteristics is reported in *Table 4.1*.

Group	*Code*	*Age*	*Sex* *0 = male 1 = female*	*Education*	*Disease Duration*	*LEDD*	*UPDRS-III (ON)*	*H&Y (ON)*	*MoCA*	*nFoG-Q*
PD-FoG	PD_001	73.9	0	20	14	898	27	2	22	17
	PD_003	68.5	0	13	13	650	39	2	26	20
	PD_004	59.7	0	8	4	300	45	3	19	11
	PD_005	73.6	0	12	15	1455	39	2.5	21	26
PD-noFoG	PD_006	74.9	0	8	4	300	28	2	23	0
	PD_007	55.6	1	13	15	710	26	2	25	0
	PD_008	66.0	0	13	5	430	25	2	27	0
	PD_009	72.9	0	13	7	575	30	2	26	0
	PD_010	61.2	0	11	4	439	46	2	24	0
	PD_011	62.6	1	18	7	405	44	2	23	6
	PD_012	81.1	0	8	4	300	36	2.5	23	0
PD-FoG	**Average**	68.9	4/0	13.3	11.5	825.8	37.5	2.4	22.0	18.5
	Stdev	6.6		5.0	5.1	486.0	7.5	0.5	2.9	6.2
PD-noFoG	**Average**	67.8	5/2	12.0	6.6	451.3	33.6	2.1	24.4	0.9
	Stdev	8.9		3.5	4.0	147.6	8.6	0.2	1.6	2.3
p-Values		0.850	0.500	0.777	0.257	0.186	0.450	0.299	0.108	0.008 *

*Table 4.1 Cohort demographic and clinical characteristics. Between-group comparisons were conducted to assess potential demographic or clinical differences: continuous variables were analyzed using the Wilcoxon Rank-Sum Test, while categorical variables were compared using the Sign Test. Statistically significant differences are indicated with *.*

4.2 Experimental Protocol

The experimental tasks were part of a broader study investigating the effects of transcranial direct current stimulation (tDCS) on FoG in PD.

The protocol included multiple sessions to test the effects of different stimulation sites compared to the baseline; however, the present work focuses exclusively on the first experimental session (baseline), during which no stimulation was applied. Multimodal recordings (fNIRS, EMG, IMU) were acquired during motor tasks designed to evaluate patients' gait on straight paths and turns and elicit FoG episodes.

During this initial session, participants underwent a baseline evaluation consisting of:

- Clinical assessments, including the MDS-UPDRS part III, H&Y stage, MoCA, 10-Meter Walk Test (10MWT), Timed Up and Go (TUG), and NFOG-Q.
- Cognitive baseline tasks, including the Phonemic Fluency Task (PFT) and a Backwards Counting Task (BCT), used to evaluate DT interference during subsequent motor assessments.

PFT required participants to say as many words as possible, beginning with a specified letter within two minutes, with the target letter changing every minute.

BCT consists in counting backward from a given number by repeatedly subtracting a fixed value. Different difficulty levels were defined by varying both the starting number and the subtraction step, with higher values corresponding to more demanding conditions. The difficulty level related to each specific patient was defined in the baseline and kept the same during the DT walk trial, changing the starting value in each session to prevent learning effects.

Following these evaluations, participants performed seven motor tasks under fNIRS-EMG-IMU monitoring, all at the highest feasible speed under safe and controlled conditions in a laboratory environment, with safety personnel present to prevent falls.

For each task, both a minimum performance criterion (e.g., completing at least ten back-and-forth trials) and time constraints were defined. Participants were required to continue the task until the minimum duration was reached, even if the performance criterion had already been met. Conversely, if the maximum duration was exceeded, typically due to prolonged freezing episodes or fatigue, the task was stopped regardless of the achieved performance.

4.2.1 360 degrees turn

In the first motor task, the patient was asked to complete six 360 degrees turns in both directions, while standing in a 50x50 cm box. The minimum duration was one minute, while the maximum duration was two minutes.

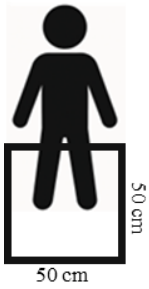

Figure 4.1 Turn 360 task setup

After this first task, the expert evaluator identified the direction in which the patient exhibited greater difficulty, that will be indicated as GDD (greater difficulty direction), while the other direction will be indicated as LDD (lower difficulty direction).

4.2.2 Dual task walking (PFT), turn in GDD

In the first walking task, patients were instructed to walk in a controlled environment consisting of two 50x50 cm boxes placed 8 meters apart along a straight path.

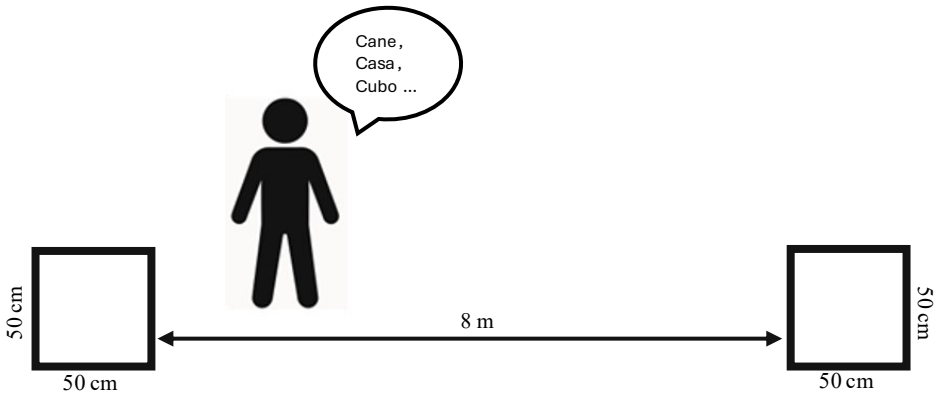

Figure 4.2 PFT walking setup, turn in GDD

Patients repeatedly walked back and forth between the two boxes, completing at least ten 180 degrees turns inside them, always in their GDD, in a time range between two and four minutes. The DT condition associated with this task was PFT, considered less demanding compared to BCT.

4.2.3 Single task walking, turn in GDD and LDD

After the first DT walking task, two ST walking task were performed, in which the same walking setup was maintained, but no cognitive task was performed.

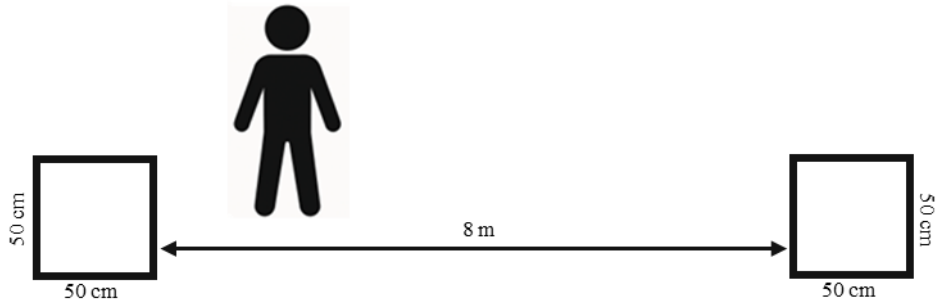

Figure 4.3 ST walking setup

In one task patients had to turn in their GDD, while in the other in their LDD. Both tasks' minimum duration was two minutes, while maximum duration was four minutes.

These two tasks served as motor-only reference, to allow comparison between ST and DT conditions.

4.2.4 Dual task walking (BCT), turn in LDD

A further DT trial was performed in the LDD, under the same spatial configuration and task characteristics (duration and performance constraints). Patients were instructed to walk back and forth between the boxes while performing BCT (e.g. backwards counting from 285 subtracting 7).

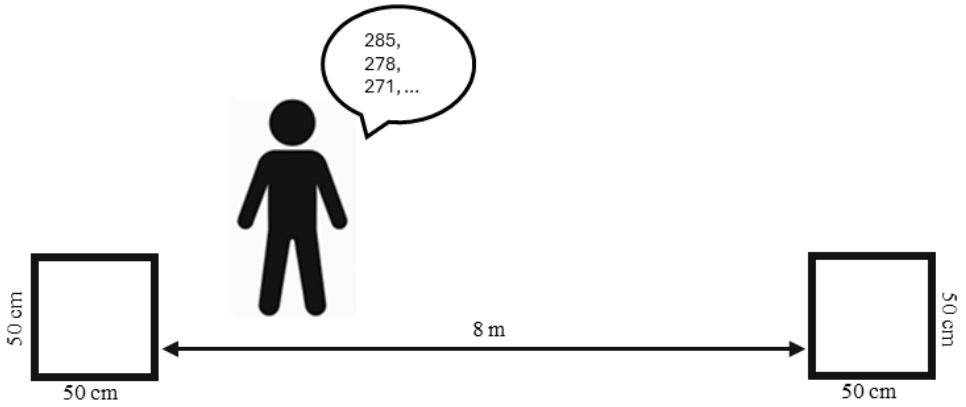

Figure 4.4 BCT walking setup, turn in LDD

4.2.5 Color-Direction Dual Task walking

In the final DT condition, patients performed the same walking task between the two boxes, but with an externally cued color-direction rule. Before the trial, each patient was instructed about a color-direction association (yellow = right, blue = left or vice versa).

During the walking task, immediately before each turn inside the box, the examiner verbally announced a color cue, and the patient was required to turn in the corresponding direction.

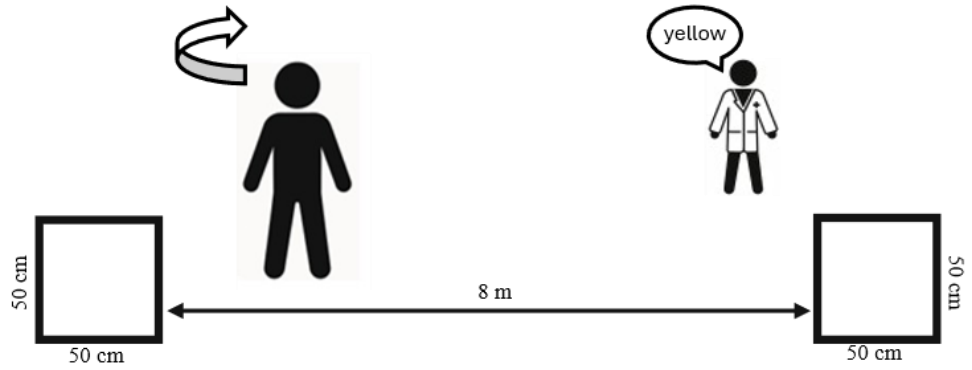

Figure 4.5 Color-Direction DT walking setup

This paradigm prevented patients from preparing the turn in advance and introduced an element of unpredictability, with the aim to increase the likelihood of FoG episodes.

4.2.6 Single-task Cone Walking

Two additional ST conditions were performed to obtain clean turning references with minimal freezing risk. Patients walked along an 8-meter path delimited by cones, performing controlled 180° turns around the cones at each end.

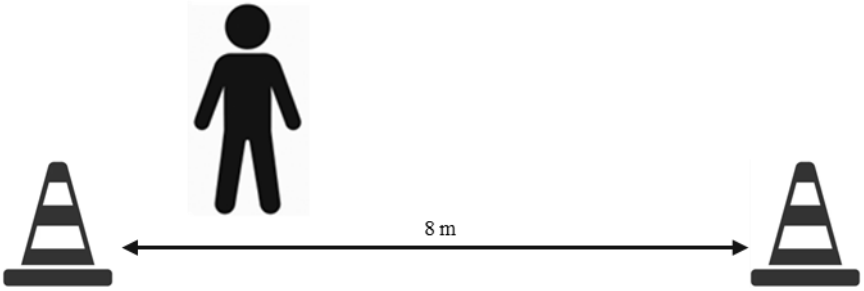

Figure 4.6 ST cone walking setup

This configuration was chosen to provide larger turning trajectories and to capture gait and turn dynamics under conditions less likely to induce FoG episodes, serving as reference for subsequent comparisons. Consistently, no FoG episodes were observed during the cone trials, confirming the validity of this assumption.

4.3 Experimental Setup

A multimodal acquisition setup was designed to simultaneously record cortical, muscular, and kinematic activity during previously described motor tasks. The system integrated fNIRS, sEMG and IMUs, all synchronized through a dedicated trigger and software interface.

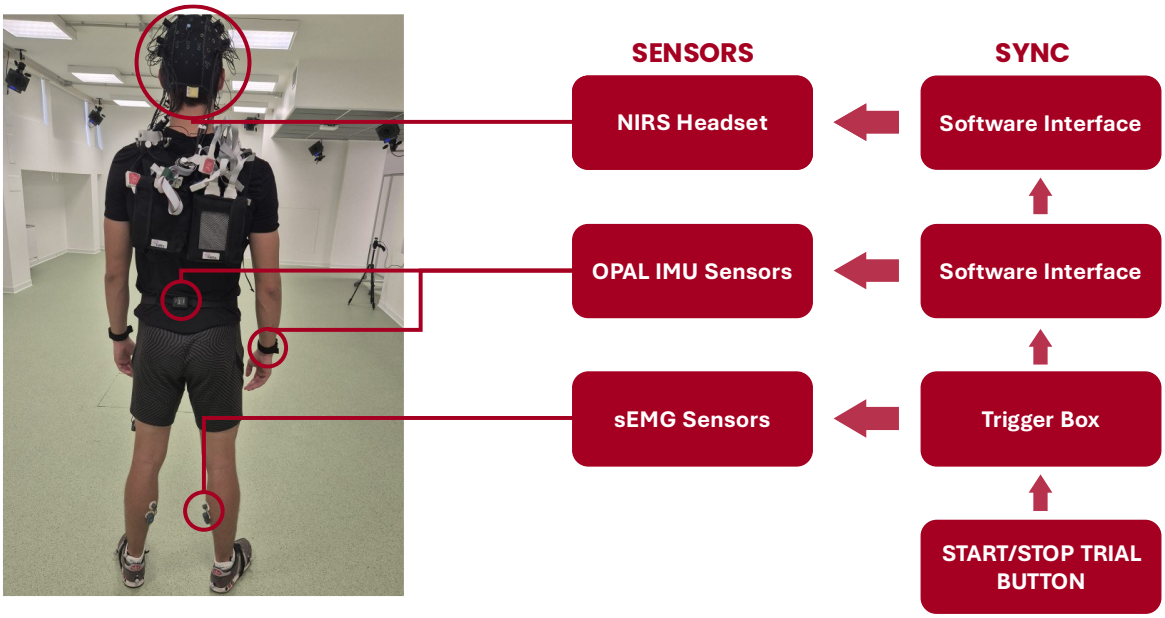

Figure 4.7 Experimental Setup: hardware and synchronization strategies

4.3.1 fNIRS Setup

In this study, cortical hemodynamic activity was measured using the NIRSport2 system (NIRx Medical Technologies, Berlin, Germany), a portable fNIRS instrument designed for multichannel brain imaging in both laboratory and unconstrained environments.

Figure 4.8 NIRSport2 system [200]

It operates in CW mode with dual-wavelength LEDs at 760 nm and 850 nm, selected to capture changes in HbO and HbR concentrations.

The configuration included 16 sources and 15 detectors, forming 52 long-separation channels with a source-detector distance of 3 cm, and 8 short-separation channels (SSc) with a distance of 8-15 mm.

The optode montage was arranged to cover frontal and motor cortical areas previously associated with FoG episodes, including PFC, SMA, and premotor regions [162], according to fMRI findings during feet motor tasks [201].

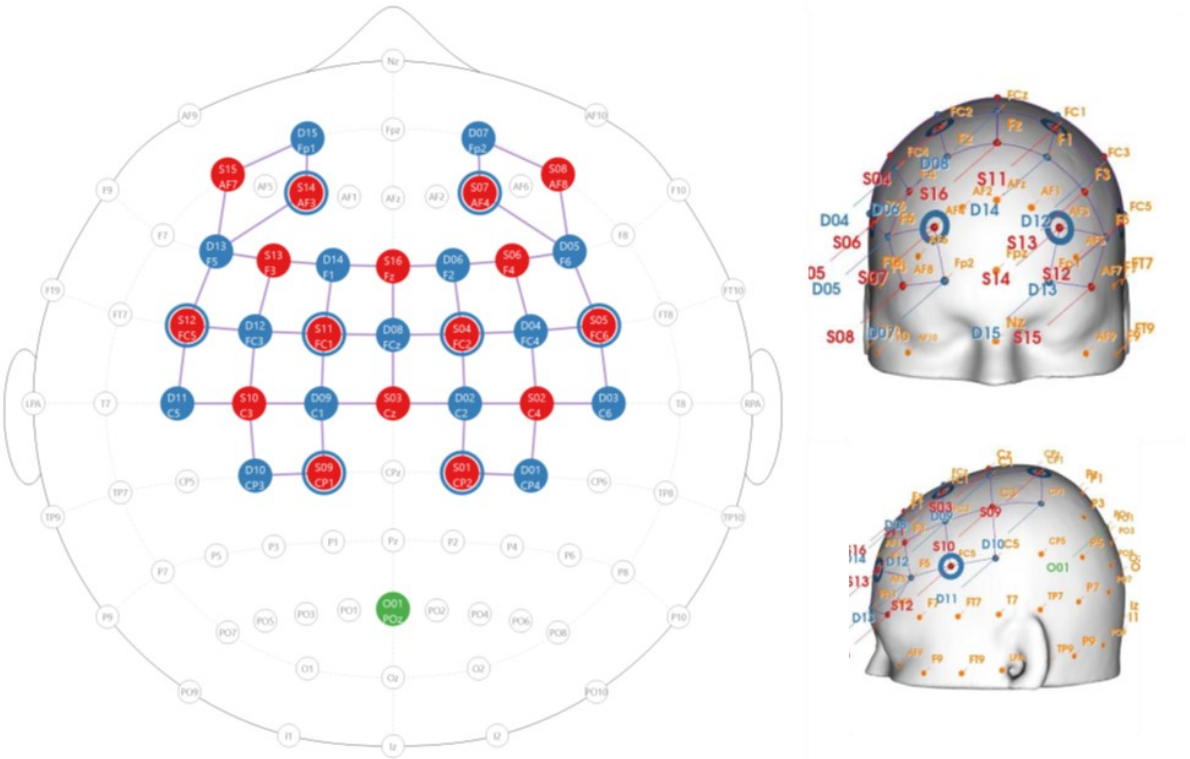

Figure 4.9 Selected optode configuration in 10-20 system. Sources are red circles, detectors are blue circles, SSc are blue circles around the sources and the imu sensor is the green circle.

Data were sampled at 5 Hz and recorded using Aurora NIRS acquisition software, which provides real-time monitoring of optode coupling quality and signal stability.

The optical cap was adapted to the participant's head size using the international 10-20 coordinate system to ensure consistent positioning across subjects. Signal quality was visually inspected before each trial, and channels with poor coupling were readjusted prior to acquisition.

The NIRSport2 headset incorporates one 6-DOF IMU, with 100 Hz sampling frequency, to allow motion monitoring and artifact handling during acquisition, and in our case to check the synchronization between the systems.

4.3.2 IMUs Setup

Kinematic data were acquired using Opal sensors (APDM Wearable Technologies, Portland, OR, USA), each comprising a triaxial accelerometer, gyroscope, and magnetometer (9 DOF).

Figure 4.10 Opal sensor [202]

Opal sensors record signals at a sampling frequency of 128 Hz, with a 16-bit resolution on each axis, and employ onboard sensor-fusion algorithms (based on Kalman filtering) to compute real-time orientation estimates and are wirelessly synchronized and transmitted to a central hub [145].

Sensors were positioned on the feet, lumbar vertebra, sternum, and wrists capturing linear and rotational dynamics relevant to gait and turning maneuvers typically associated with FoG.

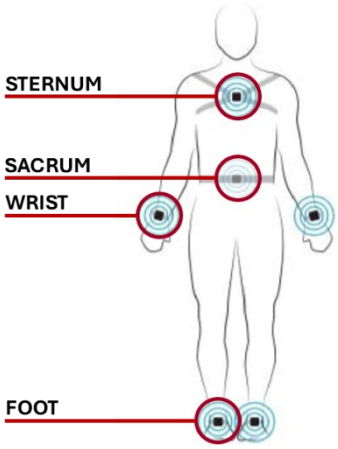

Figure 4.11 IMU sensors setup

The IMU system was managed via Mobility Lab software, which ensured synchronized data collection and automatic timestamp alignment with the other modalities through shared trigger inputs.

4.3.3 sEMG Setup

Muscle activity was recorded using a FreeEMG system (BTS Bioengineering, Milan, Italy), equipped with wireless probes employing Ag/AgCl bipolar electrodes.

Figure 4.12 FreeEMG system [203]

Each FreeEMG sensor acquires sEMG activity with 1000 Hz sampling frequency, pre-amplifies it on board, and wirelessly send the data to a receiver.

A total of 10 EMG channels were used, targeting bilateral lower-limb muscles crucial for gait initiation and postural transitions: Tibialis Anterior, Gastrocnemius Medialis, Rectus Femoris, Biceps Femoris, and Gluteus Maximus.

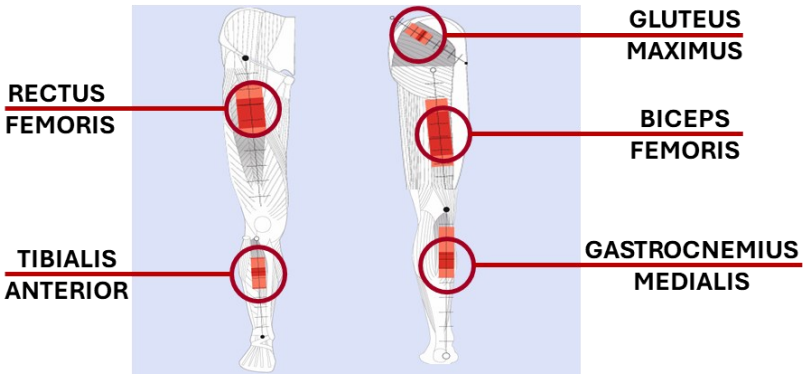

Figure 4.13 sEMG sensors setup [204]

Electrodes were placed following SENIAM recommendations [98] for inter-electrode distance and orientation, ensuring reproducibility and minimizing crosstalk.

4.3.4 Multimodal Synchronization

To ensure temporal alignment across the fNIRS, EMG, and IMU systems, a custom hardware-software synchronization architecture was implemented.

The synchronization relied on a BTS Trigger Box, an Arduino nano microcontroller, and a Lab Streaming Layer (LSL) interface that allowed all acquisition software to start and stop simultaneously with a single command.

Figure 4.14 BTS Trigger Box

The start input was delivered manually through a push button connected to the BTS Trigger Box, which controlled the BTS acquisition system (sEMG and video cameras), through an Arduino board, programmed to invert its digital output state at each button press.

The Arduino was powered via a standard USB connection, and its serial output was read directly, allowing software-level detection of the trigger event, which triggered two mechanisms:

- Sending an LSL stimulus to Aurora (NIRx), to set the start or the end of fNIRS acquisition
- Simulating a click on Mobility Lab interface's start/stop button

This configuration enabled near-perfect simultaneous initiation of all acquisition systems, ensuring that fNIRS, EMG, and IMU recordings started with minimal temporal offset despite the absence of direct hardware coupling between devices.

To guarantee full temporal precision, synchronization accuracy was subsequently verified and post hoc correction procedures were applied to compensate for the residual inter-system delay.

4.3.4.1 Inter-system delay quantification and correction

To quantify the delay among the three acquisition systems, two complementary approaches were employed.

fNIRS-IMU delay was estimated by computing the cross correlation between the acceleration magnitude of the Opal sensor positioned on the sternum and the signal from the auxiliary accelerometer mounted on the fNIRS cap.

$$R_{xy}[\tau] = \sum_{t} x[t] \cdot y[t+\tau]$$

Equation 4.1 Cross Correlation between two discrete signals x[t] and y[t]

Where $x[t]$ and $y[t]$ are the two signals and τ is the delay.

Before computing the cross-correlation, the mean value of both signals was removed to avoid introducing bias in the correlation estimation.

By identifying the delay corresponding to the cross correlation maximum value, it is possible to estimate the lag between the two signals. The search for the delay was restricted to the 0-3 s interval, as the expected lag was below one second and wider windows could introduce spurious correlations.

IMU-sEMG/video delay was quantified by identifying the first step event in both the video recordings and the gyroscope signal of the lower-limb Opal sensors *(see 4.4.1)*.

4.4 Events Definition

4.4.1 Step detection

Step detection was performed on the angular velocity signals recorded by the Opal IMUs positioned on the feet, following a custom algorithm derived from the framework proposed by Renggli et al. (2020) [151] and Borzì et al (2021) [176].

The gyroscope signal was first normalized and band-pass filtered between 0.5 and 5 Hz to remove high-frequency noise and baseline drifts, preserving the cyclical pattern associated with gait dynamics.

$$\omega_y' = \frac{\omega_y - mean(\omega_y)}{max(\omega_y) - min(\omega_y)}$$

Equation 4.2 Angular velocity normalization [176]

Within the filtered waveform, the positive peaks corresponding to the maximum angular velocity during the mid-swing phase were identified and labeled as MAX events.

For each MAX event, the TO was defined as the first negative peak preceding the MAX, representing the instant of foot lift-off, while the HS-end was defined as the first negative peak following the MAX, corresponding to the impact of the foot with the ground.

When available and within a reasonable temporal distance, the Step Start was aligned with the HS-end of the preceding step; otherwise, it was approximated by the TO of the current cycle. This procedure allowed for the precise segmentation of the gait signal into individual steps, ensuring consistent identification of stance and swing phases across subjects and trials.

The resulting event markers (Step Start, TO, MAX, HS-end) were subsequently used to extract gait parameters and to temporally align the annotations of walking, turning, and FoG periods with the corresponding step occurrences.

4.4.2 Turn identification

Turn detection was performed on the angular velocity signal acquired from the lumbar Opal IMU, which provides a stable representation of trunk rotation around the vertical axis.

Turn detection was implemented via a hysteresis thresholding scheme on the yaw angular velocity from the lumbar IMU. Turns were identified when $|\omega_{yaw}|$ crossed an upper threshold (15 °/s), while turn onset and offset were defined as the first samples before/after the upper crossing at which $|\omega_{yaw}|$ fell below a lower threshold (5 °/s).

Adjacent turning segments separated by short intervals below a minimum duration threshold (50 ms) were merged to account for natural variability in turning behavior, whereas segments shorter than the minimum valid duration (0.5 s) were excluded to eliminate spurious detections caused by small fluctuations or noise.

The algorithm was based on the method proposed by El-Gohary et al. (APDM, 2013) [153], adapted to the current experimental setup.

Following automatic detection, each trial was divided into turn and walk phases, the latter corresponding to all segments outside the turning intervals. These phases were then realigned

with the corresponding HS events obtained from the step-detection procedure, in order to capture the intention to initiate a turn or a walk rather than the isolated event itself.

This alignment ensured a consistent temporal correspondence between step-level kinematics metrics and higher-level events (walk, turn, and FoG).

4.4.3 FoG and preFoG definition

The identification of FoG and pre-FoG episodes was performed through manual video annotation, gold standard in FoG detection studies, using the ELAN software, which is recognized as a reliable tool for event labeling in gait studies [39].

Two independent evaluators, both experienced in movement-disorder assessment, annotated all video recordings to mark the onset and offset of FoG episodes, as well as periods of altered turns, turning maneuvers that were not classified as true FoG events but deviated from the subject's typical performance.

Altered turns were excluded from the primary analysis, as they do not represent either physiological turning or true freezing behavior.

The pre-FoG period was defined as a 2-second window preceding the onset of each FoG episode, in accordance with previous literature [157][176]. This temporal window was used to capture potential anticipatory changes in motor, muscular, and cortical activity prior to freezing onset.

When event overlaps occurred, a priority rule was applied to preserve event consistency:

- FoG and pre-FoG labels always took precedence over other annotations
- when an altered turn overlapped with a standard turning event, the entire segment was reclassified as altered turn.

Like for turn and walk events, also FoG boundaries were referenced to step events derived from the IMU-based detection described in *Section 4.4.1*.

Specifically, the FoG onset was aligned with the last HS event preceding the beginning of freezing, while the FoG offset corresponded to the first TO event following its termination.

4.5 Signals Processing

4.5.1 fNIRS Signals processing

fNIRS data were processed using NIRSTORM, a plugin for Brainstorm, which is an open-source MATLAB toolbox for multimodal neuroimaging analysis [205].

The preprocessing pipeline was designed to remove motion and physiological artifacts, remove non cortical hemodynamic components, and convert raw optical intensities into cortical hemodynamic activity maps.

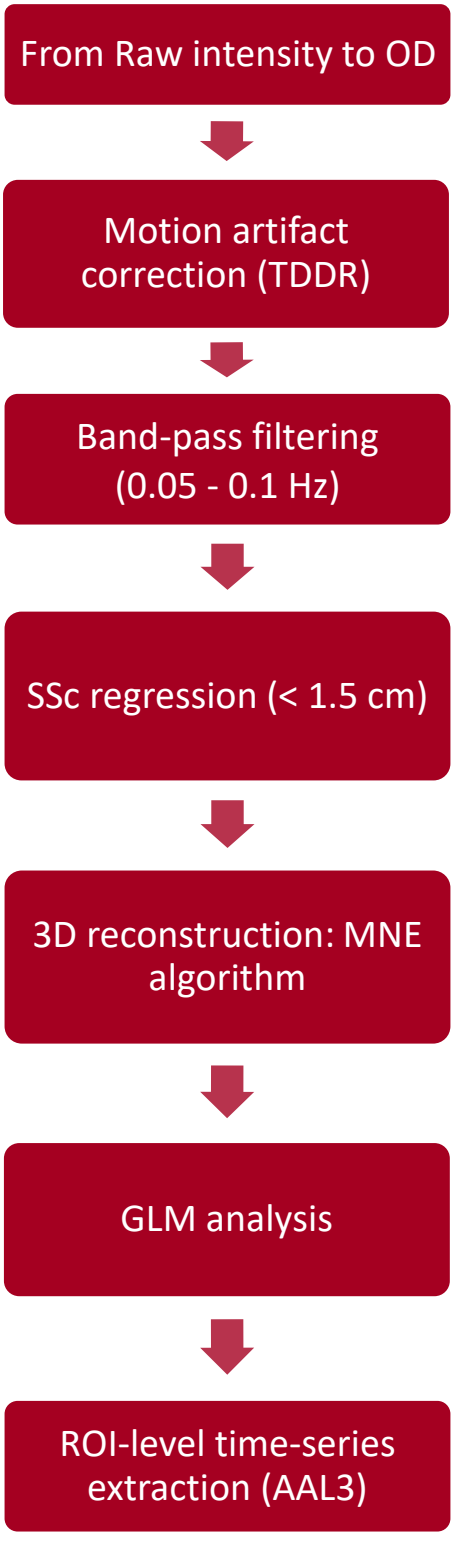

Raw light-intensity signals from the two wavelengths (760 and 850 nm) were first converted into OD.

Motion artifacts were then corrected using the temporal derivative distribution repair (TDDR) method [75], which effectively restores the temporal continuity of the signal by detecting and repairing derivative outliers.

The corrected OD signals were band-pass filtered between 0.05 and 0.1 Hz to isolate the frequency range of task-evoked hemodynamic fluctuations while removing slow drifts and high-frequency physiological noise [76].

To further suppress systemic contributions from extracerebral tissues, SSc regression was applied: the average signal from all SSc was regressed out from each long-separation channel, thereby minimizing scalp blood-flow contamination.

For spatial analysis, a 3D reconstruction was performed using the MNE algorithm, which uses photon propagation models to project channel-level data onto the cortical surface, resulting in voxel-wise hemodynamic maps.

Event-related activations were then estimated using a GLM, where event design matrices were convolved with a canonical HRF. The resulting β coefficients represented the amplitude of task-evoked responses and were used for both subject-level contrasts and group-level analyses.

To obtain region-level representations of cortical dynamics, voxel-wise HbO signals were averaged within the standard cortical ROIs of the AAL3 atlas that overlapped with the investigated cortical area.

This procedure yielded ROI-level time series describing the temporal evolution of hemodynamic activity within each region throughout the experimental tasks, providing activation-based descriptors of cortical hemodynamics, which were subsequently integrated with EMG and IMU features for multimodal analysis.

4.5.1.1 Statistical Analysis of β Maps

Event related β maps obtained from the GLM analysis were evaluated at multiple levels to capture both individual and group-level cortical activation patterns, separately for ST and DT conditions.

At the single-subject level, β values were inspected to characterize individual cortical activation patterns across the different gait-related events. This approach allowed the identification of subject-specific hemodynamic signatures associated with turning, walking, and freezing behaviors.

Paired t-tests were conducted independently within each group (PD-FoG and PD-noFoG) to explore condition-related differences while accounting for inter-subject variability.

Finally, at group level, comparisons were performed on shared conditions between PD-FoG and PD-noFoG patients to evaluate systematic differences in cortical activation related to non-FoG conditions.

4.5.2 IMU Signals processing

Inertial data were preprocessed to remove noise, standardize the reference frame, and ensure consistency across sensors and subjects.

Raw triaxial acceleration and angular velocity signals were first low-pass filtered (10 Hz cutoff frequency) to suppress high-frequency noise and mechanical vibration artifacts while preserving gait-related components.

Subsequently, each sensor's orientation was realigned to the global (earth-fixed) coordinate system using the onboard quaternion estimates provided by the Opal devices.

The resulting filtered and realigned signals were then used for event detection *(Section 4.4)* and for the extraction of quantitative features to describe gait and turning dynamics.

4.5.3 sEMG Signals processing

Surface EMG signals were preprocessed to remove potential artifacts and normalize between patients in order to mitigate variability related to electrode-skin coupling and electrode positioning differences.

First, raw traces were filtered to attenuate motion artifacts and baseline drift while preserving the physiological sEMG bandwidth, by using a 4^{th} order bandpass filter between 20 and 450 Hz.

Signals were then normalized on a per-muscle, per-task basis, scaling each channel to $[-1, 1]$ range.

$$sEMG' = 2 \cdot \frac{sEMG - min(sEMG)}{max(sEMG) - min(sEMG)} - 1$$

Equation 4.3 sEMG normalization in [-1, 1] range

4.5.3.1 Envelope extraction

The sEMG envelope was extracted by:

1. full-wave rectification
2. low-pass filtering, with a 4^{th} order filter with a cutoff frequency of 4 Hz [105]

This processing produced stable, comparable sEMG and envelope amplitude time series across muscles and sessions, suitable for subsequent epoching and feature extraction.

4.6 Features extraction

Following preprocessing, all signals were segmented into temporally synchronized 2-second epochs with 87.5% overlap between consecutive windows.

Feature extraction was performed independently for each modality, generating a multimodal dataset that captures complementary aspects of cortical, muscular, and kinematic dynamics associated with gait and freezing episodes.

4.6.1 fNIRS features

For the fNIRS modality, ROI-level time series were obtained, as described in *Section 4.5.1*, by averaging voxel-wise HbO signals within the standard cortical ROIs of the AAL3 atlas overlapping with the investigated cortical area, resulting in 65 ROIs out of 104.

From these time series, two activation-based features were extracted to characterize the temporal evolution of regional hemodynamics during the motor tasks. Specifically, for each ROI and epoch, HbO mean and the slope were computed, resulting in 130 fNIRS features.

4.6.2 IMU features

IMU-derived features were designed to capture both gait performance parameters and signal-based descriptors of lower-limb kinematics. Features were grouped into three main categories: stride-level spatiotemporal parameters, accelerometer-based features, and gyroscope-based features.

4.6.2.1 Stride-level spatiotemporal parameters

Using the step events identified in *Section 4.4.1*, a set of spatiotemporal gait metrics was computed from the foot-mounted sensors by integrating the realigned acceleration signals and correcting for drift.

For each detected step, the following parameters were extracted:

- Spatial: stride length, maximum foot clearance, outward rotation, and mean gait velocity.
- Temporal: step duration, stance and swing times, cadence, and phase-related ratios.

These metrics provide a compact description of gait performance, reflecting overall stability, step regularity, and dynamic balance.

4.6.2.2 Accelerometer-based features

From the left foot and right foot sensors, tri-axial accelerometer signals were analyzed to extract features describing amplitude, variability, and spectral composition. For each axis, the following groups of features were computed:

- Time domain: mean, STD, minimum, maximum, RMS, skewness, kurtosis, and ZC.
- Information-theoretic: SE.
- Freezing index.
- Frequency domain: peak and mean frequency.

In addition, composite 3D features were extracted, including:

- mean value of the acceleration vector magnitude.
- eigenvalues (λ_1-λ_3) of the covariance matrix among axes, representing motion anisotropy.
- lag of the first autocorrelation peak of the high pass filtered (> 2.5 Hz) acceleration vector magnitude, indicator of step periodicity.

Overall, this set yielded 76 accelerometer features.

4.6.2.3 Gyroscope-based features

Gyroscope data from the left foot, right foot, and lumbar sensors were processed to characterize rotational dynamics and inter-limb coordination. For each axis, following features were extracted:

- Time domain: mean, STD, RMS, skewness, kurtosis.
- SE.
- Frequency domain: peak and mean frequency.

Additional 3D descriptors were derived from the angular velocity vector magnitude, including the lag of the first autocorrelation peak (after high pass filtering at 0.5 Hz), which reflects the periodicity of rotational motion.

Specific metrics were also derived for particular sensors:

- Lumbar sensor: cumulative turning angle (in degrees) around the vertical axis, obtained by signal low pass filtering at 1.5 Hz, and integration.
- Bilateral coordination: inter-foot gyroscope synchrony along the mediolateral (y) axis, quantified by the maximum cross-correlation between left and right signals, as well as the average and absolute difference of their standard deviations.

This processing block yielded 81gyroscopes features in total.

4.6.3 sEMG features

sEMG features were designed to capture amplitude, waveform characteristics, spectral content, and inter-muscle coupling from each muscle's preprocessed signal and envelope.

From each muscle ten features were extracted:

- Amplitude/energy: signal Energy, envelope Mean and STD (from the rectified/smoothed envelope).
- Temporal domain: MAV, ZC, SSC, WL.
- Auto-structure: autocorrelation first-peak lag (s) and first-peak ratio (peak/zero-lag), quantifying periodicity and regularity.
- Spectral: MF (from the power spectrum).
- Information-theoretic: SE (signal complexity).

For selected antagonistic pairs, TA ↔ GC and BF ↔ RF, inter-muscle coordination was quantified by computing magnitude-squared coherence and MI between the two sEMG signals, resulting in a total of 108 sEMG features.

Category	Features	What it captures
Amplitude	Energy; MAV; Envelope Mean/Std	Overall activation level
Temporal	ZC; SSC; WL	Firing regularity/complexity
Auto-structure	Autocorr lag_1; Peak ratio	Step-cycle periodicity/regularity
Spectral	MF	Activation bandwidth
Information	SE	Signal complexity
Pairwise	Coherence; MI	Antagonist coordination

Table 4.2 sEMG features

4.6.4 Epoch's label definition

In the features extraction phase, a ground-truth label was associated to each features vector based on temporal overlap with annotated and detected events. For each epoch, the event with maximum overlap was assigned if the overlap exceeded a fixed threshold (50 % of the epoch length); otherwise, the epoch was labeled None.

4.7 Outlier identification and removal

Prior to modeling, a two-stage outlier handling procedure was applied on the multimodal feature table, restricting the analysis to walk, turn, FoG, and pre-FoG epochs (records labeled “None” and “turn_alterated” were excluded).

All operations were stratified by condition-task pair (event label + ST/DT), in order to account for task and load-specific distributions, and, within each stratum, features were processed separately by modality block (fNIRS, EMG, IMU).

4.7.1 Fixed-bounds winsorization and imputation

In the first step we computed fixed distributional bounds from the features data (mean ± 3·STD per feature), which were then held constant throughout cleaning. Using these bounds, values outside the interval were winsorized (clipped to the nearest bound).

Missing entries were imputed feature-wise with the in-bound median (fallback to the mean if the median was undefined). In parallel, we applied a conservative “10% rule” to flag low-quality epochs: an epoch was marked if ≥10% of its features in that modality fell outside the fixed bounds or were missing.

4.7.2 Density-based outlier detection

Within each stratum and modality, we then performed Local Outlier Factor (LOF) detection on z-scored features. The LOF algorithm quantifies how isolated a sample is with respect to the local density of its neighborhood, comparing the density around each point to that of its nearest neighbors. Samples located in regions of significantly lower density than their surroundings are assigned higher LOF scores, indicating that they behave anomalously relative to nearby observations.

Epochs with LOF scores exceeding mean + 1.96·STD were flagged as density outliers. LOF thus complements the univariate bounds by capturing multivariate deviations arising from atypical feature combinations.

4.7.3 Final removal and reporting

The union of flags from the 10% rule and LOF (computed independently for EMG, IMU, and fNIRS) defined the set of outlier epochs to be removed. We also summarized flags per patient to monitor the impact of cleaning (initial counts, flagged counts by modality, and percentage removed), and saved the resulting cleaned dataset for following analyses.

This pipeline combines robustness, through winsorization and imputation, with specificity provided by the multivariate LOF detection, while preserving condition-dependent statistics by estimating bounds prior to data removal and applying all steps separately within each condition-task pair and each modality.

4.8 Features dimensionality reduction

4.8.1 Statistical screening

To identify which features were most informative for distinguishing FoG from non-FoG conditions (walk, turn, and pre-FoG), a univariate statistical screening was performed using the Mann-Whitney U test, a non-parametric alternative to the t-test that does not assume normality of the data. The test was applied independently to each feature, comparing its distribution between FoG and non-FoG epochs.

To account for the large number of features tested, Bonferroni correction was applied within each modality group (fNIRS, EMG, and IMU), thus controlling the risk of false positives due to multiple comparisons. Only features with a Bonferroni-corrected p-value ≤ 0.05 were retained for further analysis, while those not meeting this criterion were discarded.

4.8.2 fNIRS features screening across patient groups

To further refine the feature set, an additional statistical screening was performed on the fNIRS features, comparing patients belonging to the two different groups (PD-FoG vs PD-noFoG).

For each feature, a two-sample t-test was computed across all epochs belonging exclusively to either group. This comparison was performed independently of task condition and cognitive load (ST/DT), since the aim was not to assess task-related effects but to identify features that exhibited no significant differences between the two patient populations.

A Bonferroni correction was applied to account for multiple comparisons between the two subgroups, and features with Bonferroni corrected p-values greater than 0.05 were discarded from the features set.

4.8.3 Feature correlation and redundancy analysis

The resulting dataset was then used for evaluate features inter-correlations, separately for each modality (fNIRS, sEMG, IMU). Highly correlated features, reflecting redundant information, were identified through pairwise correlation analysis and selectively removed to avoid collinearity in subsequent modeling steps.

This modality-wise approach was chosen to preserve complementary information across sensor types while reducing internal redundancy within each feature group. The combination of statistical relevance and correlation-based filtering resulted in a non-redundant feature set optimized for multimodal classification.

4.9 Machine Learning

4.9.1 Data partitioning and normalization

A LOPO cross validation strategy was adopted to evaluate generalization across subjects.

For the binary task, labels were collapsed to FoG vs noFoG, where the noFoG class was composed by turn and walk epochs. For the three-class task, labels were FoG, preFoG and noFoG.

Training folds were balanced using a custom partitioner: given n FoG episodes in the training fold, noFoG class was composed by $n/2$ walk epochs and $n/2$ turn segments to match FoG counts, selecting from the epochs that most overlapped walk/turn events, while the left-out subject formed the validation fold. Also, a permutation was performed before the selection, in order to avoid selecting most overlapping epochs that belonged all to the same walk/turn events.

Feature values were min-max scaled; feature selection and model fitting were performed within each training fold and validated on epochs of the held-out subject.

4.9.2 Features Selection and Classification

4.9.2.1 Binary classification (FoG vs noFoG)

The first classification task aimed to discriminate between FoG and noFoG epochs. For this purpose, different combinations of feature selection strategies and classifiers were tested:

- SVM classifier was used in combination with mRMR algorithm, which identifies the subset of features that maximize class separability while minimizing inter-feature correlation.
- RF, with feature importance derived from the Out-of-Bag (OOB) permutation error, and the model was retrained using only the top-ranked features.
- kNN classifier was built using the top-ranked features obtained by the ReliefF algorithm.
- LASSO logistic regression, which performs embedded feature selection as part of its optimization process.

For all models except LASSO regression, the number of retained features was optimized through an iterative procedure, in which the top *n* ranked features (with *n* ranging from 10 to the total number in steps of 10) were progressively selected. Model performance was then evaluated for each subset to identify both the optimal configuration and the trend of accuracy as a function of feature count.

Performance metrics were computed on the held-out subject for each fold and then averaged across patients to obtain global estimates.

4.9.2.2 Multiclass classification (FoG vs preFoG vs noFoG)

The second task extended the binary problem to a three-class classification, introducing the preFoG condition to capture transitional patterns preceding freezing episodes. Feature selection and training strategies mirrored those of the binary task:

- For the SVM, mRMR was applied prior to training, and a linear multi-class Error-Correcting Output Codes (ECOC) scheme was used for classification.
- RF again exploited the OOB importance criterion to rank predictors and was retrained on the most informative subset.
- The kNN classifier relied on ReliefF feature weighting to select the most discriminative variables.
- Finally, a Gradient Boosting ensemble (AdaBoostM2) was implemented, incorporating a cost matrix that penalized FoG misclassifications to improve sensitivity toward rare events.

For the three-class classification task, the same feature tuning strategy was applied. The number of retained features was iteratively varied by selecting the top n ranked predictors, with n ranging from 10 to the total available features in increments of 10.

4.9.3 Performance evaluation

Model performance was primarily quantified using balanced accuracy, selected as the main evaluation metric for both the binary and multiclass classification problems due to its robustness to class imbalance.

For the binary problem, balanced accuracy was computed for each fold of the LOPO cross-validation scheme and used as the principal indicator of the model's ability to discriminate FoG from noFoG epochs. For the three-class problem, overall model performance was again summarized through balanced accuracy, and the model achieving the highest mean balanced accuracy across LOPO folds for its optimal number of retained features was identified as the best performing classifier and was used to subsequent analysis.

For this model, a more detailed characterization of its classification behavior was obtained through per-class evaluation. Specifically, precision, recall, specificity, and F1-score were extracted for each of the three classes (noFoG, preFoG, FoG), providing a per-class description of the model's strengths and weaknesses.

In addition, the pairwise misclassification rates were computed to quantify how frequently each class was confused with the others, offering insight into systematic error patterns, such as whether preFoG was more often mistaken for noFoG or FoG, and allowing for a deeper understanding of model behavior.

To further evaluate the specificity of the trained models, an additional validation step was performed using data from the PD-noFoG cohort. All epochs from these patients were processed using the classifiers trained during LOPO (without retraining), and the resulting predictions were compared against the expected noFoG label. In this context, a high specificity would indicate that the model successfully distinguishes true FoG-related patterns from normal gait or turning dynamics, avoiding false positive detections in patients who never exhibit freezing.

4.9.4 Features relevance and model interpretability

After identifying the best-performing classifier, the subsequent analyses focused on estimating the relative importance of individual predictors. For the selected model, each LOPO fold provided an ordered list of features, ranked by the associated features selection algorithm according to their contribution to the classification task.

To obtain a fold-independent importance estimate, these rankings were aggregated into a single global score. For each feature, its rank position in every fold was stored in a rank matrix and the mean rank across folds was computed. This quantity was then converted into an intuitive importance measure by inverting the scale: the maximum mean rank across all features was taken as reference, and an importance score was defined as:

$$\text{score} = \max(\text{mean}R\text{ank}) - \text{mean}R\text{ank}$$

In this way, features that consistently appeared at the top of the ranking across folds obtained the highest scores, whereas features that were systematically relegated to the bottom of the lists received scores close to zero. Sorting these scores in descending order yielded a global ranking of all predictors, which was then used as the basis for subsequent analyses.

Starting from this ranking, cumulative scores were computed to summarize importance at different levels of aggregation. Scores were grouped both by sensing modality (IMU, EMG, fNIRS), to quantify their relative contribution to the classification problem, and, within each modality, they were aggregated across individual sensors (for IMUs) and muscles (for EMG) to assess which anatomical locations provided the most informative signals.

To statistically assess whether feature importance differed across groups, a non-parametric Kruskal-Wallis test was applied to the importance scores. When the omnibus test was significant ($p < 0.05$), post-hoc pairwise comparisons were performed using Tukey-type multiple comparisons on the Kruskal-Wallis ranks. Pairwise p-values were then corrected using a Bonferroni adjustment, and only comparisons surviving the corrected threshold ($\alpha = 0.05$) were interpreted as significant.

5 Results

5.1 Events Definition

5.1.1 Step detection

This section reports the results of the events definition process, starting with the step detection procedure whose results are represented in the figure below.

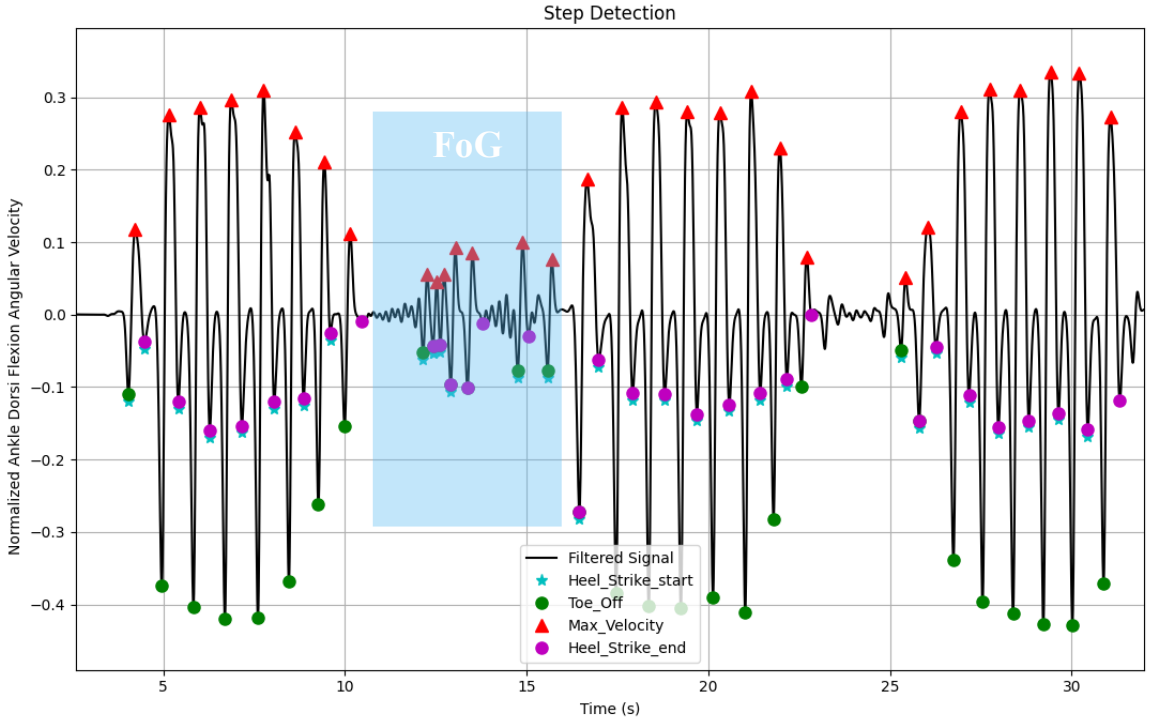

Figure 5.1 Example of Step Detection inside and outside FoG episodes

The plot shows the filtered dorsiflexion angular velocity signal (black curve) together with the gait events automatically identified by the detection algorithm. Start events are marked in light blue, heel-strike end events in magenta, toe-off events in green, and the peak angular velocities associated with each step cycle in red.

A FoG episode is highlighted in the central portion of the figure (blue shaded area), where the periodic structure of the signal is disrupted, resulting in irregular or absent gait events. This illustrates how the step-detection procedure captures both normal gait dynamics and their breakdown during freezing.

5.1.2 Turn identification

In the figure below is represented the absolute value of the angular velocity recorded from the lumbar sensor, with the identified turn events represented by blue patches

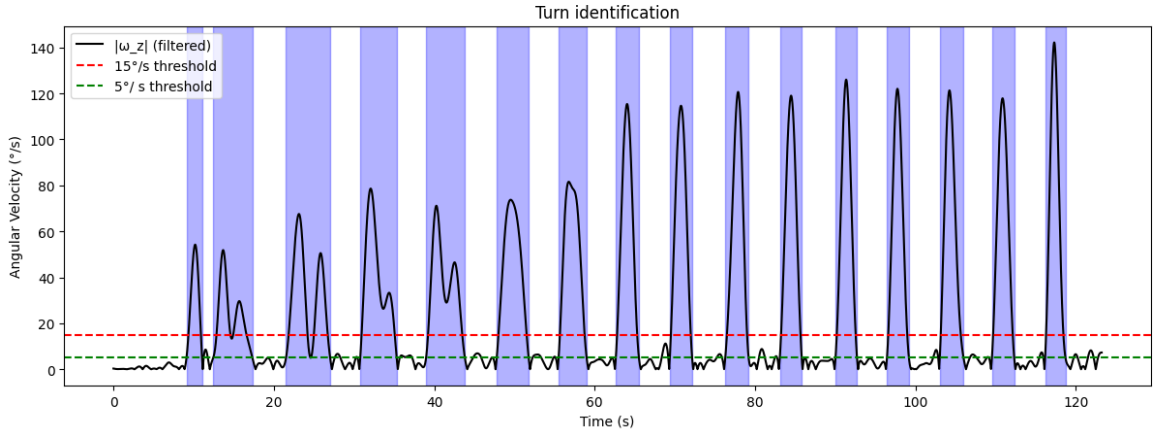

Figure 5.2 Turn Identification using double threshold approach

After this first step, all the time samples not labeled with turn were associated with "walk" label, since in our tasks configuration patients could either walk or make 180° turns.

Then the step realignment procedure was performed, resulting in the following figures, which represent the orientation angle around the vertical axis with the turn (in blue) and walk (in green) events overlapped.

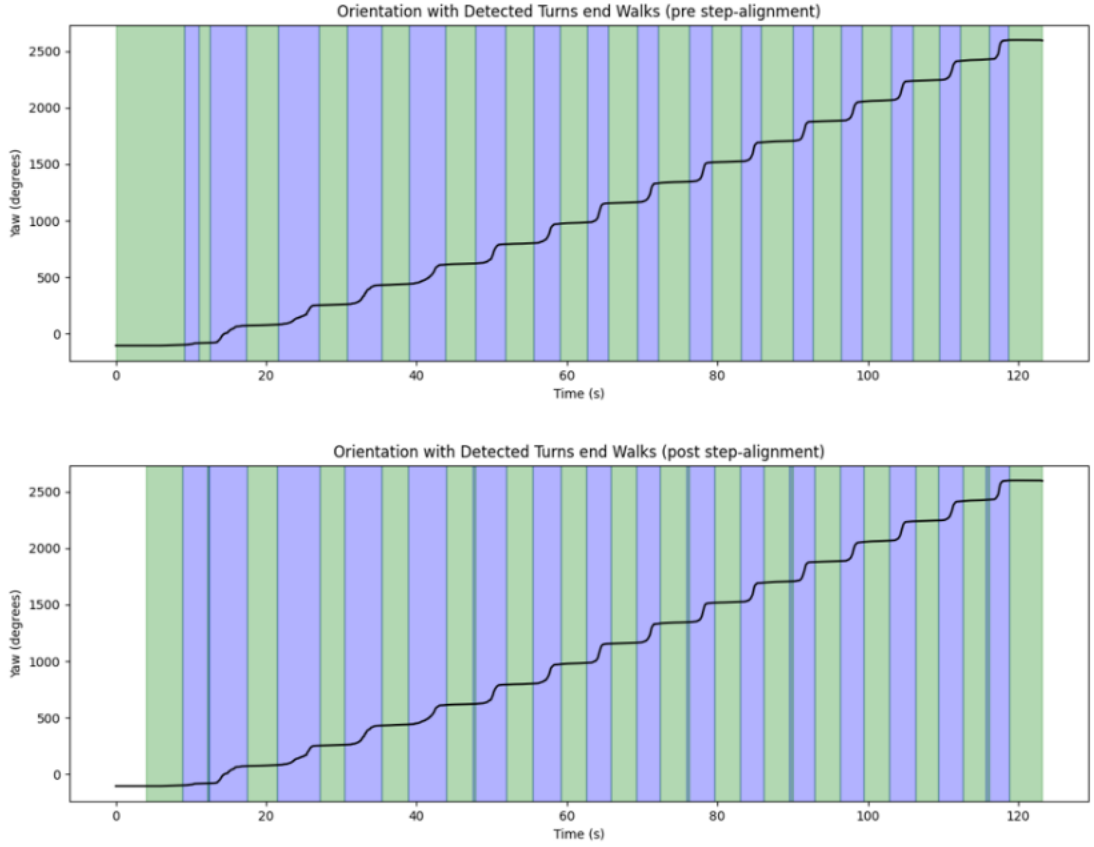

Figure 5.3 Representation of the detected gait events (walk in green, turn in blue) pre and post alignment with step events

5.1.3 FoG and preFoG definition

Consequently, manual annotation produced by the two raters were added, resolving overlap by giving priority to FoG and preFoG events, and converting "turn" events overlapping "turn_alterated" events in "turn_alterated". This procedure yielded the final events definition results, shown in the figure below

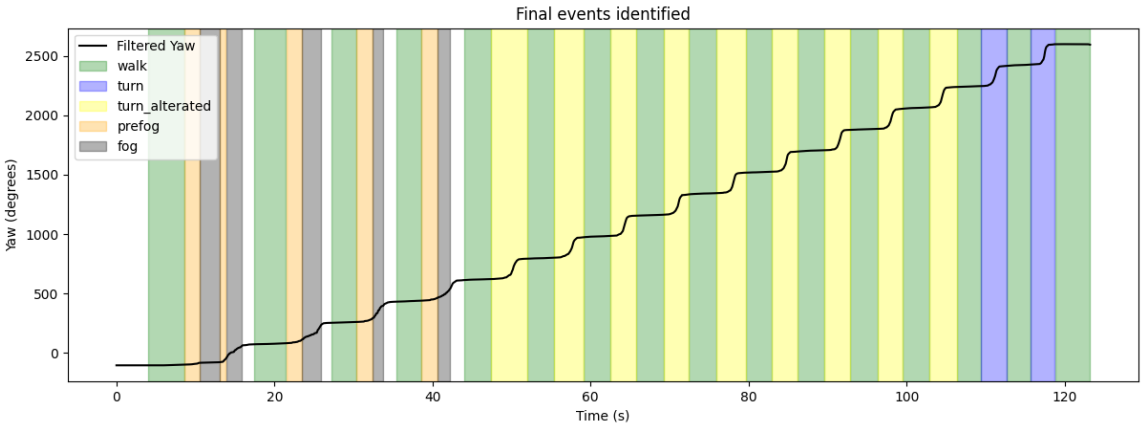

Figure 5.4 Events Definition final output

5.2 Cortical activation patterns from β-maps

This section reports the results of the statistical analyses performed on the β activation maps obtained from the GLM analysis applied to fNIRS data. Each β-map represents the cortical activation associated with a specific behavioral condition (walk, turn, preFoG, FoG), and has been analyzed both at single-subject and group level by computing contrasts to identify significant differences between conditions.

5.2.1 Single-subject analysis

Individual β-maps were first inspected to evaluate the spatial patterns of cortical activation associated with each condition.

Figure 5.5 shows an example of the activation pattern during FoG episodes (single task condition) in one representative subject. In this case, FoG is associated with increased hemodynamic activity over the right prefrontal cortex, supplementary motor areas and left postcentral regions, illustrating the cortical recruitment accompanying freezing events in this patient.

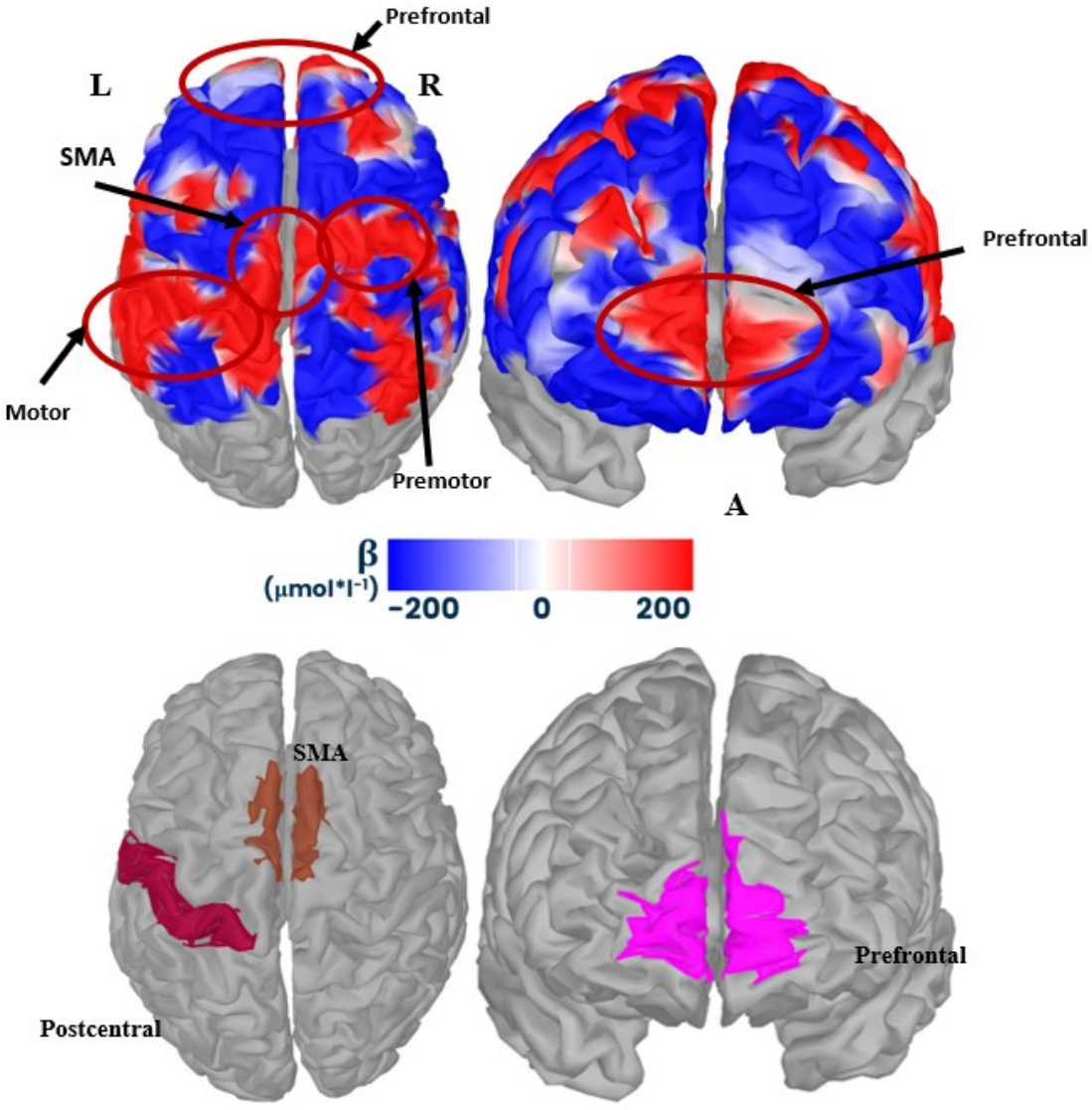

Figure 5.5 Example of single-subject β activation map during FoG. Left and right are indicated as "L" and "R" respectively, Anterior view is indicated as "A"

Subsequent within-subject contrasts were computed to highlight condition-dependent differences in activation. The following contrasts were evaluated:

1) FoG vs Walk, to identify cortical regions specifically recruited during freezing compared to steady gait.
2) FoG vs Turn, to distinguish freezing-related activation from turning-related demands.
3) FoG vs preFoG, to capture cortical transitions preceding freezing onset.
4) Turn vs Walk, to examine motor control adaptation during turning.
5) preFoG vs Walk, to characterize anticipatory activation patterns.

Figure 5.6 shows the resulting contrast maps for single task conditions, while Figure 5.7 reports the corresponding contrast for dual task conditions. Each contrast was computed at the voxel level within the subject's cortical space, producing β-difference maps, in which red colors indicate stronger activation in the first condition of the contrast, whereas blue colors indicate stronger activation in the second.

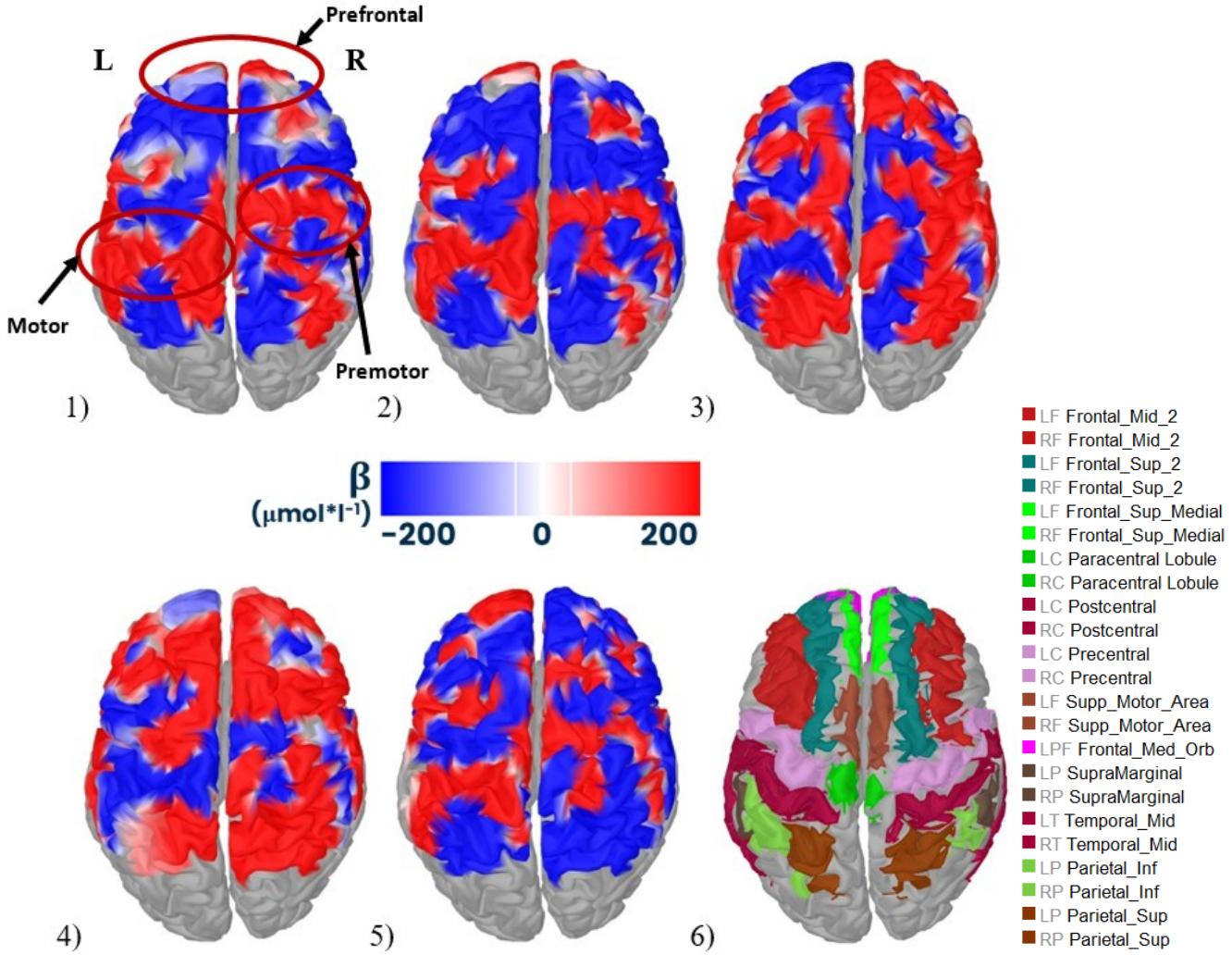

Figure 5.6 Representative single-subject contrast maps showing cortical activation differences between conditions in single task. Legend: 1) FoG vs Walk, 2) FoG vs Turn, 3) FoG vs preFoG, 4) Turn vs Walk, 5) PreFoG vs Walk, 6) AAL3 ROIs.

Under the single-task condition, all contrasts revealed widespread differences in cortical activation across the bilateral prefrontal and motor regions. The FoG vs Walk and FoG vs Turn contrasts revealed large, spatially diffuse activation differences spanning the prefrontal cortex as well as bilateral premotor and motor regions. The FoG vs preFoG comparison showed an

even more extensive enhancement during FoG, with increased activation also emerging in temporal and parietal areas. In the Turn vs Walk contrast, a clear elevation of activity was observed in prefrontal, premotor, and motor regions, indicating a higher engagement of frontal regions during turning. The preFoG vs Walk map exhibited only mild and spatially limited differences, without marked focal patterns.

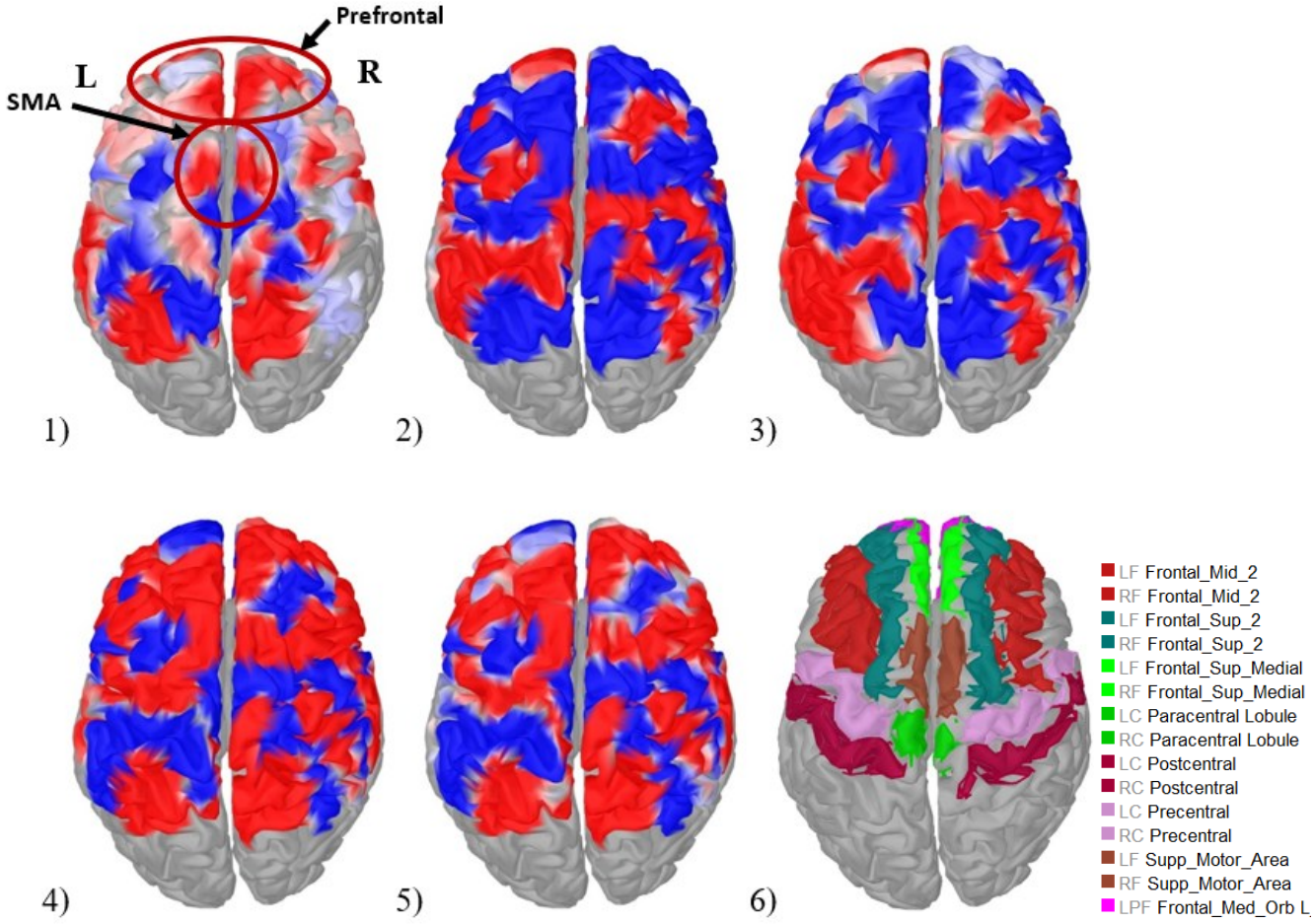

Figure 5.7 Representative single-subject contrast maps showing cortical activation differences between conditions in dual task. Legend: 1) FoG vs Walk, 2) FoG vs Turn, 3) FoG vs preFoG, 4) Turn vs Walk, 5) PreFoG vs Walk, 6) AAL3 ROIs.

Under the dual-task condition, the FoG vs Walk contrast revealed a prominent increase in activation across frontal and prefrontal regions, extending into the supplementary motor area, while a relative deactivation emerged over the primary motor cortex. The FoG vs Turn and FoG vs preFoG maps showed localized patterns, with differences mainly confined to motor and premotor territories and only limited involvement of anterior frontal regions. A broader modulation of cortical activity appeared in the Turn vs Walk contrast, characterized by spatially widespread clusters distributed across both frontal and motor areas. A similar diffuse pattern was observed in the preFoG vs Walk comparison, with extended regions showing condition-related variations but without a clear focal organization.

5.2.2 Group-level analysis

Group-level comparisons were conducted to evaluate consistency of activation patterns across participants. The results are presented in two parts:

1. within-group paired comparisons among conditions in the PD-FoG cohort
2. between-group analyses comparing PD-FoG and PD-noFoG participants.

5.2.2.1 Within-group (PD-FoG)

Paired t-tests were performed across subjects of the FoG group for the same condition contrasts examined at the single-subject level, in order to assess whether the activation patterns observed at the individual level were consistently expressed across patients

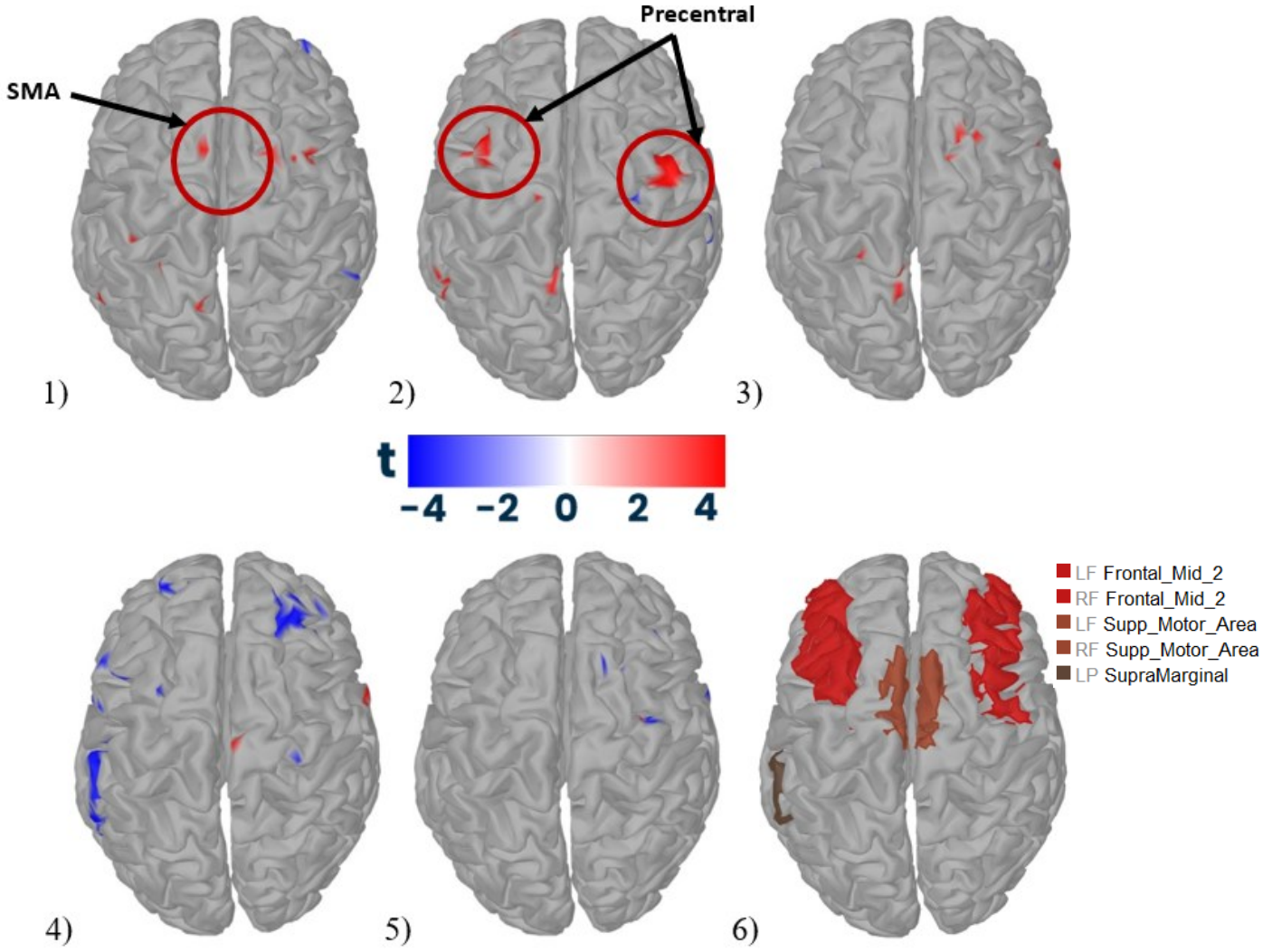

Figure 5.8 Group-level β activation contrasts within the PD-FoG cohort, single task events. Maps represent t-statistics overlaid on the cortical surface (threshold p < 0.05, uncorrected). Legend: 1) FoG vs Walk, 2) FoG vs Turn, 3) FoG vs preFoG, 4) Turn vs Walk, 5) PreFoG vs Walk, 6) AAL3 ROIs that resulted significant

Paired comparisons revealed only focal and spatially circumscribed significant activations across the examined contrasts ($p < 0.05$, uncorrected). In the FoG vs Walk map, small clusters of increased activation emerged in the SMA. The FoG vs Turn contrast showed a similarly limited pattern, with a few premotor and motor clusters displaying significant activation. The FoG vs preFoG comparison yielded sparse premotor clusters, mainly confined to the right hemisphere.

A slightly different configuration appeared in the Turn vs Walk contrast, where a small region of decreased activation was observed over the superior frontal cortex. Finally, the preFoG vs Walk contrast showed only a few scattered significant points, without a clearly organized spatial distribution.

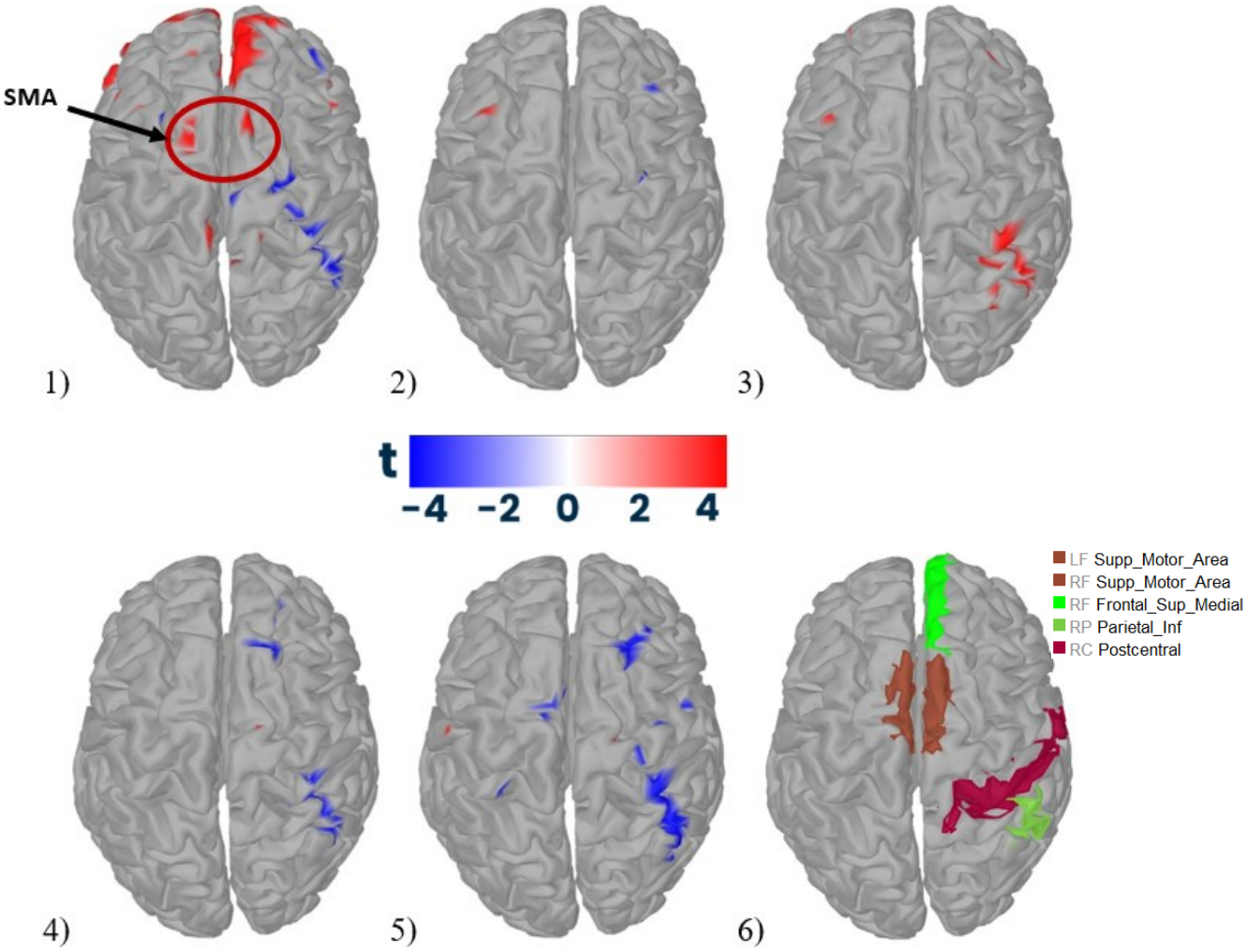

Figure 5.9 Group-level β activation contrasts within the PD-FoG cohort, dual task events. Maps represent t-statistics overlaid on the cortical surface (threshold $p < 0.05$, uncorrected). Legend: 1) FoG vs Walk, 2) FoG vs Turn, 3) FoG vs preFoG, 4) Turn vs Walk, 5) PreFoG vs Walk, 6) AAL3 ROIs that resulted significant

In the dual-task condition, group-level paired t-tests revealed a small number of significant but spatially confined clusters. The FoG vs Walk contrast showed the most prominent effect, with a clear increase in activation over frontal regions and a small focal cluster in the supplementary motor area, indicating stronger engagement of these areas during freezing episodes compared to regular walking. In the FoG vs preFoG comparison, a distinct parietal cluster exhibited higher activation in FoG than in preFoG.

For the remaining contrasts, significant effects were more limited. The Turn vs Walk and preFoG vs Walk maps mainly displayed small areas of decreased activation, predominantly located in the right premotor cortex and in right parietal regions.

Overall, these maps present small, localized clusters of significance, consistent with the modest sample size available for the paired analysis. Given the limited statistical power, the emergence of only focal effects is expected and aligns with the methodological constraints of the dataset.

5.2.2.2 Between-group (PD-FoG vs PD-noFoG)

To explore group differences in cortical activation, two-sample t-tests were performed between the PD-FoG and PD-noFoG cohorts for the conditions common to both groups:

1) Walk single task
2) Turn single task
3) Walk dual task
4) Turn dual task

This analysis aimed to assess whether patients experiencing freezing episodes exhibit distinct cortical dynamics even during non-freezing motor conditions.

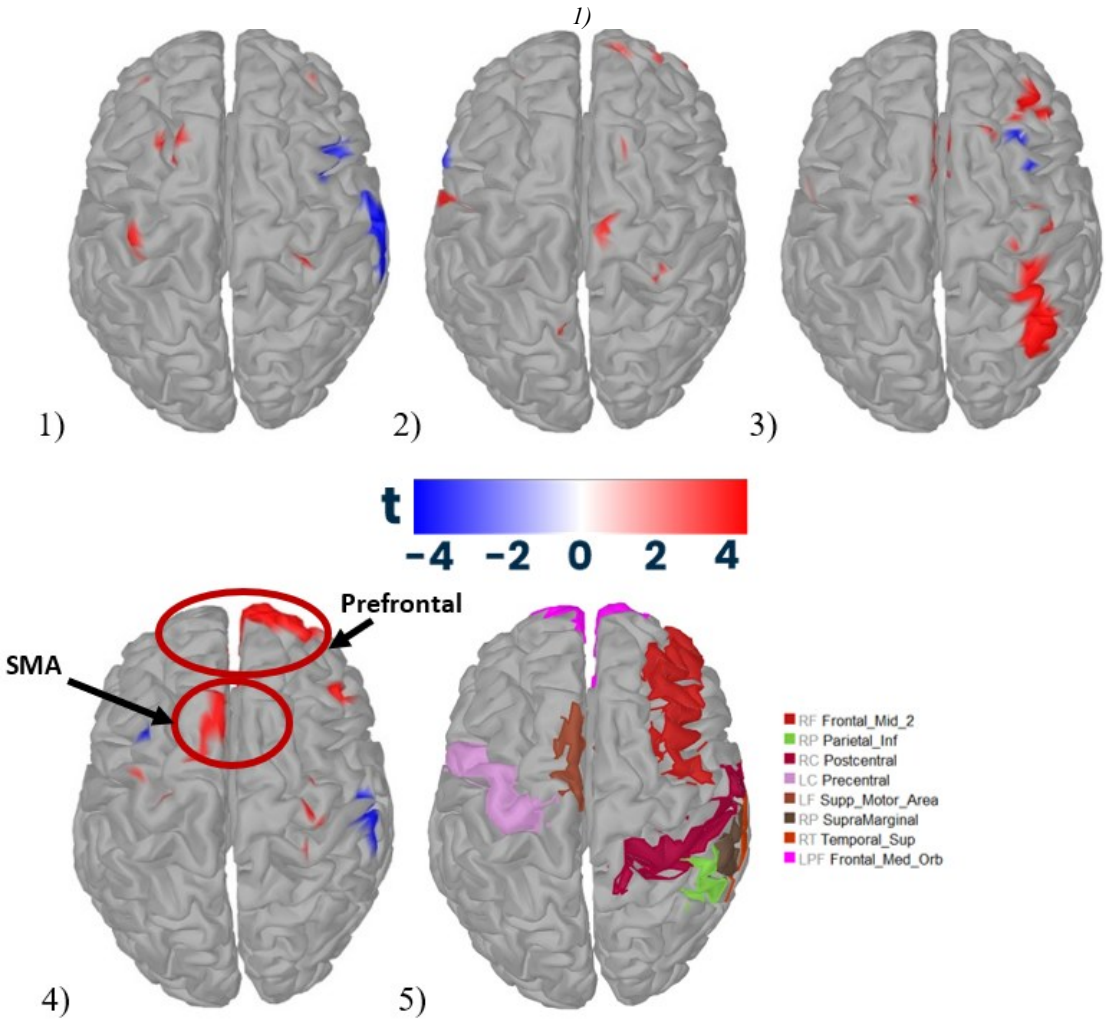

Figure 5.10 Between-group comparison of β activation maps for walk and turn conditions. Warm colors indicate higher activation in the PD-FoG group, cool colors indicate higher activation in PD-noFoG participants. Subfigure number 5 shows AAL3 ROIs that resulted significant.

Group-level comparisons between PD-FoG and PD-noFoG participants revealed a limited number of significant clusters. In the Walk-ST contrast, a small cluster of higher activation in the PD-noFoG group appeared in the right temporal region, together with a few isolated small clusters in the left hemisphere.

In the Turn-ST contrast, scattered small clusters emerged, predominantly located in the right hemisphere, with the bigger one located between the SMA and primary motor cortex.

The Walk-DT comparison showed a focal area of significantly higher activation in the PD-FoG group, localized in the right parietal inferior area, while no extended bilateral effects were observed.

Finally, in the Turn-DT contrast, the largest cluster among the four conditions appeared over the right frontal cortex, where PD-FoG patients exhibited consistently higher activation than PD-noFoG individuals. Another relatively big cluster of grater activation in PD-FoG patients was found in the SMA, while additional smaller clusters were present but remained spatially sparse.

5.3 Outlier identification and removal

After the feature-extraction pipeline, which produced a high-dimensional dataset, a general screening procedure was applied to obtain a more compact and cleaner feature set, ensuring higher data quality and reducing redundancy before the subsequent analyses.

The outlier identification procedure resulted in the removal of 17.8% of the total number of epochs, with detailed information on the specific reasons for removal, including LOF flags and 10% rule violations for each modality, reported in the following table.

Patient	Epochs number	EMG LOF	IMU LOF	NIRS LOF	EMG 10pct	IMU 10pct	NIRS 10pct	Union	Kept epochs number	Percentage removed
PD_001	2789	132	91	385	8	20	570	978	1811	35%
PD_003	3680	101	149	106	0	13	0	335	3345	9.1%
PD_004	3421	134	154	191	0	207	3	604	2817	17.7%
PD_005	2952	166	217	13	0	28	0	369	2583	12.5%
All	12842	533	611	695	8	268	573	2286	10556	17.8%

Table 5.1 Outlier identification results

5.4 Features dimensionality reduction

5.4.1 Statistical screening

The first filtering step removed features that did not show statistically significant differences across the labeled gait events. As summarized in *Table 5.2*, this procedure eliminated a limited portion of the original feature set. Overall, 8.3% of IMU features, 4.6% of EMG features, and 5.4% of fNIRS features were discarded at this stage.

Modality	Number of features pre removal	Number of retained features	Percentage removed
IMU	168	154	8.3%
EMG	108	103	4.6%
NIRS	130	123	5.4%

Table 5.2 Results of the statistical screening procedure

5.4.2 fNIRS features screening across patient groups

Because cortical activation patterns are known to differ between FoG and non-FoG patients, an additional statistical comparison was carried out exclusively on fNIRS features. Features that did not show significant differences in group comparisons between PD-FoG and PD-noFoG participants were removed, resulting in the exclusion of 26 features, corresponding to 21.1% of the fNIRS feature set.

5.4.3 Feature correlation and redundancy analysis

To evaluate redundancy within the retained features, correlation matrices were computed separately for IMU (a), EMG (b), and fNIRS (c).

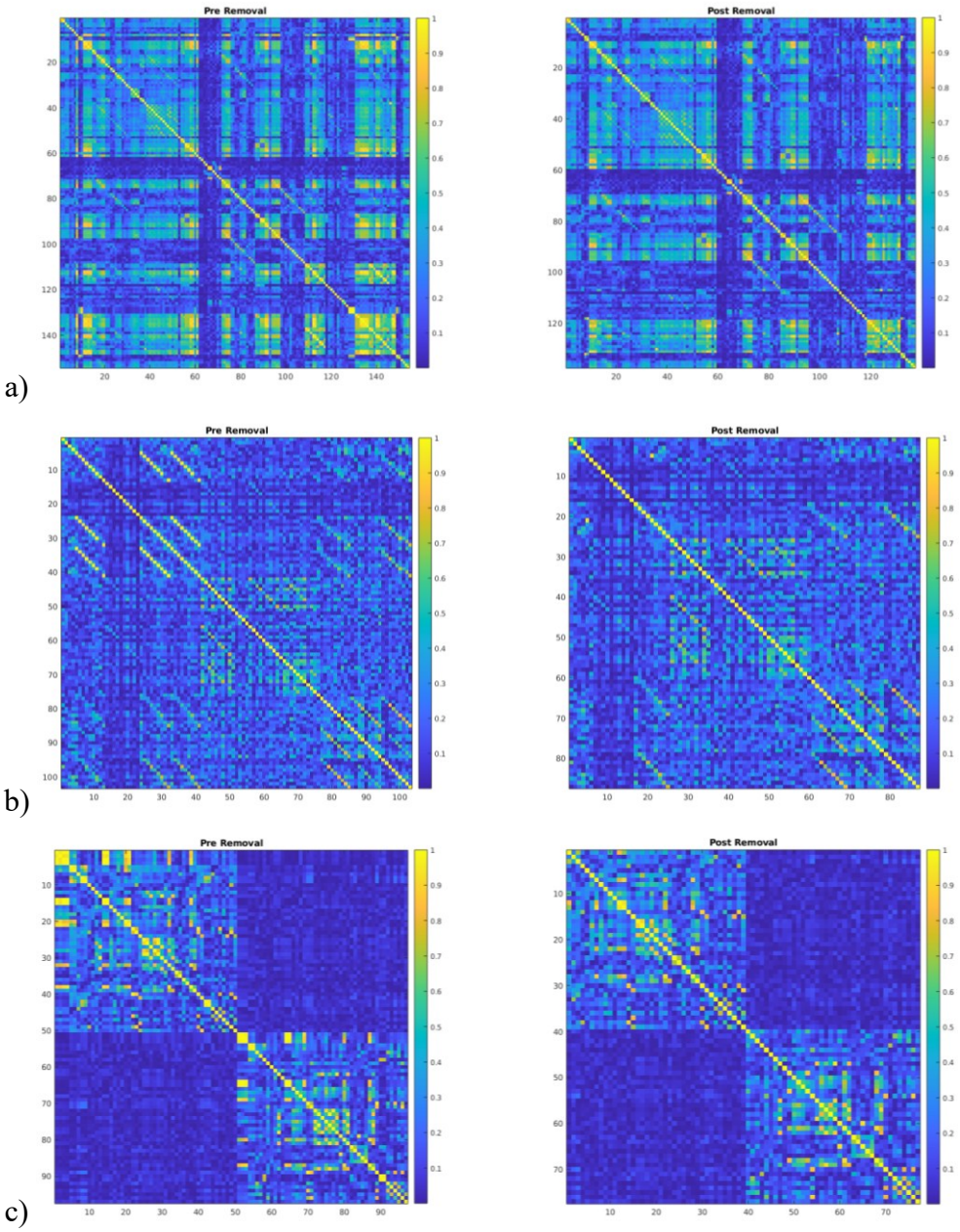

Figure 5.11 Correlation plots pre (left) and post (right) removal

Modality	# Features pre removal	# Features kept	% Removed
IMU	154	137	11%
EMG	103	87	15.5%
NIRS	97	77	20.6%

Table 5.3 Results of the correlation analysis procedure

The correlation maps show that the initial feature sets exhibited several dense blocks of highly correlated descriptors, especially within NIRS-derived measures and within muscles of the same anatomical group for EMG.

5.5 Machine Learning results

This section presents the results of the classification analyses performed to automatically identify FoG episodes based on multimodal features extracted from fNIRS, EMG, and IMU signals, both for two-class problem (FoG vs noFoG) and three-class problem (FoG vs noFoG vs preFoG).

5.5.1 Binary classification (FoG vs noFoG)

In the binary problem, classification performance was evaluated on the epochs of the held-out patient through balanced accuracy, chosen to account for the unbalancing of the validation set (for each patient noFoG class is always prevalent).

5.5.1.1 Feature number tuning

For the three classifiers that included a feature selection procedure providing an importance-based ranking, a feature number tuning was performed to evaluate the optimum number for each model.

Figure 5.12 illustrates how the mean balanced accuracy across folds varied as a function of the number of selected features for each classifier. Among the evaluated classifiers, the Random Forest showed the highest and most stable accuracy across the full feature range, whereas the SVM exhibited greater variability related to dimensionality, with performance peaking with 100 features. The optimal number of features was chosen separately for each model by finding the maximum average balanced accuracy across folds and was therefore used in the subsequent analyses.

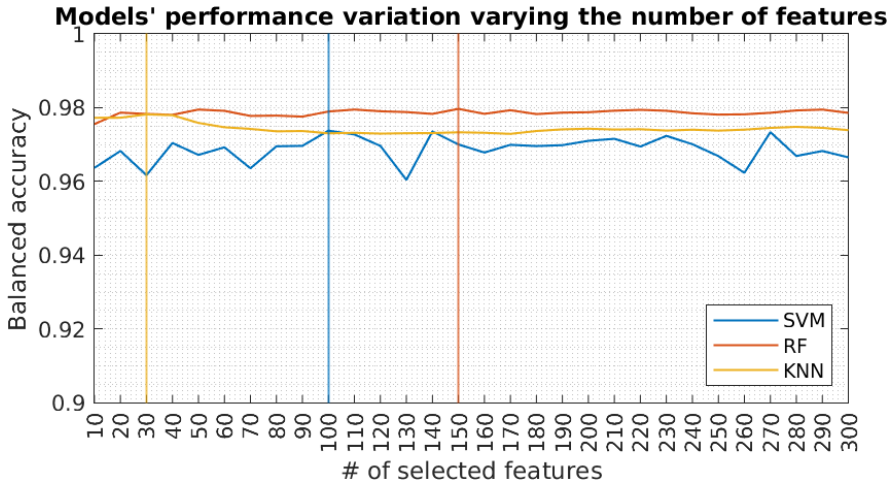

Figure 5.12 Variation of balanced accuracy as a function of the number of selected features for each classifier (2-class problem). Vertical lines indicate the optimal feature count for each model.

	SVM	RF	kNN
Mean	96%	98%	97%
Standard Deviation	0.4%	0.1%	0.2%

Table 5.4 Mean and Standard deviation of classification performance varying the number of selected features (2-class problem).

5.5.1.2 Validation performance across subjects

Figure 5.13 reports the balanced accuracy obtained for each validation subject within the LOPO cross-validation procedure. Each group of bars represents a single fold, where the left-out subject was used as the validation set and the remaining subjects formed the training set.

The results show consistent and very high model performance across folds, with balanced accuracy values above 90% for all classifiers in every subject.

Inter-subject variability was limited (2-3%), suggesting that the models generalize well to unseen patients despite the heterogeneity in individual patterns.

The Random Forest and kNN models demonstrated the highest mean performance across folds (98%), while SVM exhibited slightly larger fluctuations (3.1% standard deviation).

The corresponding numerical values for each model and validation subject are summarized in *Table 5.5*, which provides the exact balanced accuracy scores shown graphically in *Figure 5.13*.

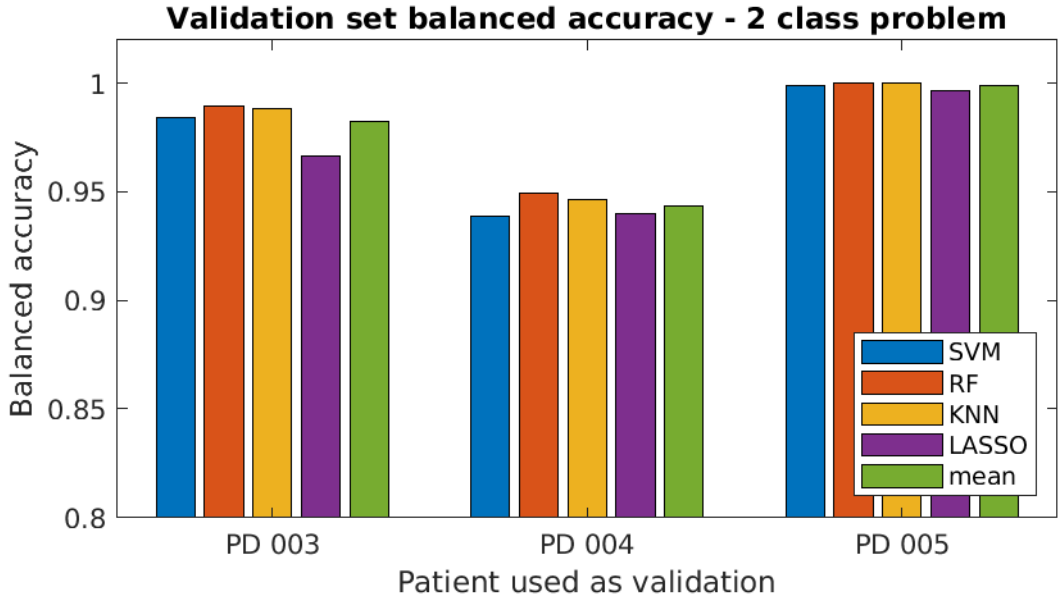

Figure 5.13 Balanced accuracy for each subject used as validation fold in the LOPO cross-validation (2-class problem). Each color corresponds to a different classifier.

	SVM	RF	KNN	LASSO	Mean	Standard Deviation
PD_003	98%	99%	99%	97%	98%	1%
PD_004	94%	95%	94%	94%	94%	0.5%
PD_005	99%	99%	99%	99%	99%	0.1%
Mean	97%	98%	98%	97%		
Standard Deviation	3.1%	2.7%	2.8%	2.8%		

Table 5.5 Balanced accuracy values per subject and model, corresponding to the bars shown in Figure 5.13.

5.5.1.3 Overall model comparison

The overall comparison of classifiers, averaged across folds, is summarized in *Figure 5.14*. All models achieved high balanced accuracy, with mean values exceeding 0.95.

The Random Forest and kNN models yielded the best overall performance, both in terms of mean accuracy and stability, as reflected by the smaller standard deviation across folds. The SVM achieved comparable performance, though with slightly larger variability, while the LASSO model performed relatively worse.

Overall, the results indicate that ensemble and neighborhood-based methods provided the most robust discrimination between FoG and noFoG epochs in this dataset.

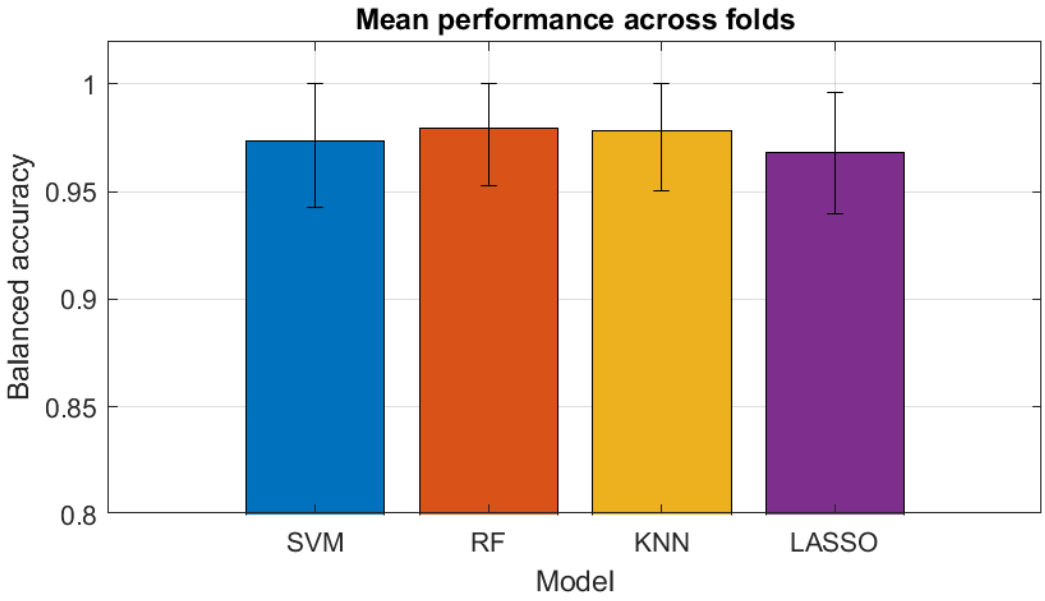

Figure 5.14 Mean balanced accuracy (± standard deviation) across LOPO folds for each classifier.

5.5.2 Multiclass classification (FoG vs preFoG vs noFoG)

In the three class classification problem, classification performance was also evaluated on the epochs of the held-out patient computing balanced accuracy.

5.5.2.1 Feature number tuning

Figure 5.15 shows the variation of the balanced accuracy as a function of the number of selected features for each classifier in the three-class problem.

Similarly to the binary case, the top ranked features were iteratively selected (with the number ranging from 10 to the total number in steps of 10), and performance was evaluated by averaging each LOPO fold performance.

As illustrated, the kNN classifier showed the best overall performance, showing a stable accuracy plateau above 80% once more than 70 features were included, and achieving the greatest balanced accuracy value using 290 features.

The Random Forest and Gradient Boosting models followed closely, exhibiting moderate sensitivity to the number of features, while SVM reached lower accuracy levels and higher variability, lowering its performance when increasing the number of features.

The optimal feature count, corresponding to the highest average balanced accuracy for each model, was subsequently used in the following analyses.

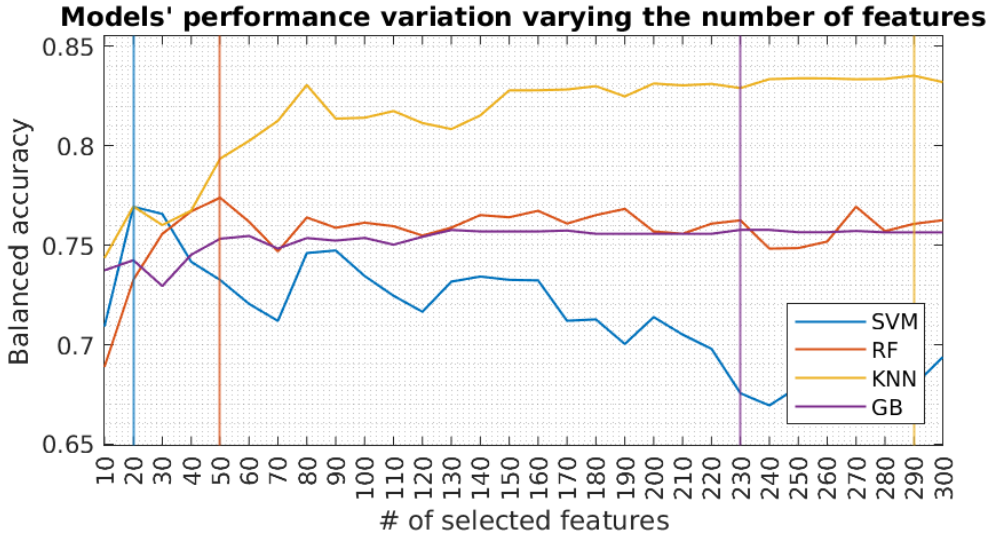

Figure 5.15 Balanced accuracy as a function of the number of selected features for each classifier (3-class problem). Vertical lines indicate the feature count that provided the best performance for each model.

	SVM	RF	kNN	GB
Mean	72%	76%	82%	75%
Standard Deviation	2.6%	1.5%	2.5%	0.6%

Table 5.6 Mean and Standard deviation of classification performance varying the number of selected features (3-class problem

5.5.2.2 Validation performance across subjects

Figure 5.16 summarizes the balanced accuracy obtained for each subject used as validation in the LOPO cross-validation. Each group of bars represents one fold, corresponding to a different patient excluded from the training set and used as validation.

The results show overall good classification performance across subjects, although slightly lower than in the binary problem, as expected given the additional difficulty of discriminating the preFoG state.

However, clear inter-subject variability in FoG expression emerges from the results. Subject PD_003, in particular, acted as a strong validation case, since models trained on the remaining participants transferred well to this subject, yet proved to be a weak training case. This imbalance reflects substantial heterogeneity in how FoG manifests across individuals and likely contributes to the reduced consistency observed in the three-class scenario. Such variability underscores the challenge of learning preFoG-specific patterns in a truly subject-independent way.

The kNN classifier yielded the most stable results, maintaining balanced accuracy values around or above 80% for most patients. The SVM and GBT exhibited the worst performance (77-76%), comparable to the RF but with slightly higher dispersion (8.8-9.2% standard deviation against 6.5%).

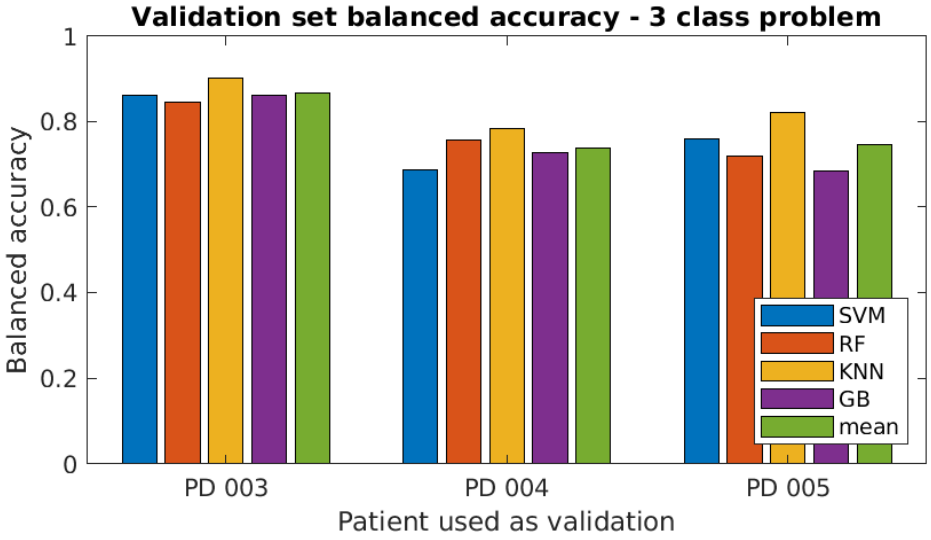

Figure 5.16 Balanced accuracy per subject for the LOPO cross-validation (3-class problem). Each color represents a different classifier

	SVM	RF	KNN	GB	Mean	Standard Deviation
PD_003	86%	85%	90%	86%	87%	2.3%
PD_004	69%	76%	78%	73%	74%	4.2%
PD_005	76%	72%	82%	69%	75%	5.8%
Mean	77%	77%	84%	76%		
Standard Deviation	8.8%	6.5%	5.9%	9.2%		

Table 5.7 Balanced accuracy values per subject and model corresponding to the bars in Figure 5.16

5.5.2.3 Overall model comparison

The overall mean balanced accuracy and standard deviation across LOPO folds is presented in this section. All models demonstrated satisfactory classification performance, with mean accuracies ranging between 75% and 85%.

The kNN classifier achieved the best average performance and the smallest variability across folds (84% ± 5.9%), confirming its robustness in handling the nonlinear separations among the three classes. The Random Forest and Gradient Boosting models achieved similar mean accuracies, showing good generalization and stable behavior.

Conversely, the SVM yielded slightly lower performance, consistent with its limited capacity to capture complex, nonlinear relationships without explicit kernel tuning.

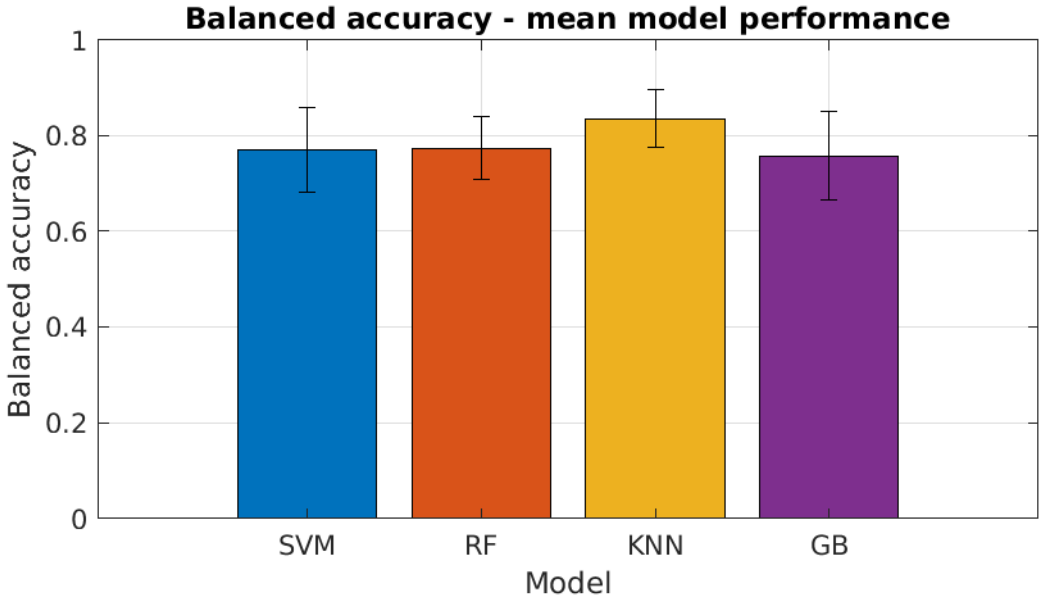

Figure 5.17 Mean balanced accuracy (± standard deviation) across LOPO folds for each classifier (3-class problem).

5.5.2.4 Inter-class performance analysis

To better characterize the classification behavior of the best-performing model (kNN with 290 features), a confusion matrix-based analysis was carried out.

For each LOPO fold, the confusion matrix was computed, normalized by row to represent prediction probabilities, and subsequently averaged across folds to obtain a subject-independent estimate.

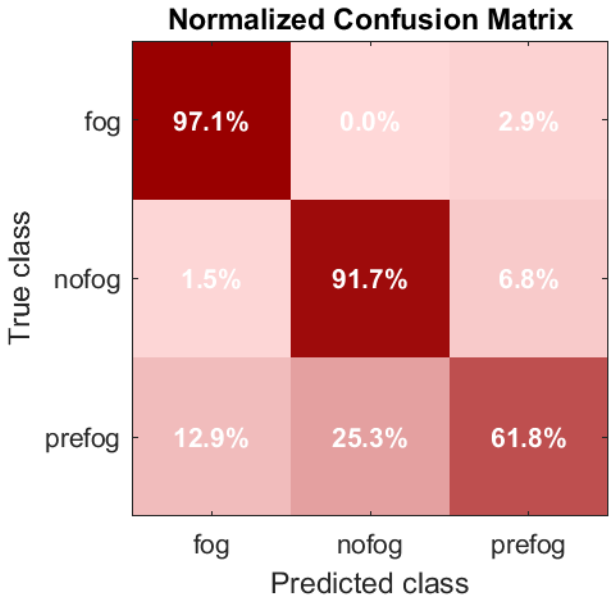

Figure 5.18 Normalized confusion matrix of the kNN classifier (3-class problem), averaged across LOPO folds. Diagonal values indicate correct classifications; off-diagonal values represent inter-class confusions.

From the averaged confusion matrix, the main performance metrics were computed class-wise, to evaluate model's capability of distinguish each class.

Class	Precision	Recall	Specificity	F1-score
FoG	87%	97%	93%	92%
noFoG	78%	92%	87%	85%
preFoG	86%	62%	95%	72%

Table 5.8 Per-class performance metrics derived from the averaged confusion matrix.

As expected, the FoG and noFoG classes achieved the highest recall and precision values, while preFoG showed lower scores, confirming its intermediate and overlapping nature between stable gait and freezing onset. This pattern indicates that the model reliably distinguishes freezing events but partially confuses transitional states with nearby classes.

To further quantify inter-class confusion, pairwise misclassification rates were extracted. These values represent the percentage of epochs from one class that were misclassified as another.

Misclassification	Rate percent
FoG → noFoG	0
FoG → preFoG	2.9
noFoG → FoG	1.5
noFoG → preFoG	6.8
preFoG → FoG	12.9
preFoG → noFoG	25.3

Table 5.9 Pairwise misclassification rates between classes, expressed as percentage of total predictions.

The analysis revealed a pronounced asymmetry, with preFoG → noFoG errors (≈ 25%) being more frequent than preFoG → FoG (≈ 13%), suggesting that early freezing signatures share stronger similarities with gait phases rather than freezing episodes in this specific setup and conditions (2 seconds preFoG window).

5.5.2.5 Model specificity evaluation on PD-noFoG patients

To assess model specificity, best-performing models trained within the LOPO framework were additionally tested on data coming exclusively from the PD-noFoG cohort. For each fold, predictions on these participants were collected, and class proportions were normalized and then averaged across folds, yielding the group-level confusion matrix shown in the figure below.

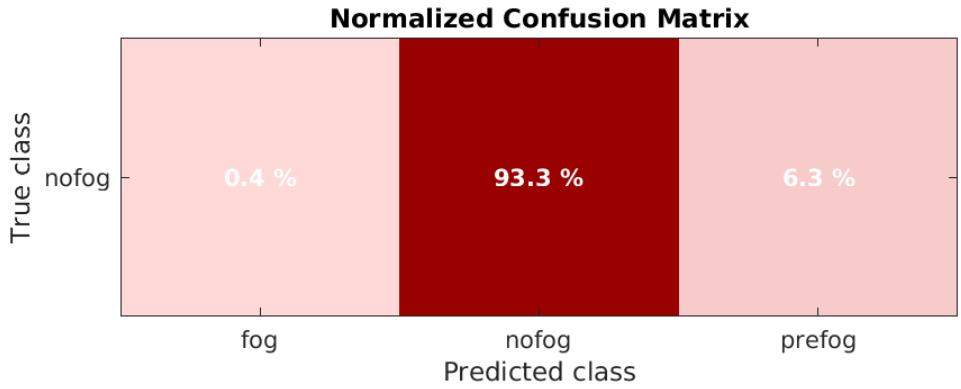

Figure 5.19 Normalized predictions on PD-noFoG cohort

As expected, the classifier assigned the vast majority of epochs from PD-noFoG patients to the noFoG class (93.3%), indicating a high specificity in recognizing non-freezing behavior. Only a very small proportion of epochs were incorrectly labeled as FoG (0.4%), while a limited fraction was classified as preFoG (6.3%).

5.5.2.6 Feature relevance and model interpretability

To gain insight into the decision process of the classifier and identify the most informative predictors, a feature importance analysis was conducted on the best-performing model.

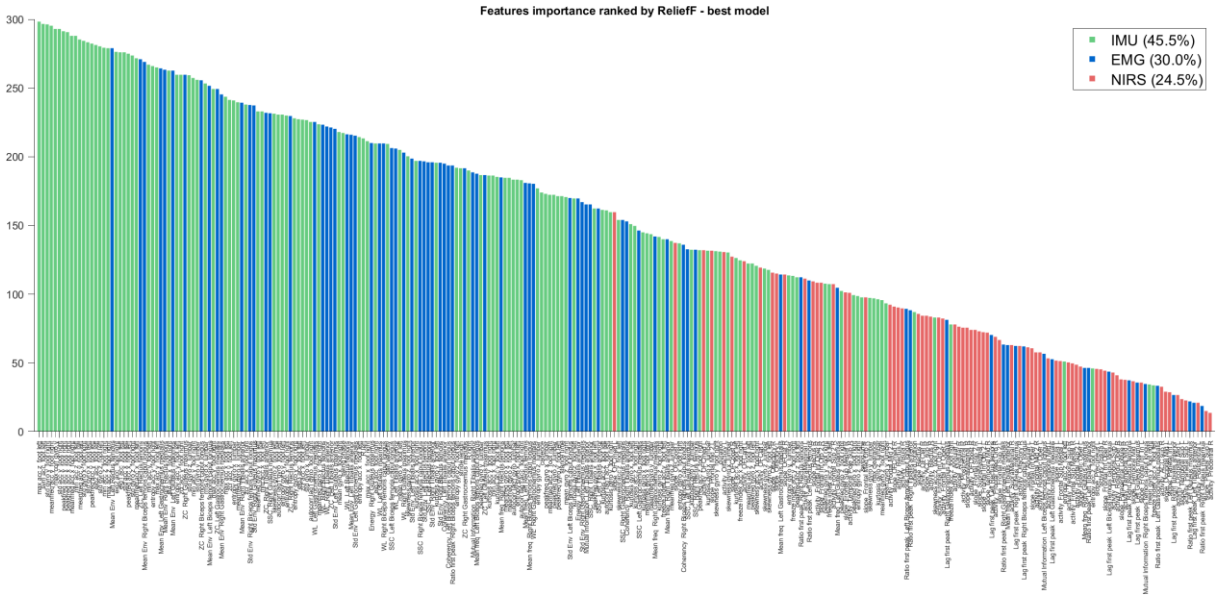

Figure 5.20 Feature importance ranking of the best-performing model (kNN, 3-class problem). Bars represent feature importance, color-coded by modality (green = IMU, blue = EMG, red = fNIRS).

In the bar plot above is illustrated the relative importance of the top-ranked features contributing to the multiclass discrimination. Each bar represents one feature, while colors denote feature modality, green for IMU-derived features, blue for EMG, and red for fNIRS.

The analysis revealed that IMU-based features dominated the upper portion of the ranking, highlighting the central role of gait kinematics and dynamic stability in distinguishing the three conditions.

Although the bar plot in the figure below suggests that cumulative feature importance was not evenly distributed across IMU sensors, with left-foot features showing the highest mean contribution, these differences did not result statistically significant in the analysis.

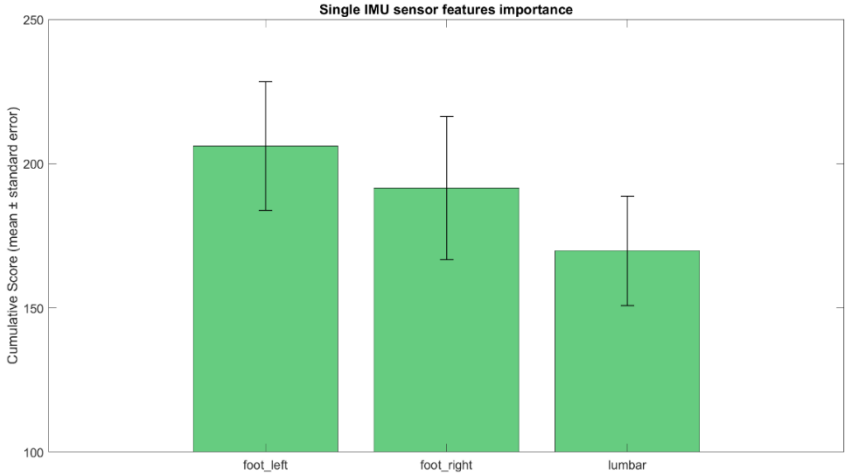

Figure 5.21 Cumulative feature importance (mean ± standard error) aggregated by single IMU sensor

Several EMG features exhibited notable discriminative power, and the aggregated importance scores displayed apparent differences across muscles. As shown in *Figure 5.22*, distal muscles such as the rectus femoris and tibialis anterior tended to show higher average importance

compared with more proximal muscles like the gluteus maximus. However, these differences were not statistically significant after correction for multiple comparisons, resulting in descriptive trends rather than group-wise differences in feature relevance across EMG recording sites.

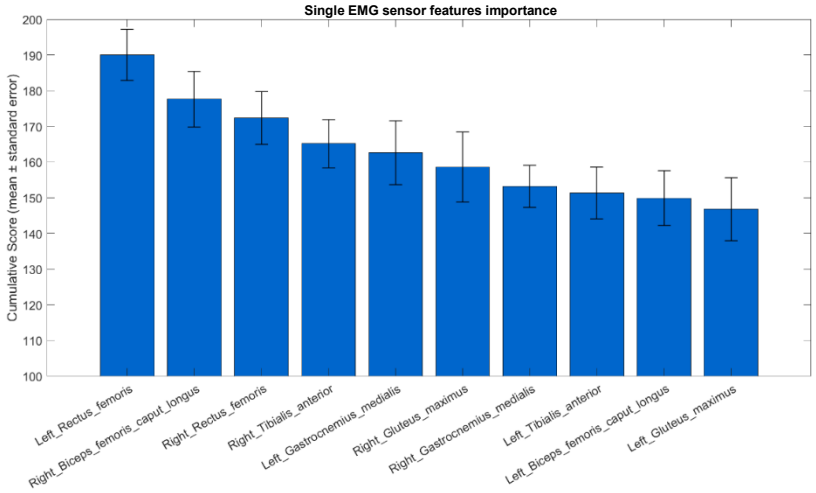

Figure 5.22 Cumulative feature importance (mean ± standard error) aggregated by muscle

Conversely, fNIRS features, though less represented among the top-ranked predictors, provided complementary information, suggesting their involvement in FoG episodes.

To provide an overall view of how informative each sensing modality was, the cumulative feature importance scores were aggregated across IMU, EMG, and fNIRS features. As shown in the figure below, the three modalities contributed unevenly to the classification task. IMU features exhibited the highest cumulative importance, confirming the dominant role of gait kinematics in distinguishing among noFoG, preFoG, and FoG epochs. EMG features followed, reflecting their sensitivity to changes in muscle activation patterns preceding and accompanying freezing episodes. fNIRS features, while less influential than the two peripheral modalities, still contributed non-negligibly, indicating that cortical hemodynamics carries complementary information about the cognitive-motor dynamics underlying FoG behavior.

Statistical testing confirmed that these differences were significant, with the pairs exceeding the Bonferroni-corrected threshold highlighted by double asterisks in the boxplot below.

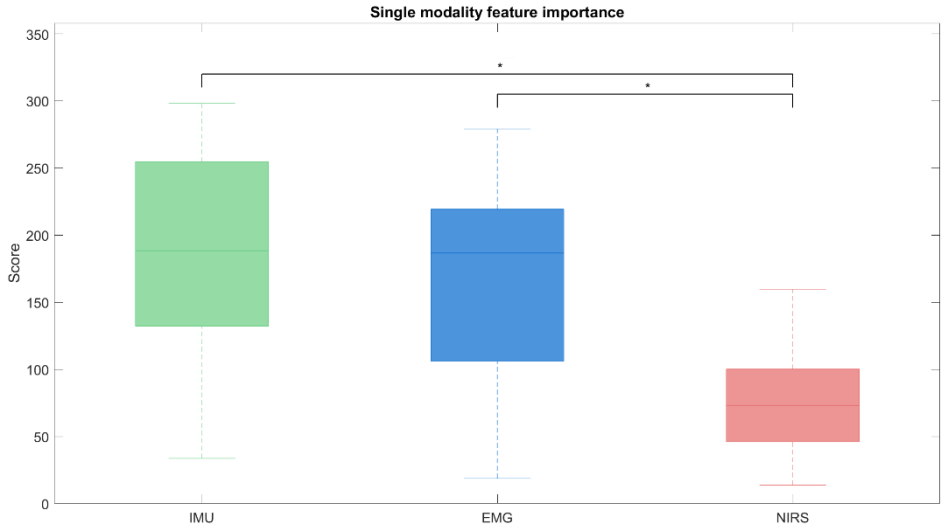

*Figure 5.23 Cumulative feature importance grouped by sensing modality. Statistically significant differences between modalities are indicated with * ($p < 0.05$)*

6 Discussion

6.1 Events Definition

The definition of FoG and preFoG events in this work relied directly on expert video annotation, which represents the gold standard in FoG research and ensures the highest possible reliability for training and validating automatic detection systems.

Regarding gait event detection, the step-detection procedure combined classical approaches, such as the IMU-based angular-velocity peak detection described by Renggli et al. (2020) [151], with a strategy specifically adapted for FoG, inspired by the step identification proposed by Borzì et al. (2021) [176]. This hybrid solution enabled the algorithm to remain sensitive in conditions where the step cycle becomes irregular, attenuated, or fragmented, as typically observed during freezing episodes.

Turn identification was performed through an angular velocity-based approach that proved highly reliable and required minimal adaptation from the original algorithm [153]. Turns represent stereotyped motor events with a well-defined kinematic signature, which remains identifiable even in the presence of mild gait alterations, explaining the strong performance of the method in this context.

However, the algorithm may fragment turn segments when a FoG episode occurs during the turning phase, as the characteristic rotational velocity pattern is disrupted. This issue is handled afterwards, since turn segments overlapping with FoG or preFoG are explicitly removed and not used in subsequent analyses. As a result, these detection “failures” do not affect the validity of the final event labels nor the downstream analyses.

Overall, the event definition pipeline allowed for consistent segmentation of walking, turning, preFoG, and FoG periods, enabling both cortical activation analysis and supervised machine-learning tasks to be built upon a coherent temporal representation of the motor behavior.

6.2 Cortical activation patterns from β-maps

The β-map analyses provided insight into the cortical dynamics associated with walking, turning, and freezing behavior. At the single-subject level, contrasts consistently revealed widespread activation differences, including bilateral prefrontal, premotor, and supplementary motor areas. These findings align with several fNIRS studies reporting increased prefrontal recruitment in patients with FoG, interpreted as compensatory engagement of executive control during gait [55]. The spatially distributed increases observed during FoG relative to walk or turn further support the hypothesis of "network overload," whereby the frontal executive network becomes excessively taxed during complex or destabilized gait.

In the FoG vs preFoG contrasts, activation patterns were typically stronger and more spatially extensive during FoG, often involving temporo-parietal regions as well. This is in line with models suggesting that the breakdown of automaticity during gait deterioration recruits additional multimodal integration areas prior to complete freezing [198].

Group-level analyses, performed using paired tests across patients with FoG, yielded only small, focal clusters of significant activation differences. This limited statistical power was expected given the modest sample size and the high inter-subject variability characteristic of FoG, which has been documented extensively in prior work [28]. Nonetheless, the clusters detected were largely consistent with those highlighted at the individual level, especially within frontal and motor regions.

Between-group comparisons (PD-FoG vs PD-noFoG) during walk and turn revealed small differences, with PD-FoG patients showing clusters of increased activation in premotor, frontal and parietal areas, while PD-noFoG displayed localized greater activations in temporal regions in some conditions. These modest effects are coherent with previous findings suggesting that patients who experience FoG often show altered cortical recruitment even during non-freezing gait, although such differences are subtle and heterogeneous [161].

Taken together, the β-map analyses support the emerging view that FoG is associated with disrupted allocation of executive and sensorimotor cortical resources, but they also highlight the difficulty of obtaining consistent group-level signatures due to intrinsic variability across patients and freezing episodes.

6.3 Machine learning for FoG detection and prediction

The machine-learning analysis demonstrated that multimodal sensing combined with classical feature-based algorithms can achieve robust FoG and preFoG detection performance. In the binary classification problem (FoG vs noFoG), the models achieved high balanced accuracy across all folds, with values greater than those reported in the literature for IMU-based FoG detection [184]. The kNN and Random Forest models showed particularly stable behavior, suggesting that a combination of nearest-neighbor structure and ensemble-based decision boundaries is well suited to handle the variability inherent in FoG kinematics.

Performance decreased in the three-class problem (FoG vs preFoG vs noFoG), confirming that preFoG is substantially harder to discriminate, but also less represented in the training phase. This reduction mirrors findings from prior studies, where preFoG classification often falls between 70-85%, reflecting the ambiguity and high inter-subject variability of transitional states [184]. Models tended to confuse preFoG more frequently with noFoG than with FoG (respectively 25.3% and 12.9% of total preFoG epochs), suggesting that preFoG represents a mild gait degradation that shares more characteristics with normal walking than with full freezing.

From the LOPO cross-validation emerged a relatively great inter-subject variability in classification performance (6-9% balanced accuracy standard deviation across folds), indicating a variability in FoG expression in this study cohort.

The specificity analysis performed on PD-noFoG subjects showed that the best model produced very few false positives (<1% mislabeled as FoG), with the vast majority of epochs correctly identified as noFoG. This is an important clinical requirement and is rarely reported in prior works; many existing FoG detectors are not explicitly evaluated on subjects who don’t report freezing.

Feature-importance analysis revealed a clear hierarchy among sensing modalities: IMU features were the most informative, followed by EMG and then fNIRS, although statistically significant differences were found only between IMU and fNIRS, and between EMG and fNIRS. This ranking aligns with the expected results, since gait-kinematic signals are commonly used in FoG detection tasks and are well known also in terms of which informative FoG descriptors to extract [184], while fNIRS has not been used yet in FoG detection tasks, so its importance in this field is expected to increase in the next few years. Within each modality, feature importance varied across sensors and muscles, although statistical testing showed that these differences were not significant.

Overall, the machine-learning results confirm that traditional feature-based approaches, when carefully engineered and combined with rigorous LOPO validation, can achieve strong generalization in FoG detection. At the same time, the drop in performance for the preFoG class and the observed inter-subject variability highlight clear areas for future research.

7 Conclusions

This thesis investigated FoG and its dynamics through a combined neurophysiological and machine-learning framework, integrating fNIRS-derived cortical activation patterns with multimodal sensor data. The work produced two main contributions. First, the analysis of β-maps revealed cortical signatures associated with walking, turning, and freezing behavior, highlighting frontal and sensorimotor network involvement and confirming several findings previously reported in the literature regarding the executive and integration deficits underlying FoG. Although group-level effects remained subtle due to inter-subject variability and limited statistical power, the overall pattern of results supports current hypotheses describing FoG as a failure of automaticity accompanied by compensatory frontal recruitment.

Second, the machine-learning component demonstrated that FoG and preFoG can be detected with high accuracy using classical feature-based models trained on IMU, EMG, and fNIRS data. The binary FoG vs noFoG task yielded strong generalization in a strict LOPO setting, while the more challenging three-class problem confirmed that preFoG remains intrinsically difficult to discriminate, reflecting its transitional and heterogeneous nature.

The feature-importance analyses emphasized the central role of peripheral sensors, particularly IMUs, in capturing FoG-related motor signatures, while also showing that EMG and fNIRS provide complementary information.

Overall, the results demonstrate that multimodal sensing combined with interpretable, feature-based machine learning provides a reliable pipeline for characterizing and detecting FoG. At the same time, the findings highlight the complex interplay between cortical and peripheral markers of gait deterioration and the need for models trained on larger samples, in order to better accommodate the variability observed across individuals and freezing episodes.

8 Limitations and Future Directions

Although the present work provides a complete multimodal framework for FoG characterization and detection, several limitations must be acknowledged, together with clear avenues for future development.

Sample size and study design

The number of participants included in the study was limited, but this constraint is intrinsic to the context in which the work was carried out. The thesis was embedded within a preclinical trial in early stage, and substantial effort was dedicated to protocol definition, sensor setup and synchronization across modalities, data acquisition, and the development of the entire preprocessing pipeline. As a result, the dataset reflects the initial phase of a long-term clinical study rather than a consolidated cohort. This should not be interpreted as a methodological limitation of the analytical approach, but rather as a natural consequence of contributing to a project in all its developmental stages. Nevertheless, as the trial progresses, expanding the participant pool will be essential to strengthen statistical power and enhance the generalizability of the developed models.

Event-definition parameters and epoch construction

Several components of the event-definition pipeline rely on parameters that could be further optimized. In particular, the duration of preFoG windows, as well as the length and overlap of the analysis epochs, were chosen based on reasonable assumptions and preliminary literature but were not systematically tuned. Since these parameters influence the temporal resolution of cortical analyses and the balance of training samples in machine learning models, future work should investigate data-driven or adaptive strategies for refining them.

Hyperparameter tuning.

The machine-learning models were intentionally kept relatively simple to prioritize interpretability and stability. However, more systematic hyperparameter optimization, with grid search, or nested cross-validation, could yield additional performance improvements, particularly for the multiclass problem where preFoG remains challenging. Such tuning would also enable a more rigorous comparison between models and help establish well-optimized baselines for future studies.

Enhancing fNIRS feature extraction

The fNIRS component was intentionally kept comparable to IMU and EMG in terms of feature extraction window (2 seconds epochs), but this imposes constraints given the inherently slow nature of the hemodynamic response. With only 10 samples per epoch, part of the physiologically informative dynamics may be missed. Extending the temporal window for hemodynamic feature computation and extracting connectivity features may substantially improve the discriminative power of fNIRS. These refinements could help clarify the role of cortical contributions in preFoG and FoG detection.

Single-modality model assessment

Although the multimodal approach demonstrated strong performance, an explicit evaluation of the contribution of each modality through single-modality models would provide clearer insight into how much each biosignal improves detection.

From epoch classification to continuous prediction

The current pipeline operates on overlapping 2 seconds epochs, producing discrete class predictions rather than a continuous decision stream. This representation, while convenient for model training, may obscure higher-level temporal patterns, such as anticipatory fluctuations or systematic lags in preFoG → FoG transitions. Future work could reconstruct continuous time-series predictions by integrating the per-epoch outputs and applying smoothing, temporal filtering, or sequence-based models. This would allow examination of timing precision, identification delays, and potential early-warning signatures.

Bibliography

[1] L. V. Kalia e A. E. Lang, «Parkinson's disease», *The lancet*, vol. 386, fasc. 9996, pp. 896–912, 2015.

[2] K. R. Chaudhuri, D. G. Healy, e A. H. Schapira, «Non-motor symptoms of Parkinson's disease: diagnosis and management», *Lancet Neurol.*, vol. 5, fasc. 3, pp. 235–245, 2006.

[3] M. Goedert, M. Masuda-Suzukake, e B. Falcon, «Like prions: the propagation of aggregated tau and α-synuclein in neurodegeneration», *Brain*, vol. 140, fasc. 2, pp. 266–278, 2017.

[4] M. G. Spillantini, M. L. Schmidt, V. M.-Y. Lee, J. Q. Trojanowski, R. Jakes, e M. Goedert, «α-Synuclein in Lewy bodies», *Nature*, vol. 388, fasc. 6645, pp. 839–840, 1997.

[5] «What Causes Parkinson's Disease?», ParkinsonsDisease.net. Consultato: 29 ottobre 2025. [Online]. Disponibile su: https://parkinsonsdisease.net/basics/pathophysiology-what-is-it

[6] H. Braak, K. Del Tredici, U. Rüb, R. A. De Vos, E. N. J. Steur, e E. Braak, «Staging of brain pathology related to sporadic Parkinson's disease», *Neurobiol. Aging*, vol. 24, fasc. 2, pp. 197–211, 2003.

[7] R. L. Albin, A. B. Young, e J. B. Penney, «The functional anatomy of basal ganglia disorders», *Trends Neurosci.*, vol. 12, fasc. 10, pp. 366–375, 1989.

[8] M. R. DeLong, «Primate models of movement disorders of basal ganglia origin», *Trends Neurosci.*, vol. 13, fasc. 7, pp. 281–285, 1990.

[9] R. B. Postuma e D. Berg, «Prodromal Parkinson's disease: the decade past, the decade to come», *Mov. Disord.*, vol. 34, fasc. 5, pp. 665–675, 2019.

[10] K. Del Tredici e H. Braak, «Lewy pathology and neurodegeneration in premotor Parkinson's disease», *Mov. Disord.*, vol. 27, fasc. 5, pp. 597–607, 2012.

[11] J. Parkinson, «An essay on the shaking palsy», *J. Neuropsychiatry Clin. Neurosci.*, vol. 14, fasc. 2, pp. 223–236, 2002.

[12] J. Jankovic *et al.*, «Variable expression of Parkinson's disease: A base-line analysis of the DAT ATOP cohort», *Neurology*, vol. 40, fasc. 10, pp. 1529–1529, 1990.

[13] J. Jankovic, «Parkinson's disease: clinical features and diagnosis», *J. Neurol. Neurosurg. Psychiatry*, vol. 79, fasc. 4, pp. 368–376, 2008.

[14] R. B. Postuma *et al.*, «MDS clinical diagnostic criteria for Parkinson's disease», *Mov. Disord.*, vol. 30, fasc. 12, pp. 1591–1601, 2015.

[15] Ü. Ö. Akdemir, H. A. T. Bora, e L. Ö. Atay, «Dopamine transporter spect imaging in Parkinson's disease and parkinsoniandisorders», *Turk. J. Med. Sci.*, vol. 51, fasc. 2, pp. 400–410, 2021.

[16] M. Dasari e R. V. Medapati, «Cerebrospinal Fluid Biomarkers for Diagnosis of Parkinson's disease: A Systematic Review», *Cureus*, feb. 2025, doi: 10.7759/cureus.79386.

[17] C. G. Goetz *et al.*, «Movement Disorder Society-sponsored revision of the Unified Parkinson's Disease Rating Scale (MDS-UPDRS): scale presentation and clinimetric testing results», *Mov. Disord. Off. J. Mov. Disord. Soc.*, vol. 23, fasc. 15, pp. 2129–2170, 2008.

[18] M. M. Hoehn e M. D. Yahr, «Parkinsonism: onset, progression, and mortality», *Neurology*, vol. 17, fasc. 5, pp. 427–427, 1967.

[19] C. G. Goetz *et al.*, «Movement Disorder Society Task Force report on the Hoehn and Yahr staging scale: status and recommendations the Movement Disorder Society Task Force on rating scales for Parkinson's disease», *Mov. Disord.*, vol. 19, fasc. 9, pp. 1020–1028, 2004.

[20] C. W. Olanow, M. B. Stern, e K. Sethi, «The scientific and clinical basis for the treatment of Parkinson disease (2009)», *Neurology*, vol. 72, fasc. 21_supplement_4, pp. S1–S136, 2009.
[21] A. H. Schapira, K. R. Chaudhuri, e P. Jenner, «Non-motor features of Parkinson disease», *Nat. Rev. Neurosci.*, vol. 18, fasc. 7, pp. 435–450, 2017.
[22] S. H. Fox *et al.*, «International Parkinson and movement disorder society evidence-based medicine review: update on treatments for the motor symptoms of Parkinson's disease», *Mov. Disord.*, vol. 33, fasc. 8, pp. 1248–1266, 2018.
[23] G. Deuschl *et al.*, «A randomized trial of deep-brain stimulation for Parkinson's disease», *N. Engl. J. Med.*, vol. 355, fasc. 9, pp. 896–908, 2006.
[24] F. M. Weaver *et al.*, «Bilateral deep brain stimulation vs best medical therapy for patients with advanced Parkinson disease: a randomized controlled trial», *Jama*, vol. 301, fasc. 1, pp. 63–73, 2009.
[25] C. L. Tomlinson *et al.*, «Physiotherapy intervention in Parkinson's disease: systematic review and meta-analysis», *Bmj*, vol. 345, 2012.
[26] G. M. Petzinger, B. E. Fisher, S. McEwen, J. A. Beeler, J. P. Walsh, e M. W. Jakowec, «Exercise-enhanced neuroplasticity targeting motor and cognitive circuitry in Parkinson's disease», *Lancet Neurol.*, vol. 12, fasc. 7, pp. 716–726, 2013.
[27] G. Winston, N. Kharas, P. Svenningsson, A. Jha, e M. G. Kaplitt, «Gene therapy for Parkinson's disease: trials and technical advances», *Lancet Neurol.*, vol. 24, fasc. 6, pp. 548–556, 2025.
[28] J. G. Nutt, B. R. Bloem, N. Giladi, M. Hallett, F. B. Horak, e A. Nieuwboer, «Freezing of gait: moving forward on a mysterious clinical phenomenon», *Lancet Neurol.*, vol. 10, fasc. 8, pp. 734–744, 2011.
[29] A. Nieuwboer e N. Giladi, «Characterizing freezing of gait in Parkinson's disease: Models of an episodic phenomenon», *Mov. Disord.*, vol. 28, fasc. 11, pp. 1509–1519, 2013, doi: 10.1002/mds.25683.
[30] P. Ginis, E. Heremans, A. Ferrari, E. M. Bekkers, C. G. Canning, e A. Nieuwboer, «External input for gait in people with Parkinson's disease with and without freezing of gait: one size does not fit all», *J. Neurol.*, vol. 264, fasc. 7, pp. 1488–1496, 2017.
[31] S. Perez-Lloret *et al.*, «Prevalence, determinants, and effect on quality of life of freezing of gait in Parkinson disease», *JAMA Neurol.*, vol. 71, fasc. 7, pp. 884–890, 2014.
[32] S. J. Lewis e J. M. Shine, «The next step: a common neural mechanism for freezing of gait», *The Neuroscientist*, vol. 22, fasc. 1, pp. 72–82, 2016.
[33] A. H. Snijders *et al.*, «Gait-related cerebral alterations in patients with Parkinson's disease with freezing of gait», *Brain*, vol. 134, fasc. 1, pp. 59–72, 2011.
[34] J. M. Shine *et al.*, «Freezing of gait in Parkinson's disease is associated with functional decoupling between the cognitive control network and the basal ganglia», *Brain*, vol. 136, fasc. 12, pp. 3671–3681, 2013.
[35] C. Karachi *et al.*, «Cholinergic mesencephalic neurons are involved in gait and postural disorders in Parkinson disease», *J. Clin. Invest.*, vol. 120, fasc. 8, pp. 2745–2754, 2010.
[36] E. Heremans *et al.*, «Cognitive aspects of freezing of gait in Parkinson's disease: a challenge for rehabilitation», *J. Neural Transm.*, vol. 120, fasc. 4, pp. 543–557, 2013.
[37] A. Nieuwboer *et al.*, «Reliability of the new freezing of gait questionnaire: agreement between patients with Parkinson's disease and their carers», *Gait Posture*, vol. 30, fasc. 4, pp. 459–463, 2009.
[38] N. Giladi, H. Shabtai, E. Simon, S. Biran, J. Tal, e A. Korczyn, «Construction of freezing of gait questionnaire for patients with Parkinsonism», *Parkinsonism Relat. Disord.*, vol. 6, fasc. 3, pp. 165–170, 2000.
[39] M. Mancini *et al.*, «Technology for measuring freezing of gait: Current state of the art and recommendations», *J. Park. Dis.*, vol. 15, fasc. 1, pp. 19–40, 2025.

[40] J. Schaafsma, Y. Balash, T. Gurevich, A. Bartels, J. M. Hausdorff, e N. Giladi, «Characterization of freezing of gait subtypes and the response of each to levodopa in Parkinson's disease», *Eur. J. Neurol.*, vol. 10, fasc. 4, pp. 391–398, 2003.
[41] S. T. Moore, H. G. MacDougall, D. T. O'Keeffe, J.-M. Gracies, e V. S. C. Fung, «Freezing of gait affects the dynamics of Parkinsonian gait», *Gait Posture*, vol. 27, fasc. 4, pp. 668–673, 2008, doi: 10.1016/j.gaitpost.2007.08.008.
[42] M. Mancini, A. Weiss, T. Herman, e J. M. Hausdorff, «Turn Around Freezing: Community-Living Turning Behavior in People with Parkinson's Disease», *Front. Neurol.*, vol. 9, p. 18, gen. 2018, doi: 10.3389/fneur.2018.00018.
[43] W. Thevathasan *et al.*, «Pedunculopontine nucleus stimulation improves gait freezing in Parkinson disease», *Neurosurgery*, vol. 69, fasc. 6, pp. 1248–1254, 2011.
[44] M. U. Ferraye *et al.*, «Effects of pedunculopontine nucleus area stimulation on gait disorders in Parkinson's disease», *Brain*, vol. 133, fasc. 1, pp. 205–214, 2010.
[45] A. Nieuwboer e N. Giladi, «Cueing for freezing of gait in Parkinson's disease: a review of the scientific basis and clinical effectiveness», *Parkinsonism Relat. Disord.*, vol. 19, fasc. 2, pp. 189–197, 2013, doi: 10.1016/j.parkreldis.2012.09.012.
[46] E. M. Bekkers *et al.*, «Do patients with Parkinson's disease with freezing of gait respond differently than those without to treadmill training augmented by virtual reality?», *Neurorehabil. Neural Repair*, vol. 34, fasc. 5, pp. 440–449, 2020.
[47] C. C. Walton, J. M. Shine, L. Mowszowski, S. L. Naismith, e S. J. Lewis, «Freezing of gait in Parkinson's disease: current treatments and the potential role for cognitive training», *Restor. Neurol. Neurosci.*, vol. 32, fasc. 3, pp. 411–422, 2014.
[48] M. Macht e H. Ellgring, «Behavioral analysis of the freezing phenomenon in Parkinson's disease: a case study», *J. Behav. Ther. Exp. Psychiatry*, vol. 30, fasc. 3, pp. 241–247, 1999.
[49] R. B. Buxton, K. Uludağ, D. J. Dubowitz, e T. T. Liu, «Modeling the hemodynamic response to brain activation», *NeuroImage*, vol. 23, pp. S220–S233, gen. 2004, doi: 10.1016/j.neuroimage.2004.07.013.
[50] N. K. Logothetis, «What we can do and what we cannot do with fMRI», *Nature*, vol. 453, fasc. 7197, pp. 869–878, giu. 2008, doi: 10.1038/nature06976.
[51] J. Steinbrink, A. Villringer, F. Kempf, D. Haux, S. Boden, e H. Obrig, «Illuminating the BOLD signal: combined fMRI–fNIRS studies», *Magn. Reson. Imaging*, vol. 24, fasc. 4, pp. 495–505, mag. 2006, doi: 10.1016/j.mri.2005.12.034.
[52] T. J. Huppert, M. A. Franceschini, e D. A. Boas, «Noninvasive Imaging of Cerebral Activation with Diffuse Optical Tomography», in *In Vivo Optical Imaging of Brain Function. 2nd edition*, CRC Press/Taylor & Francis, 2009. Consultato: 11 ottobre 2025. [Online]. Disponibile su: https://www.ncbi.nlm.nih.gov/books/NBK20225/
[53] M. Ferrari e V. Quaresima, «A brief review on the history of human functional near-infrared spectroscopy (fNIRS) development and fields of application», *NeuroImage*, vol. 63, fasc. 2, pp. 921–935, nov. 2012, doi: 10.1016/j.neuroimage.2012.03.049.
[54] D. M. Kustov, A. S. Sharova, V. I. Makarov, A. V. Borodkin, T. A. Saveleva, e V. B. Loschenov, «Evaluating the dynamics of brain tissue oxygenation using near-infrared spectroscopy on various experimental models», *Laser Phys. Lett.*, vol. 16, fasc. 11, p. 115602, nov. 2019, doi: 10.1088/1612-202X/ab4182.
[55] I. Maidan, H. Bernad-Elazari, E. Gazit, N. Giladi, e J. M. Hausdorff, «Changes in oxygenated hemoglobin link freezing of gait to frontal activation in patients with Parkinson disease: an fNIRS study of transient motor-cognitive failures», *J. Neurol.*, vol. 262, fasc. 4, pp. 899–908, apr. 2015, doi: 10.1007/s00415-015-7650-6.
[56] P. Pinti *et al.*, «A Review on the Use of Wearable Functional Near-Infrared Spectroscopy in Naturalistic Environments», *Jpn. Psychol. Res.*, vol. 60, fasc. 4, pp. 347–373, 2018, doi: 10.1111/jpr.12206.

[57] M. Rupawala, H. Dehghani, S. J. E. Lucas, P. Tino, e D. Cruse, «Shining a Light on Awareness: A Review of Functional Near-Infrared Spectroscopy for Prolonged Disorders of Consciousness», *Front. Neurol.*, vol. 9, mag. 2018, doi: 10.3389/fneur.2018.00350.
[58] G. Strangman, D. A. Boas, e J. P. Sutton, «Non-invasive neuroimaging using near-infrared light», *Biol. Psychiatry*, vol. 52, fasc. 7, pp. 679–693, ott. 2002, doi: 10.1016/S0006-3223(02)01550-0.
[59] D. A. Boas, K. Chen, D. Grebert, e M. A. Franceschini, «Improving the diffuse optical imaging spatial resolution of the cerebral hemodynamic response to brain activation in humans», *Opt. Lett.*, vol. 29, fasc. 13, pp. 1506–1508, lug. 2004, doi: 10.1364/OL.29.001506.
[60] D. T. Delpy, M. Cope, P. van der Zee, S. Arridge, S. Wray, e J. Wyatt, «Estimation of optical pathlength through tissue from direct time of flight measurement», *Phys. Med. Biol.*, vol. 33, fasc. 12, p. 1433, dic. 1988, doi: 10.1088/0031-9155/33/12/008.
[61] F. Scholkmann e M. Wolf, «General equation for the differential pathlength factor of the frontal human head depending on wavelength and age», *J. Biomed. Opt.*, vol. 18, fasc. 10, p. 105004, ott. 2013, doi: 10.1117/1.JBO.18.10.105004.
[62] F. Scholkmann, A. J. Metz, e M. Wolf, «Measuring tissue hemodynamics and oxygenation by continuous-wave functional near-infrared spectroscopy—how robust are the different calculation methods against movement artifacts?», *Physiol. Meas.*, vol. 35, fasc. 4, p. 717, mar. 2014, doi: 10.1088/0967-3334/35/4/717.
[63] S. R. Arridge, «Optical tomography in medical imaging», *Inverse Probl.*, vol. 15, fasc. 2, pp. R41–R93, apr. 1999, doi: 10.1088/0266-5611/15/2/022.
[64] D. A. Boas *et al.*, «Imaging the body with diffuse optical tomography», *IEEE Signal Process. Mag.*, vol. 18, fasc. 6, pp. 57–75, nov. 2001, doi: 10.1109/79.962278.
[65] G. Strangman, M. A. Franceschini, e D. A. Boas, «Factors affecting the accuracy of near-infrared spectroscopy concentration calculations for focal changes in oxygenation parameters», *NeuroImage*, vol. 18, fasc. 4, pp. 865–879, apr. 2003, doi: 10.1016/S1053-8119(03)00021-1.
[66] Q. Fang e D. A. Boas, «Monte Carlo Simulation of Photon Migration in 3D Turbid Media Accelerated by Graphics Processing Units», *Opt. Express*, vol. 17, fasc. 22, pp. 20178–20190, ott. 2009, doi: 10.1364/OE.17.020178.
[67] E. Okada *et al.*, «Theoretical and Experimental Investigation of the Influence of Frontal Sinus on the Sensitivity of the NIRS Signal in the Adult Head», in *Oxygen Transport to Tissue XXXI*, E. Takahashi e D. F. Bruley, A c. di, Boston, MA: Springer US, 2010, pp. 231–236. doi: 10.1007/978-1-4419-1241-1_33.
[68] F.-H. Lin, T. Witzel, S. P. Ahlfors, S. M. Stufflebeam, J. W. Belliveau, e M. S. Hämäläinen, «Assessing and improving the spatial accuracy in MEG source localization by depth-weighted minimum-norm estimates», *NeuroImage*, vol. 31, fasc. 1, pp. 160–171, mag. 2006, doi: 10.1016/j.neuroimage.2005.11.054.
[69] Z. Cai *et al.*, «Diffuse optical reconstructions of functional near infrared spectroscopy data using maximum entropy on the mean», *Sci. Rep.*, vol. 12, fasc. 1, p. 2316, feb. 2022, doi: 10.1038/s41598-022-06082-1.
[70] C. Amblard, E. Lapalme, e J.-M. Lina, «Biomagnetic Source Detection by Maximum Entropy and Graphical Models», *IEEE Trans. Biomed. Eng.*, vol. 51, fasc. 3, pp. 427–442, mar. 2004, doi: 10.1109/TBME.2003.820999.
[71] R. Cooper *et al.*, «A Systematic Comparison of Motion Artifact Correction Techniques for Functional Near-Infrared Spectroscopy», *Front. Neurosci.*, vol. 6, ott. 2012, doi: 10.3389/fnins.2012.00147.
[72] S. Brigadoi *et al.*, «Motion artifacts in functional near-infrared spectroscopy: A comparison of motion correction techniques applied to real cognitive data», *NeuroImage*, vol. 85, pp. 181–191, gen. 2014, doi: 10.1016/j.neuroimage.2013.04.082.

[73] L. Pollonini, C. Olds, H. Abaya, H. Bortfeld, M. S. Beauchamp, e J. S. Oghalai, «Auditory cortex activation to natural speech and simulated cochlear implant speech measured with functional near-infrared spectroscopy», *Hear. Res.*, vol. 309, pp. 84–93, mar. 2014, doi: 10.1016/j.heares.2013.11.007.
[74] L. Pollonini, C. Olds, H. Abaya, H. Bortfeld, M. S. Beauchamp, e J. S. Oghalai, «Auditory cortex activation to natural speech and simulated cochlear implant speech measured with functional near-infrared spectroscopy», *Hear. Res.*, vol. 309, pp. 84–93, 2014.
[75] F. A. Fishburn, R. S. Ludlum, C. J. Vaidya, e A. V. Medvedev, «Temporal Derivative Distribution Repair (TDDR): A motion correction method for fNIRS», *NeuroImage*, vol. 184, pp. 171–179, gen. 2019, doi: 10.1016/j.neuroimage.2018.09.025.
[76] H. Huang *et al.*, «Resting-state brain network analysis and applied evaluation of global developmental delay in preterm infants: A functional near-infrared spectroscopic study», *Biosens. Bioelectron. X*, vol. 21, p. 100546, dic. 2024, doi: 10.1016/j.biosx.2024.100546.
[77] L. Gagnon, M. A. Yücel, D. A. Boas, e R. J. Cooper, «Further improvement in reducing superficial contamination in NIRS using double short separation measurements», *NeuroImage*, vol. 85, pp. 127–135, gen. 2014, doi: 10.1016/j.neuroimage.2013.01.073.
[78] I. Tachtsidis e F. Scholkmann, «False positives and false negatives in functional near-infrared spectroscopy: issues, challenges, and the way forward», *Neurophotonics*, vol. 3, fasc. 3, p. 031405, mar. 2016, doi: 10.1117/1.NPh.3.3.031405.
[79] A. Duncan *et al.*, «Measurement of Cranial Optical Path Length as a Function of Age Using Phase Resolved Near Infrared Spectroscopy», *Pediatr. Res.*, vol. 39, fasc. 5, pp. 889–894, mag. 1996, doi: 10.1203/00006450-199605000-00025.
[80] J. W. Barker, A. Aarabi, e T. J. Huppert, «Autoregressive model based algorithm for correcting motion and serially correlated errors in fNIRS», *Biomed. Opt. Express*, vol. 4, fasc. 8, pp. 1366–1379, ago. 2013, doi: 10.1364/BOE.4.001366.
[81] S. Tak, M. Uga, G. Flandin, I. Dan, e W. D. Penny, «Sensor space group analysis for fNIRS data», *J. Neurosci. Methods*, vol. 264, pp. 103–112, mag. 2016, doi: 10.1016/j.jneumeth.2016.03.003.
[82] H. Khan, R. Khadka, M. S. Sultan, A. Yazidi, H. Ombao, e P. Mirtaheri, «Unleashing the potential of fNIRS with machine learning: classification of fine anatomical movements to empower future brain-computer interface», *Front. Hum. Neurosci.*, vol. 18, p. 1354143, feb. 2024, doi: 10.3389/fnhum.2024.1354143.
[83] K.-S. Hong, M. J. Khan, e M. J. Hong, «Feature Extraction and Classification Methods for Hybrid fNIRS-EEG Brain-Computer Interfaces», *Front. Hum. Neurosci.*, vol. 12, giu. 2018, doi: 10.3389/fnhum.2018.00246.
[84] Z. Li *et al.*, «Dynamic functional connectivity revealed by resting-state functional near-infrared spectroscopy», *Biomed. Opt. Express*, vol. 6, fasc. 7, p. 2337, lug. 2015, doi: 10.1364/BOE.6.002337.
[85] H. Niu *et al.*, «Abnormal dynamic functional connectivity and brain states in Alzheimer's diseases: functional near-infrared spectroscopy study», *Neurophotonics*, vol. 6, fasc. 02, p. 1, giu. 2019, doi: 10.1117/1.NPh.6.2.025010.
[86] M. J. Khan, U. Ghafoor, e K.-S. Hong, «Early Detection of Hemodynamic Responses Using EEG: A Hybrid EEG-fNIRS Study», *Front. Hum. Neurosci.*, vol. 12, nov. 2018, doi: 10.3389/fnhum.2018.00479.
[87] N. Naseer e K.-S. Hong, «fNIRS-based brain-computer interfaces: a review», *Front. Hum. Neurosci.*, vol. 9, gen. 2015, doi: 10.3389/fnhum.2015.00003.
[88] H. Santosa, A. Aarabi, S. B. Perlman, e T. J. Huppert, «Characterization and correction of the false-discovery rates in resting state connectivity using functional near-infrared spectroscopy», *J. Biomed. Opt.*, vol. 22, fasc. 5, p. 055002, mag. 2017, doi: 10.1117/1.JBO.22.5.055002.

[89] R. M. Hutchison *et al.*, «Dynamic functional connectivity: Promise, issues, and interpretations», *NeuroImage*, vol. 80, pp. 360–378, ott. 2013, doi: 10.1016/j.neuroimage.2013.05.079.
[90] Y. Peng, C. Li, Q. Chen, Y. Zhu, e L. Sun, «Functional Connectivity Analysis and Detection of Mental Fatigue Induced by Different Tasks Using Functional Near-Infrared Spectroscopy», *Front. Neurosci.*, vol. 15, mar. 2022, doi: 10.3389/fnins.2021.771056.
[91] K. J. Verdière, R. N. Roy, e F. Dehais, «Detecting Pilot's Engagement Using fNIRS Connectivity Features in an Automated vs. Manual Landing Scenario», *Front. Hum. Neurosci.*, vol. 12, gen. 2018, doi: 10.3389/fnhum.2018.00006.
[92] F. Scholkmann *et al.*, «A review on continuous wave functional near-infrared spectroscopy and imaging instrumentation and methodology», *NeuroImage*, vol. 85, pp. 6–27, gen. 2014, doi: 10.1016/j.neuroimage.2013.05.004.
[93] «fNIRS Software: NIRS Analysis | NIRS Data Recording | fNIRS Systems | NIRS Devices | NIRx», NIRx Medical Technologies. Consultato: 18 novembre 2025. [Online]. Disponibile su: https://nirx.net/software
[94] V. Agostini, M. Ghislieri, S. Rosati, G. Balestra, e M. Knaflitz, «Surface Electromyography Applied to Gait Analysis: How to Improve Its Impact in Clinics?», *Front. Neurol.*, vol. 11, set. 2020, doi: 10.3389/fneur.2020.00994.
[95] M. Al-Ayyad, H. A. Owida, R. De Fazio, B. Al-Naami, e P. Visconti, «Electromyography Monitoring Systems in Rehabilitation: A Review of Clinical Applications, Wearable Devices and Signal Acquisition Methodologies», *Electronics*, vol. 12, fasc. 7, p. 1520, mar. 2023, doi: 10.3390/electronics12071520.
[96] R. Merletti e D. Farina, *Surface Electromyography: Physiology, Engineering, and Applications*. John Wiley & Sons, 2016.
[97] D. Farina, R. Merletti, e R. M. Enoka, «The extraction of neural strategies from the surface EMG», *J. Appl. Physiol.*, vol. 96, fasc. 4, pp. 1486–1495, apr. 2004, doi: 10.1152/japplphysiol.01070.2003.
[98] H. J. Hermens, B. Freriks, C. Disselhorst-Klug, e G. Rau, «Development of recommendations for SEMG sensors and sensor placement procedures», *J. Electromyogr. Kinesiol.*, vol. 10, fasc. 5, pp. 361–374, ott. 2000, doi: 10.1016/S1050-6411(00)00027-4.
[99] C. J. De Luca, «The Use of Surface Electromyography in Biomechanics», *J. Appl. Biomech.*, vol. 13, fasc. 2, pp. 135–163, mag. 1997, doi: 10.1123/jab.13.2.135.
[100] A. Botter, «Bioingegneria della riabilitazione, slide del corso»,
[101] H. H. Hennemann e I. Falck, «Über Kombinationen von aplastischen mit hämolytischen Syndromen», 1957, Consultato: 13 ottobre 2025. [Online]. Disponibile su: https://dx.doi.org/10.1159/000205326
[102] R. M. Enoka e J. Duchateau, «Rate Coding and the Control of Muscle Force», *Cold Spring Harb. Perspect. Med.*, vol. 7, fasc. 10, p. a029702, gen. 2017, doi: 10.1101/cshperspect.a029702.
[103] J. I. Priego-Quesada, M. F. Goethel, K. M. Becker, R. J. Fernandes, e J. P. Vilas-Boas, «How to Work with Electromyography Decomposition in Practical Classes of Exercise Physiology and Biomechanics», *Life*, vol. 12, fasc. 4, p. 483, mar. 2022, doi: 10.3390/life12040483.
[104] I. Campanini, A. Merlo, C. Disselhorst-Klug, L. Mesin, S. Muceli, e R. Merletti, «Fundamental Concepts of Bipolar and High-Density Surface EMG Understanding and Teaching for Clinical, Occupational, and Sport Applications: Origin, Detection, and Main Errors», *Sensors*, vol. 22, fasc. 11, p. 4150, mag. 2022, doi: 10.3390/s22114150.
[105] R. Merletti e P. J. Parker, *Electromyography: Physiology, Engineering, and Non-Invasive Applications*. John Wiley & Sons, 2004.

[106] D. Farina, M. Fosci, e R. Merletti, «Motor unit recruitment strategies investigated by surface EMG variables», *J. Appl. Physiol.*, vol. 92, fasc. 1, pp. 235–247, gen. 2002, doi: 10.1152/jappl.2002.92.1.235.
[107] S. Muceli e R. Merletti, «Tutorial. Frequency analysis of the surface EMG signal: Best practices», *J. Electromyogr. Kinesiol.*, vol. 79, p. 102937, dic. 2024, doi: 10.1016/j.jelekin.2024.102937.
[108] E. A. Clancy, E. L. Morin, e R. Merletti, «Sampling, noise-reduction and amplitude estimation issues in surface electromyography», *J. Electromyogr. Kinesiol.*, vol. 12, fasc. 1, pp. 1–16, feb. 2002, doi: 10.1016/S1050-6411(01)00033-5.
[109] L. Ricardo, J. Luiz, M. Bigliassi, T. F. Dias Kanthack, A. C. De Moraes, e T. Abrao, «Influence of Different Strategies of Treatment Muscle Contraction and Relaxation Phases on EMG Signal Processing and Analysis During Cyclic Exercise», in *Computational Intelligence in Electromyography Analysis - A Perspective on Current Applications and Future Challenges*, G. R. Naik, A c. di, InTech, 2012. doi: 10.5772/50599.
[110] A. Phinyomark, A. Nuidod, P. Phukpattaranont, e C. Limsakul, «Feature Extraction and Reduction of Wavelet Transform Coefficients for EMG Pattern Classification», *Elektron. Ir Elektrotechnika*, vol. 122, fasc. 6, pp. 27–32, giu. 2012, doi: 10.5755/j01.eee.122.6.1816.
[111] B. Hudgins, P. Parker, e R. N. Scott, «A new strategy for multifunction myoelectric control», *IEEE Trans. Biomed. Eng.*, vol. 40, fasc. 1, pp. 82–94, gen. 1993, doi: 10.1109/10.204774.
[112] S. Rampichini, T. M. Vieira, P. Castiglioni, e G. Merati, «Complexity Analysis of Surface Electromyography for Assessing the Myoelectric Manifestation of Muscle Fatigue: A Review», *Entropy*, vol. 22, fasc. 5, p. 529, mag. 2020, doi: 10.3390/e22050529.
[113] S. Karlsson, J. Yu, e M. Akay, «Time-frequency analysis of myoelectric signals during dynamic contractions: a comparative study», *IEEE Trans. Biomed. Eng.*, vol. 47, fasc. 2, pp. 228–238, feb. 2000, doi: 10.1109/10.821766.
[114] X. Zhang e P. Zhou, «Sample Entropy Analysis of Surface EMG for Improved Muscle Activity Onset Detection against Spurious Background Spikes», *J. Electromyogr. Kinesiol. Off. J. Int. Soc. Electrophysiol. Kinesiol.*, vol. 22, fasc. 6, pp. 901–907, dic. 2012, doi: 10.1016/j.jelekin.2012.06.005.
[115] C. E. Shannon, «A mathematical theory of communication», *Bell Syst. Tech. J.*, vol. 27, fasc. 3, pp. 379–423, lug. 1948, doi: 10.1002/j.1538-7305.1948.tb01338.x.
[116] N. A. Turpin, A. Guével, S. Durand, e F. Hug, «Effect of power output on muscle coordination during rowing», *Eur. J. Appl. Physiol.*, vol. 111, fasc. 12, pp. 3017–3029, dic. 2011, doi: 10.1007/s00421-011-1928-x.
[117] T. W. Boonstra, A. Danna-Dos-Santos, H.-B. Xie, M. Roerdink, J. F. Stins, e M. Breakspear, «Muscle networks: Connectivity analysis of EMG activity during postural control», *Sci. Rep.*, vol. 5, fasc. 1, p. 17830, dic. 2015, doi: 10.1038/srep17830.
[118] D. M. Halliday, J. R. Rosenberg, A. M. Amjad, P. Breeze, B. A. Conway, e S. F. Farmer, «A framework for the analysis of mixed time series/point process data—Theory and application to the study of physiological tremor, single motor unit discharges and electromyograms», *Prog. Biophys. Mol. Biol.*, vol. 64, fasc. 2, pp. 237–278, gen. 1995, doi: 10.1016/S0079-6107(96)00009-0.
[119] C. E. Shannon, «A mathematical theory of communication», *Bell Syst. Tech. J.*, vol. 27, fasc. 3, pp. 379–423, lug. 1948, doi: 10.1002/j.1538-7305.1948.tb01338.x.
[120] A. Kraskov, H. Stögbauer, e P. Grassberger, «Estimating mutual information», *Phys. Rev. E*, vol. 69, fasc. 6, p. 066138, giu. 2004, doi: 10.1103/PhysRevE.69.066138.

[121] S. Muceli, A. T. Boye, A. d'Avella, e D. Farina, «Identifying Representative Synergy Matrices for Describing Muscular Activation Patterns During Multidirectional Reaching in the Horizontal Plane», *J. Neurophysiol.*, vol. 103, fasc. 3, pp. 1532–1542, mar. 2010, doi: 10.1152/jn.00559.2009.
[122] R. O'Keeffe *et al.*, «InfoMuNet: Information-theory-based Functional Muscle Network Tracks Sensorimotor Integration Post-stroke», 10 febbraio 2022, *Neuroscience*. doi: 10.1101/2022.02.10.479324.
[123] J. Perry e J. M. Burnfield, «Gait Analysis: Normal and Pathological Function», *J. Sports Sci. Med.*, vol. 9, fasc. 2, p. 353, giu. 2010.
[124] H. G. Kang e J. B. Dingwell, «Dynamics and stability of muscle activations during walking in healthy young and older adults», *J. Biomech.*, vol. 42, fasc. 14, pp. 2231–2237, ott. 2009, doi: 10.1016/j.jbiomech.2009.06.038.
[125] M. C. N. Rosa, A. Marques, S. Demain, C. D. Metcalf, e J. Rodrigues, «Methodologies to assess muscle co-contraction during gait in people with neurological impairment – A systematic literature review», *J. Electromyogr. Kinesiol.*, vol. 24, fasc. 2, pp. 179–191, apr. 2014, doi: 10.1016/j.jelekin.2013.11.003.
[126] S. M. Keloth, S. P. Arjunan, S. Raghav, e D. K. Kumar, «Muscle activation strategies of people with early-stage Parkinson's during walking», *J. NeuroEngineering Rehabil.*, vol. 18, p. 133, set. 2021, doi: 10.1186/s12984-021-00932-1.
[127] A. d'Avella e E. Bizzi, «Shared and specific muscle synergies in natural motor behaviors», *Proc. Natl. Acad. Sci.*, vol. 102, fasc. 8, pp. 3076–3081, feb. 2005, doi: 10.1073/pnas.0500199102.
[128] M. Ghislieri, M. Lanotte, M. Knaflitz, L. Rizzi, e V. Agostini, «Muscle synergies in Parkinson's disease before and after the deep brain stimulation of the bilateral subthalamic nucleus», *Sci. Rep.*, vol. 13, fasc. 1, p. 6997, apr. 2023, doi: 10.1038/s41598-023-34151-6.
[129] M. Tohfafarosh, N. Ratnakumar, L. Zurzolo, S. Adamovich, e X. Zhou, «Interactive Gait Rehabilitation Through Gamified Real-Time Biofeedback and Adaptive Hip Exoskeleton Assistance: A Preliminary Evaluation», *IEEE Int. Conf. Rehabil. Robot. Proc.*, vol. 2025, pp. 1799–1804, mag. 2025, doi: 10.1109/ICORR66766.2025.11063083.
[130] O. A. Howlett, N. A. Lannin, L. Ada, e C. McKinstry, «Functional Electrical Stimulation Improves Activity After Stroke: A Systematic Review With Meta-Analysis», *Arch. Phys. Med. Rehabil.*, vol. 96, fasc. 5, pp. 934–943, mag. 2015, doi: 10.1016/j.apmr.2015.01.013.
[131] A. Holobar e D. Farina, «Blind source identification from the multichannel surface electromyogram», *Physiol. Meas.*, vol. 35, fasc. 7, pp. R143–R165, lug. 2014, doi: 10.1088/0967-3334/35/7/R143.
[132] P. Picerno, «25 years of lower limb joint kinematics by using inertial and magnetic sensors: A review of methodological approaches», *Gait Posture*, vol. 51, pp. 239–246, gen. 2017, doi: 10.1016/j.gaitpost.2016.11.008.
[133] R. Moe-Nilssen, «A new method for evaluating motor control in gait under real-life environmental conditions. Part 1: The instrument», *Clin. Biomech.*, vol. 13, fasc. 4, pp. 320–327, giu. 1998, doi: 10.1016/S0268-0033(98)00089-8.
[134] A. M. Sabatini, «Quaternion-based extended Kalman filter for determining orientation by inertial and magnetic sensing», *IEEE Trans. Biomed. Eng.*, vol. 53, fasc. 7, pp. 1346–1356, lug. 2006, doi: 10.1109/TBME.2006.875664.
[135] «LSM9DS0 Hookup Guide - SparkFun Learn». Consultato: 31 ottobre 2025. [Online]. Disponibile su: https://learn.sparkfun.com/tutorials/lsm9ds0-hookup-guide/about-the-lsm9ds0
[136] O. J. Woodman, «An introduction to inertial navigation», Computer Laboratory, University of Cambridge. doi: 10.48456/TR-696.

[137] «How MEMS Accelerometer Gyroscope Magnetometer Work & Arduino Tutorial - YouTube». Consultato: 31 ottobre 2025. [Online]. Disponibile su: https://www.youtube.com/watch?v=eqZgxR6eRjo
[138] S. O. H. Madgwick, A. J. L. Harrison, e R. Vaidyanathan, «Estimation of IMU and MARG orientation using a gradient descent algorithm», in *2011 IEEE International Conference on Rehabilitation Robotics*, giu. 2011, pp. 1–7. doi: 10.1109/ICORR.2011.5975346.
[139] B. Mariani, H. Rouhani, X. Crevoisier, e K. Aminian, «Quantitative estimation of foot-flat and stance phase of gait using foot-worn inertial sensors», *Gait Posture*, vol. 37, fasc. 2, pp. 229–234, feb. 2013, doi: 10.1016/j.gaitpost.2012.07.012.
[140] D. Roetenberg, H. Luinge, P. Slycke, e others, «Xsens MVN: Full 6DOF human motion tracking using miniature inertial sensors», *Xsens Motion Technol. BV Tech Rep*, vol. 1, fasc. 2009, pp. 1–7, 2009.
[141] R. Mahony, T. Hamel, e J.-M. Pflimlin, «Nonlinear complementary filters on the special orthogonal group», *IEEE Trans. Autom. Control*, vol. 53, fasc. 5, pp. 1203–1218, 2008.
[142] G. Welch, G. Bishop, e others, «An introduction to the Kalman filter», 1995.
[143] H. J. Luinge e P. H. Veltink, «Measuring orientation of human body segments using miniature gyroscopes and accelerometers», *Med. Biol. Eng. Comput.*, vol. 43, fasc. 2, pp. 273–282, 2005.
[144] M. Mancini, L. King, A. Salarian, L. Holmstrom, J. McNames, e F. B. Horak, «Mobility lab to assess balance and gait with synchronized body-worn sensors», *J. Bioeng. Biomed. Sci.*, p. 007, 2011.
[145] APDM Wearable Technologies, «Opal User Guide», Portland, OR, Technical Report/User Manual, 2023. [Online]. Disponibile su: https://clario.com/solutions/precision-motion-for-research/
[146] K. Aminian, B. Najafi, C. Büla, P.-F. Leyvraz, e P. Robert, «Spatio-temporal parameters of gait measured by an ambulatory system using miniature gyroscopes», *J. Biomech.*, vol. 35, fasc. 5, pp. 689–699, 2002.
[147] A. Salarian *et al.*, «Gait assessment in Parkinson's disease: toward an ambulatory system for long-term monitoring», *IEEE Trans. Biomed. Eng.*, vol. 51, fasc. 8, pp. 1434–1443, 2004.
[148] J. M. Jasiewicz *et al.*, «Gait event detection using linear accelerometers or angular velocity transducers in able-bodied and spinal-cord injured individuals», *Gait Posture*, vol. 24, fasc. 4, pp. 502–509, dic. 2006, doi: 10.1016/j.gaitpost.2005.12.017.
[149] A. M. Sabatini, C. Martelloni, S. Scapellato, e F. Cavallo, «Assessment of walking features from foot inertial sensing», *IEEE Trans. Biomed. Eng.*, vol. 52, fasc. 3, pp. 486–494, mar. 2005, doi: 10.1109/TBME.2004.840727.
[150] W.-C. Hsu *et al.*, «Multiple-Wearable-Sensor-Based Gait Classification and Analysis in Patients with Neurological Disorders», *Sensors*, vol. 18, fasc. 10, p. 3397, ott. 2018, doi: 10.3390/s18103397.
[151] D. Renggli *et al.*, «Wearable inertial measurement units for assessing gait in real-world environments», *Front. Physiol.*, vol. 11, p. 90, 2020.
[152] S. Del Din, A. Godfrey, C. Mazzà, S. Lord, e L. Rochester, «Free-living monitoring of Parkinson's disease: Lessons from the field», *Mov. Disord.*, vol. 31, fasc. 9, pp. 1293–1313, 2016.
[153] M. El-Gohary *et al.*, «Continuous monitoring of turning in patients with movement disability», *Sensors*, vol. 14, fasc. 1, pp. 356–369, 2013.
[154] A. Weiss, S. Sharifi, M. Plotnik, J. P. Van Vugt, N. Giladi, e J. M. Hausdorff, «Toward automated, at-home assessment of mobility among patients with Parkinson disease, using

a body-worn accelerometer», *Neurorehabil. Neural Repair*, vol. 25, fasc. 9, pp. 810–818, 2011.
[155] L. Kribus-Shmiel, G. Zeilig, B. Sokolovski, e M. Plotnik, «How many strides are required for a reliable estimation of temporal gait parameters? Implementation of a new algorithm on the phase coordination index», *PLoS ONE*, vol. 13, fasc. 2, p. e0192049, feb. 2018, doi: 10.1371/journal.pone.0192049.
[156] D. Rodríguez-Martín *et al.*, «A Waist-Worn Inertial Measurement Unit for Long-Term Monitoring of Parkinson's Disease Patients», *Sensors*, vol. 17, fasc. 4, p. 827, apr. 2017, doi: 10.3390/s17040827.
[157] L. Palmerini, L. Rocchi, S. Mazilu, E. Gazit, J. M. Hausdorff, e L. Chiari, «Identification of Characteristic Motor Patterns Preceding Freezing of Gait in Parkinson's Disease Using Wearable Sensors», *Front. Neurol.*, vol. 8, p. 394, ago. 2017, doi: 10.3389/fneur.2017.00394.
[158] D.-S. Komaris, G. Tarfali, B. O'Flynn, e S. Tedesco, «Unsupervised IMU-based evaluation of at-home exercise programmes: a feasibility study», *BMC Sports Sci. Med. Rehabil.*, vol. 14, fasc. 1, p. 28, dic. 2022, doi: 10.1186/s13102-022-00417-1.
[159] M. Bächlin *et al.*, «Wearable assistant for Parkinson's disease patients with the freezing of gait symptom», *IEEE Trans. Inf. Technol. Biomed.*, vol. 14, fasc. 2, pp. 436–446, 2010, doi: 10.1109/TITB.2009.2036165.
[160] A. Mazzetta, G. Di Lazzaro, V. Pierella, E. P. Scilingo, e N. Vanello, «A wearable system for the detection of freezing of gait in Parkinson's disease using inertial and electromyographic sensors», *IEEE Trans. Neural Syst. Rehabil. Eng.*, vol. 27, fasc. 10, pp. 2001–2009, 2019, doi: 10.1109/TNSRE.2019.2939365.
[161] H. M. Cockx, R. Oostenveld, Y. A. Flórez, B. R. Bloem, I. G. M. Cameron, e R. J. A. van Wezel, «Freezing of gait in Parkinson's disease is related to imbalanced stopping–related cortical activity», *Brain Commun.*, vol. 6, fasc. 5, p. fcae259, 2024, doi: 10.1093/braincomms/fcae259.
[162] V. Belluscio, S. Stuart, E. Bergamini, G. Vannozzi, e M. Mancini, «The Association between Prefrontal Cortex Activity and Turning Behavior in People with and without Freezing of Gait», *Neuroscience*, vol. 416, pp. 168–176, set. 2019, doi: 10.1016/j.neuroscience.2019.07.024.
[163] E. E. Tripoliti *et al.*, «Automatic detection of freezing of gait events in patients with Parkinson's disease», *Comput. Methods Programs Biomed.*, vol. 110, fasc. 1, pp. 12–26, apr. 2013, doi: 10.1016/j.cmpb.2012.10.016.
[164] A. Suppa *et al.*, «l-DOPA and Freezing of Gait in Parkinson's Disease: Objective Assessment through a Wearable Wireless System», *Front. Neurol.*, vol. 8, ago. 2017, doi: 10.3389/fneur.2017.00406.
[165] M. Mancini, K. C. Priest, J. G. Nutt, e F. B. Horak, «Quantifying freezing of gait in Parkinson's disease during the instrumented timed up and go test», in *2012 Annual International Conference of the IEEE Engineering in Medicine and Biology Society*, ago. 2012, pp. 1198–1201. doi: 10.1109/EMBC.2012.6346151.
[166] S. T. Moore, «Autonomous identification of freezing of gait in Parkinson's disease from lower-body segmental accelerometry | Journal of NeuroEngineering and Rehabilitation». [Online]. Disponibile su: https://link.springer.com/article/10.1186/1743-0003-10-19
[167] C. Ahlrichs *et al.*, «Detecting freezing of gait with a tri-axial accelerometer in Parkinson's disease patients», *Med. Biol. Eng. Comput.*, vol. 54, fasc. 1, pp. 223–233, gen. 2016, doi: 10.1007/s11517-015-1395-3.
[168] S. Mazilu *et al.*, «Online detection of freezing of gait with smartphones and machine learning techniques», in *2012 6th International Conference on Pervasive Computing Technologies for Healthcare (PervasiveHealth) and Workshops*, mag. 2012, pp. 123–130. doi: 10.4108/icst.pervasivehealth.2012.248680.

[169] Y. Zhang, W. Yan, Y. Yao, J. B. Ahmed, Y. Tan, e D. Gu, «Prediction of Freezing of Gait in Patients With Parkinson's Disease by Identifying Impaired Gait Patterns», *IEEE Trans. Neural Syst. Rehabil. Eng.*, vol. 28, fasc. 3, pp. 591–600, mar. 2020, doi: 10.1109/TNSRE.2020.2969649.

[170] H. B. Kim *et al.*, «Validation of Freezing-of-Gait Monitoring Using Smartphone», *Telemed. J. E-Health Off. J. Am. Telemed. Assoc.*, vol. 24, fasc. 11, pp. 899–907, nov. 2018, doi: 10.1089/tmj.2017.0215.

[171] L. Borzì, L. Sigcha, D. Rodríguez-Martín, e G. Olmo, «Real-time detection of freezing of gait in Parkinson's disease using multi-head convolutional neural networks and a single inertial sensor», *Artif. Intell. Med.*, vol. 135, p. 102459, gen. 2023, doi: 10.1016/j.artmed.2022.102459.

[172] A. Nieuwboer, R. Dom, W. De Weerdt, K. Desloovere, P. Cras, e V. Thijs, «Electromyographic recordings of freezing episodes in Parkinson's disease», *Mov. Disord.*, vol. 19, fasc. 5, pp. 544–551, 2004, doi: 10.1002/mds.20011.

[173] A. Tahafchi, M. Varreci, N. Giladi, e J. M. Hausdorff, «Detection of freezing of gait in Parkinson's disease using EMG and inertial sensors», *J. NeuroEngineering Rehabil.*, vol. 14, fasc. 1, pp. 1–10, 2017, doi: 10.1186/s12984-017-0300-0.

[174] Y. Zhang, N. Howard, X. Li, e others, «Multimodal Data for the Detection of Freezing of Gait in Parkinson's Disease», *Sci. Data*, vol. 9, fasc. 1, p. 658, 2022, doi: 10.1038/s41597-022-01713-8.

[175] Moore, Anna, «Wearable Surface Electromyography System to Predict Freeze of Gait in Parkinson's Disease Patients». Consultato: 5 ottobre 2025. [Online]. Disponibile su: https://www.mdpi.com/1424-8220/24/23/7853

[176] L. Borzì, I. Mazzetta, A. Zampogna, A. Suppa, G. Olmo, e F. Irrera, «Prediction of freezing of gait in Parkinson's disease using wearables and machine learning», *Sensors*, vol. 21, fasc. 2, p. 614, 2021.

[177] I. Goodfellow, Y. Bengio, A. Courville, e Y. Bengio, *Deep learning*, vol. 1. MIT press Cambridge, 2016.

[178] R. Kohavi e others, «A study of cross-validation and bootstrap for accuracy estimation and model selection», in *Ijcai*, Montreal, Canada, 1995, pp. 1137–1145.

[179] I. Guyon e A. Elisseeff, «An introduction to variable and feature selection», *J. Mach. Learn. Res.*, vol. 3, fasc. Mar, pp. 1157–1182, 2003.

[180] Y. Saeys, I. Inza, e P. Larranaga, «A review of feature selection techniques in bioinformatics», *bioinformatics*, vol. 23, fasc. 19, pp. 2507–2517, 2007.

[181] H. Peng, F. Long, e C. Ding, «Feature selection based on mutual information criteria of max-dependency, max-relevance, and min-redundancy», *IEEE Trans. Pattern Anal. Mach. Intell.*, vol. 27, fasc. 8, pp. 1226–1238, 2005.

[182] M. Robnik-Šikonja e I. Kononenko, «Theoretical and empirical analysis of ReliefF and RReliefF», *Mach. Learn.*, vol. 53, fasc. 1, pp. 23–69, 2003.

[183] R. Kohavi e G. H. John, «Wrappers for feature subset selection», *Artif. Intell.*, vol. 97, fasc. 1, pp. 273–324, dic. 1997, doi: 10.1016/S0004-3702(97)00043-X.

[184] S. Pardoel, J. Kofman, J. Nantel, e E. D. Lemaire, «Wearable-Sensor-Based Detection and Prediction of Freezing of Gait in Parkinson's Disease: A Review», *Sensors*, vol. 19, fasc. 23, p. 5141, nov. 2019, doi: 10.3390/s19235141.

[185] C. Cortes e V. Vapnik, «Support-vector networks», *Mach. Learn.*, vol. 20, fasc. 3, pp. 273–297, 1995, doi: 10.1007/BF00994018.

[186] D. Bzdok, M. Krzywinski, e N. Altman, «Machine learning: supervised methods», *Nat. Methods*, vol. 15, fasc. 1, p. 5, 2018.

[187] «Decision Tree in Machine Learning», AlmaBetter. Consultato: 27 ottobre 2025. [Online]. Disponibile su: https://www.almabetter.com/bytes/tutorials/data-science/decision-tree
[188] S. Tangirala, «Evaluating the impact of GINI index and information gain on classification using decision tree classifier algorithm», *Int. J. Adv. Comput. Sci. Appl.*, vol. 11, fasc. 2, pp. 612–619, 2020.
[189] S. Rezvanian e T. E. Lockhart, «Electromyographic and kinematic analysis of gait instability in Parkinson's disease», *Gait Posture*, vol. 45, pp. 102–108, 2016, doi: 10.1016/j.gaitpost.2015.12.015.
[190] L. Breiman, «Random forests», *Mach. Learn.*, vol. 45, fasc. 1, pp. 5–32, 2001, doi: 10.1023/A:1010933404324.
[191] J. H. Friedman, «Greedy function approximation: A gradient boosting machine.», *Ann. Stat.*, vol. 29, fasc. 5, pp. 1189–1232, ott. 2001, doi: 10.1214/aos/1013203451.
[192] H. Deng, Y. Zhou, L. Wang, e C. Zhang, «Ensemble learning for the early prediction of neonatal jaundice with genetic features», *BMC Med. Inform. Decis. Mak.*, vol. 21, fasc. 1, p. 338, dic. 2021, doi: 10.1186/s12911-021-01701-9.
[193] T. Cover e P. Hart, «Nearest neighbor pattern classification», *IEEE Trans. Inf. Theory*, vol. 13, fasc. 1, pp. 21–27, 1967.
[194] H. Bhat, «KNN Algorithm in Python: Implementation with Examples», AlmaBetter. Consultato: 27 ottobre 2025. [Online]. Disponibile su: https://www.almabetter.com/bytes/articles/knn-algorithm-python
[195] N. Gogia, «THE STORY OF LOGISTIC REGRESSION…», Analytics Vidhya. Consultato: 27 ottobre 2025. [Online]. Disponibile su: https://medium.com/analytics-vidhya/the-story-of-logistic-regression-3a978fdc4fe2
[196] R. Tibshirani, «Regression shrinkage and selection via the lasso», *J. R. Stat. Soc. Ser. B Stat. Methodol.*, vol. 58, fasc. 1, pp. 267–288, 1996.
[197] B. T. Cole, S. H. Roy, e S. H. Nawab, «Detecting freezing-of-gait during unscripted and unconstrained activity», in *2011 Annual International Conference of the IEEE Engineering in Medicine and Biology Society*, ago. 2011, pp. 5649–5652. doi: 10.1109/IEMBS.2011.6091367.
[198] H. Feng, Y. Jiang, J. Lin, W. Qin, L. Jin, e X. Shen, «Cortical activation and functional connectivity during locomotion tasks in Parkinson's disease with freezing of gait», *Front. Aging Neurosci.*, vol. 15, mar. 2023, doi: 10.3389/fnagi.2023.1068943.
[199] P. Pinti *et al.*, «The present and future use of functional near-infrared spectroscopy (fNIRS) for cognitive neuroscience», *Ann. N. Y. Acad. Sci.*, vol. 1464, fasc. 1, pp. 5–29, mar. 2020, doi: 10.1111/nyas.13948.
[200] «NIRSport2 | fNIRS Systems | NIRS Devices | NIRx», NIRx Medical Technologies. Consultato: 1 novembre 2025. [Online]. Disponibile su: https://nirx.net/nirsport
[201] «Action Observation and Motor Imagery Improve Dual Task in Parkinson's Disease: A Clinical/fMRI Study - Sarasso - 2021 - Movement Disorders - Wiley Online Library». Consultato: 20 novembre 2025. [Online]. Disponibile su: https://movementdisorders.onlinelibrary.wiley.com/doi/full/10.1002/mds.28717
[202] «Precision Motion for Research», Clario. Consultato: 1 novembre 2025. [Online]. Disponibile su: https://clario.com/solutions/precision-motion-for-research/
[203] S. I. Materia, «FREEEMG | Sistema EMG di superficie wireless | BTS Bioengineering», BTS. Consultato: 1 novembre 2025. [Online]. Disponibile su: https://www.btsbioengineering.com/it/products/freeemg/
[204] M. Barbero, R. Merletti, e A. Rainoldi, *Atlas of Muscle Innervation Zones*. Milano: Springer Milan, 2012. doi: 10.1007/978-88-470-2463-2.

[205] É. Delaire *et al.*, «NIRSTORM: a Brainstorm extension dedicated to functional near-infrared spectroscopy data analysis, advanced 3D reconstructions, and optimal probe design», *Neurophotonics*, vol. 12, fasc. 02, mag. 2025, doi: 10.1117/1.NPh.12.2.025011.

Ringraziamenti

Giunto al termine di questo percorso, vorrei esprimere la mia gratitudine verso tutti coloro che hanno contribuito e mi hanno permesso di renderlo possibile.

Ci tengo a ringraziare il Professor Molinari, esempio di disponibilità e professionalità durante tutte le fasi di questo percorso, e il Chiar.mo Professor Filippi per avermi dato la possibilità di entrare a far parte di questo progetto in un contesto così stimolante dal punto di vista scientifico e professionale. Vorrei inoltre ringraziare la Professoressa Agosta, fonte di ispirazione per la sua competenza e dedizione.

Ringrazio in particolar modo Silvia, a cui va tutta la mia ammirazione per la sua enorme conoscenza e per la capacità di sapere sempre come guidare chi lavora con lei, essendo un punto di riferimento costante. È stato per me un privilegio e un onore avere la possibilità di imparare da lei in questo percorso, che mi ha formato professionalmente e personalmente.

Un grazie enorme a Luca e Tommaso per la disponibilità mostrata, i consigli e la conoscenza che mi hanno trasmesso, facendomi sentire sempre come uno di loro sin dal primo giorno. Grazie per avermi seguito per tutto il percorso e avermi supportato quotidianamente.

Vorrei ringraziare Elisabetta e Gardo, il cui punto di vista clinico estremamente competente mi ha permesso di espandere le mie conoscenze oltre quanto mi aspettassi, grazie per aver sempre speso una parola in più di quanto fosse necessario e per aver supportato il mio lavoro di tesi.

Una considerazione speciale va a tutti i ragazzi e le ragazze del Neurotech: Marco, Alejandro, Laura, Anna, Andre e i già citati Tommaso, Luca, Gardo ed Elisabetta. Grazie per aver contribuito a rendere questa esperienza fantastica, permettendomi di alternare al lavoro momenti di leggerezza e spensieratezza. Ringrazio anche tutti i ragazzi e ragazze del CAB, in particolar modo Gianca, sempre pronto a fornire pillole di saggezza e a strapparmi un sorriso. Siete persone vere, vi ringrazio infinitamente.

Infine, grazie ad Alice e Bea, le migliori compagne di viaggio con cui condividere questa esperienza. Sapere di poter contare su di voi mi ha sicuramente permesso di vivere a pieno ogni momento, rendendo questo percorso ancora più bello e importante.